

**UNDERSTANDING CRYSTALLIZATION MECHANISMS OF A  
BIODEGRADABLE COPOLYMER POLY[(R)-3-HYDROXYBUTYRATE-CO-  
(R)-3-HYDROXYHEXANOATE] (PHBX) AND THE INHIBITION OF ITS  
CRYSTALLIZATION USING ALUMINUM OXIDE AND  
PSEUDOBOEHMITE**

by

Changhao Liu

A dissertation submitted to the Faculty of the University of Delaware in partial fulfillment of the requirements for the degree of Doctor of Philosophy in Materials Science and Engineering

Fall 2019

© 2019 Changhao Liu  
All Rights Reserved

**UNDERSTANDING CRYSTALLIZATION MECHANISMS OF A  
BIODEGRADABLE COPOLYMER POLY[(R)-3-HYDROXYBUTYRATE-CO-  
(R)-3-HYDROXYHEXANOATE] (PHBHX) AND THE INHIBITION OF ITS  
CRYSTALLIZATION USING ALUMINUM OXIDE AND  
PSEUDOBOEHMITE**

by

Changhao Liu

Approved: \_\_\_\_\_  
Darrin Pochan, Ph.D.  
Chair of the Department of Materials Science and Engineering

Approved: \_\_\_\_\_  
Levi T. Thompson, Ph.D.  
Dean of the College of Engineering

Approved: \_\_\_\_\_  
Douglas J. Doren, Ph.D.  
Interim Vice Provost for Graduate and Professional Education and  
Dean of the Graduate College

I certify that I have read this dissertation and that in my opinion it meets the academic and professional standard required by the University as a dissertation for the degree of Doctor of Philosophy.

Signed:

---

John F. Rabolt, Ph.D.  
Professor in charge of dissertation

I certify that I have read this dissertation and that in my opinion it meets the academic and professional standard required by the University as a dissertation for the degree of Doctor of Philosophy.

Signed:

---

D. Bruce Chase, Ph.D.  
Professor in charge of dissertation

I certify that I have read this dissertation and that in my opinion it meets the academic and professional standard required by the University as a dissertation for the degree of Doctor of Philosophy.

Signed:

---

Isao Noda, Ph.D.  
Professor in charge of dissertation

I certify that I have read this dissertation and that in my opinion it meets the academic and professional standard required by the University as a dissertation for the degree of Doctor of Philosophy.

Signed:

---

David C. Martin, Ph.D.  
Member of dissertation committee

I certify that I have read this dissertation and that in my opinion it meets the academic and professional standard required by the University as a dissertation for the degree of Doctor of Philosophy.

Signed:

---

Chaoying Ni, Ph.D.  
Member of dissertation committee

## ACKNOWLEDGMENTS

First, I would like to express my gratitude to my advisors: Dr. John Rabolt, Dr. Bruce Chase, and Dr. Isao Noda for their endless support, guidance, and encouragement throughout my Ph.D. research. Without their support, the achievement in this dissertation would not be possible. Thank you, Dr. Rabolt, for your meticulous research spirit and kindness, which helped me overcome great challenges over the years. Thank you, Dr. Chase, for your objective research suggestions and criticism, pushing me to pursuit unbiased results. Thank you, Dr. Noda, for providing all the first-hand PHA knowledge. Your great scientific ideas, motivation, and patience have pushed me a lot to pursue my Ph.D. degree.

Additionally, I would like to thank the rest of my dissertation committee. Dr. David Martin and Dr. Chaoying Ni. I sincerely express my gratitude to Dr. Martin's guidance in polymer crystal growth and TEM study on polymers. I appreciate Dr. Ni's support on guiding me on performing electron diffraction experiments for beam sensitive polymer single crystals.

I also thank my fellow lab mates: Dr. Brian Sobieski, Dr. Shuyu Xu, Dr. Liang Gong, Dr. Reva street, and Joanna Norris. Dr. Brian Sobieski also served as a fellow mentor of mine. He helped develop my scientific thinking of conducting research. I also thank my collaborators: Yuying Zhang, Meng Jia, and Dr. Jing Qu. I thank Gerald Poirier for providing endless support on training and problem-solving in the advanced materials characterization lab. I thank Dr. Jennifer Sloppy and Dr. Yong Zhao for the training and guidance on the use of an electron microscope.

I would like to thank Dr. Wesley Sattler, Dr. Joseph Manna, and Dr. Yuanqiao Rao. Dr. Sattler and Dr. Rao were my mentors during my Dow internship. Their guidance strengthened my research ability. I appreciate Dr. Manna as my manager during my Dow internship. Working under your wings accelerated my adaption to the new environment.

Last but not least, I would like to thank my family: my girlfriend: Ivy Chi, my parents: Jianhua Liu and Yan Gao. Thank you all for your love, motivation, and support throughout my life.

I would like to acknowledge the support from Delaware NSF EPSCoR Grant # 1301765, 1757353, and the NSF DMR Polymers Program Grant #1407255.

## TABLE OF CONTENTS

LIST OF TABLES .....	x
LIST OF FIGURES .....	xi
ABSTRACT .....	xx

### Chapter

1	BACKGROUND .....	1
1.1	Plastic Pollution Overview .....	1
1.2	Polyhydroxyalkanoate (PHA) .....	3
1.3	Research Overview .....	8
1.3.1	Understanding PHBHx crystallization in solution grown single crystals .....	8
1.3.2	Using aluminum oxide (AO) and pseudoboehmite (PB) to retard or inhibit PHB and PHBHx crystallization .....	10
1.4	Organization .....	10
2	MATERIALS AND CHARACTERIZATION METHODS .....	12
2.1	Materials .....	12
2.1.1	PHBHx .....	12
2.1.2	Other materials .....	13
2.2	Characterization .....	13
2.2.1	Transmission electron microscopy (TEM) .....	13
2.2.2	X-ray diffraction .....	14
2.2.3	Fourier transform infrared (FTIR) spectroscopy .....	15
2.2.4	X-ray photoelectron spectroscopy (XPS) .....	15
3	CRYSTALLIZATION METHODS DEVELOPMENT FOR SOLUTION GROWING PHBHx SINGLE CRYSTALS .....	17
3.1	Isothermal crystallization method .....	17

3.2	Self-seeding method .....	21
3.3	Ultrasonication assisted self-seeding process.....	30
3.4	Gradual cooling method .....	35
3.5	Comments on the three crystallization methods.....	38
4	CRYSTALLIZATION MECHANISM FOR PHBHx(3.9mol%) SINGLE CRYSTALS UNDER ISOTHERMAL GROWTH.....	40
4.1	Preparation conditions .....	40
4.2	Crystal morphology and crystal polymorph as a function of $T_c$ .....	42
4.3	Variations of lattice parameters, a and b, as a function of $T_c$ .....	49
4.4	Lamellar thickness evaluation .....	50
4.5	DSC studies of PHBHx(3.9mol%) grown at different $T_c$ .....	54
4.6	FTIR study of PHBHx(3.9mol%) single crystals.....	56
4.7	Crystal structure analysis.....	58
4.8	Critical dose measurement of PHBHx single crystals.....	60
5	EFFECT OF 3HHX ON THE MORPHOLOGY OF SOLUTION GROWN PHBHx CRYSTALS .....	65
5.1	Effect of 3HHx content on single crystal morphology.....	65
5.2	Characteristic morphology of PHBHx(3.9mol%), PHBHx(7.6mol%), and PHBHx(13mol%) crystals .....	69
6	CRYSTALLIZATION OF PHB AND PHBHx ULTRATHIN FILMS ON METAL OXIDE FLAT SURFACES.....	75
6.1	Discovery of the crystallization retardation of PHBHx(13mol%) thick sheet sandwiched by Al foil .....	75
6.2	Flat metal coated glass substrates.....	78
6.3	Thin film preparation and melt crystallization on surfaces .....	79
6.4	Typical IRRAS spectra changes during crystallization at room temperature.....	81
6.5	Crystallization of PHB and PHBHx (13mol%) thin films on different surfaces.....	83
6.6	XPS studies on different metal surfaces.....	85
7	CRYSTALLIZATION RETARDATION OF ULTRATHIN FIOMLS OF POLY[(R)-3-HYDROXYBUTYRATE] (PHB) AND A RANDOM COPOLYMER POLY[(R)-3-HYDROXYBUTYRATE-CO-(R)-3- HYDROXYHEXANOATE] (PHBHx) ON AN ALUMINUM OXIE SURFACE .....	91

7.1	Crystallization kinetics of PHB, PHBHx(5.8mol%), PHBHx(9.4mol%) and PHBHx(13mol%) on gold and aluminum substrates .....	91
7.2	Avrami analysis of crystallization kinetics.....	95
7.3	Mechanistic study of crystallization retardation.....	100
7.3.1	H-bonding study between PHB/PHBHx and AO surface .....	100
7.3.2	Dipole-dipole interaction between PHB/PHBHx and AO surface.....	104
7.3.3	The disordered nature of AO surface .....	105
7.3.4	Effect of the aluminum substrate on the crystal orientation.....	107
8	INTERMOLECULAR HYDROGEN BONDING BETWEEN POLY[(R)-3-HYDROXYBUTYRATE] (PHB) AND PSEUDOBOEHMITE AND ITS EFFECT ON CRYSTALLIZATION OF PHB .....	113
8.1	Preparation of a pseudoboehmite surface.....	113
8.2	Intermolecular H-bonding of aPHB and PB.....	114
8.3	Intermolecular H-bonding of isotactic PHB (iPHB) with PB .....	118
8.4	Effects of intermolecular H-bonding on the crystallization behavior of PHB .....	120
9	FUTURE DIRECTIONS AND RECOMMENDATIONS .....	125
9.1	Comments on the special interaction of -CH $\cdots$ O=C in PHBHx alpha crystal structure .....	125
9.2	Other directions .....	128
	REFERENCES.....	130
	Appendix	
A	PERMISSIONS .....	135

## LIST OF TABLES

<b>Table 2.1: A list of all PHBHx samples provided by Proctor and Gamble with their weight averaged molecular weight (<math>M_w</math>), melting temperatures (<math>T_m</math>), and polydispersity indices (PDI).....</b>	<b>13</b>
<b>Table 4.1: Crystallization conditions .....</b>	<b>41</b>
<b>Table 6.1: Calculated surface energy for gold and silver surfaces .....</b>	<b>90</b>
<b>Table 7.1: kinetic parameters derived from experimental Avrami analysis .....</b>	<b>98</b>
<b>Table 7.2: Calculated surface energy for gold and aluminum oxide (AO) surfaces .....</b>	<b>105</b>

## LIST OF FIGURES

<b>Figure 1.1: General structure of PHA. R<sub>1</sub> and R<sub>2</sub> are alkyl groups with C<sub>1</sub> to C<sub>13</sub>. x and y = 1 to 4. ....</b>	<b>4</b>
<b>Figure 1.2: molecular structure of PHB .....</b>	<b>4</b>
<b>Figure 1.3: Crystallinity of PHB copolymers as a function of comonomer content.<sup>5</sup> .....</b>	<b>5</b>
<b>Figure 1.4: molecular structure of PHBV .....</b>	<b>6</b>
<b>Figure 1.5: molecular structure of PHBH<sub>x</sub> .....</b>	<b>7</b>
<b>Figure 1.6: Schematic illustrating two processing methods to prepare lamellar single crystals: melt crystallization(left) and solution crystallization (right).....</b>	<b>9</b>
<b>Figure 3.1: A schematic to illustrate two routes to prepare supercooled solution in the isothermal crystallization method. T<sub>d</sub> is the dissolution temperature. T<sub>c</sub> is the crystallization temperature. ....</b>	<b>18</b>
<b>Figure 3.2: A: suspension formed due to phase separation. Inset(A): micrograph of amorphous globules due to phase separation. B: suspension formed due to nucleation and growth. Inset(B): micrograph of PHBH<sub>x</sub> crystals. ....</b>	<b>20</b>
<b>Figure 3.3: A: white “nuclei” crystals formed in early crystallization stage. B: larger crystal aggregates formed after hours of crystallization. ....</b>	<b>20</b>
<b>Figure 3.4: A schematic illustration of the steps in the self-seeding method. ....</b>	<b>21</b>
<b>Figure 3.5: TEM image of PHBH<sub>x</sub>(3.9mol%) precursor crystals .....</b>	<b>23</b>
<b>Figure 3.6: PHBH<sub>x</sub> (3.9mol%) crystals grown using self-seeding method with a T<sub>s</sub> of 95 °C. Red arrows indicate notches developed on the lateral side of lamellae. Green arrow indicates a well-developed self-seeded lamellae. Blue arrows indicate self-seeded crystals developed near lamellar lateral sides.....</b>	<b>25</b>

<b>Figure 3.7: PHBHx (3.9mol%) crystals grown using self-seeding method with a <math>T_s</math> of 97 °C. Red arrows indicate notches developed on the lateral side of lamellae. Green arrows indicate a well developed self-seeded lamellae. ....</b>	<b>26</b>
<b>Figure 3.8: PHBHx (3.9mol%) crystals grown using self-seeding method with a <math>T_s</math> of 101 °C. Red arrow indicates residual precursor crystals. ....</b>	<b>27</b>
<b>Figure 3.9: PHBHx (3.9mol%) crystals grown using self-seeding method with a <math>T_s</math> of 105 °C. ....</b>	<b>28</b>
<b>Figure 3.10: PHBHx (3.9mol%) crystals grown using self-seeding method with a <math>T_s</math> of 108 °C ....</b>	<b>28</b>
<b>Figure 3.11: A schematic to illustrate a proposed seeding process .....</b>	<b>30</b>
<b>Figure 3.12: Fragmented PHBHx(3.9mol%) precursor crystals after ultrasonication for 10mins.....</b>	<b>32</b>
<b>Figure 3.13: PHBHx(3.9mol%) single crystals made by the ultrasonification assisted method as a function of sonication time.....</b>	<b>32</b>
<b>Figure 3.14: PHBHx(3.9mol%) precursor crystals grown from ultrasonicated polymers. ....</b>	<b>33</b>
<b>Figure 3.15: PHBHx(3.9mol%) single crystals prepared using ultrasonification assisted self-seeding method. Green boxes and green arrows indicate self-assembled structures comprised of multiple individual self-seeded crystals. Insert is fragmented precursor crystals treated by ultrasonification. ....</b>	<b>34</b>
<b>Figure 3.16: A schematic illustrating the formation of self-assembled structure comprised of multiple individual self-seeded crystals.....</b>	<b>35</b>
<b>Figure 3.17: PHBHx(13mol%) spherulites grown using a gradual cooling method with <math>T_d = 110</math> °C.....</b>	<b>37</b>
<b>Figure 3.18: PHBHx(13mol%) spherulites grown using a gradual cooling method with <math>T_d = 105</math> °C.....</b>	<b>37</b>
<b>Figure 3.19: PHBHx(13mol%) spherulites grown using a gradual cooling method with <math>T_d = 100</math> °C.....</b>	<b>38</b>
<b>Figure 3.20: PHBHx(13mol%) spherulites grown using a gradual cooling method with <math>T_d = 90</math> °C.....</b>	<b>38</b>

<b>Figure 4.1: A phase diagram of PHBHx(3.9mol%) in the solvent mixture of chloroform and ethanol.....</b>	<b>41</b>
<b>Figure 4.2: Morphology and diffraction pattern (from yellow boxed area) of PHBHx(3.9mol%) crystals grown at -20 °C. ....</b>	<b>43</b>
<b>Figure 4.3: Morphology and diffraction pattern (from red highlighted area) of PHBHx(3.9mol%) crystals grown at 20 °C.....</b>	<b>44</b>
<b>Figure 4.4: Morphology and diffraction pattern of PHBHx(3.9mol%) crystals grown at 40 °C. ....</b>	<b>45</b>
<b>Figure 4.5: Morphology and diffraction pattern of PHBHx(3.9mol%) crystals grown at 55 °C .....</b>	<b>45</b>
<b>Figure 4.6: Morphology and diffraction pattern of PHBHx(3.9mol%) crystals grown at 60 °C .....</b>	<b>46</b>
<b>Figure 4.7: Morphology and diffraction pattern of PHBHx(3.9mol%) crystals grown at 65 °C .....</b>	<b>46</b>
<b>Figure 4.8: Morphology and diffraction pattern of PHBHx(3.9mol%) crystals grown at 75 °C .....</b>	<b>47</b>
<b>Figure 4.9: A schematic to illustrate the needle-shaped crystal, apex angle <math>\Theta</math>, and growth dimension x and y along two directions.....</b>	<b>48</b>
<b>Figure 4.10: Histograms of measured apex angle of crystals at each <math>T_c</math>. ....</b>	<b>48</b>
<b>Figure 4.11: The plot of apex angle, growth rate ratio, and unit cell packing rate ratio along the a- and b- axes as a function of <math>T_c</math>.....</b>	<b>49</b>
<b>Figure 4.12: A schematic to illustrate a lamella crystal model with 3HHx excluded from the crystalline layer and located on the folding layer. ....</b>	<b>50</b>
<b>Figure 4.13: A schematic to compare single crystal mat and powder XRD. ....</b>	<b>51</b>
<b>Figure 4.14: XRD data for PHBHx(3.9mol%) single crystal mats at different <math>T_c</math> and powder diffraction data.....</b>	<b>52</b>
<b>Figure 4.15: The plots of crystallites size along the b and c axis as a function of <math>T_c</math> .....</b>	<b>52</b>
<b>Figure 4.16: AFM height image of PHBHx(3.9mol%) single crystals at 20 °C ....</b>	<b>53</b>

<b>Figure 4.17: AFM height image of PHBHx(3.9mol%) single crystals at 60 °C ....</b>	<b>53</b>
<b>Figure 4.18: DSC heating curves for PHBHx(3.9mol%) single crystals grown at -20, 20, 40, and 60 °C. ....</b>	<b>55</b>
<b>Figure 4.19: DSC heating traces for PHBHx(3.9mol%) single crystals grown at 60 °C as a function of heating rate.....</b>	<b>56</b>
<b>Figure 4.20: FTIR spectra of PHBHx(3.9mol%) single crystals at different T<sub>c</sub>. The carbonyl stretching region is on the left and the CH stretching region is on the right. ....</b>	<b>57</b>
<b>Figure 4.21: Schematic of PHB alpha crystalline structure viewed along c (left) and b (right) directions. ....</b>	<b>59</b>
<b>Figure 4.22: Morphology and diffraction pattern changes of PHBHx(3.9mol%) single crystals as a function of electron dose. ....</b>	<b>60</b>
<b>Figure 4.23: Representative radial cross line drawn on raw diffraction pattern. ....</b>	<b>62</b>
<b>Figure 4.24: 1-D profile from the cross line draw in Figure 3.23.....</b>	<b>62</b>
<b>Figure 4.25: Logarithm plots of (110) diffraction peak intensity as a function of electron dose for PHBHx(3.9mol%) single crystals grown at different T<sub>c</sub>. ....</b>	<b>63</b>
<b>Figure 4.26: Plot of critical dose vs melting temperatures for different polymers.<sup>18</sup> The red cross represents data point for PHBHx(3.9mol%)......</b>	<b>64</b>
<b>Figure 5.1: PHBHx(3.9mol%) single crystals. Crystallization method: self-seeding. Crystallization conditions: concentration = 0.027wt%, precursor crystallization (pure EtOH, T<sub>d</sub> = 110 °C, gradual cooling in an oil bath), seeding process (T<sub>i</sub> = 70°C, heating rate = 30°C/hr, T<sub>s</sub> = 100°C, gradual cooling in an oil bath). ....</b>	<b>66</b>
<b>Figure 5.2: An individual PHBHx(3.9mol%) single crystal grown by the self-seeding method and its EDP. ....</b>	<b>67</b>

<b>Figure 5.3: PHBHx(7.6mol%) single crystals. Crystallization method: self-seeding. Crystallization conditions: concentration = 0.01wt%, precursor crystallization (pure EtOH, <math>T_d = 110\text{ }^\circ\text{C}</math>, gradual cooling in an oil bath), seeding process (<math>T_i = 50\text{ }^\circ\text{C}</math>, heating rate = <math>30\text{ }^\circ\text{C/hr}</math>, <math>T_s = 68\text{ }^\circ\text{C}</math>, gradual cooling in an oil bath). Type A crystals (upper) and Type B crystals (bottom).</b>	67
<b>Figure 5.4: An individual PHBHx(7.6mol%) single crystal grown by self-seeding and its EDP.</b>	68
<b>Figure 5.5: PHBHx(13mol%) single crystals. Crystallization method: self seeding. Crystallization conditions: concentration = 0.01wt%, precursor preparation (pure EtOH, <math>T_d = 110\text{ }^\circ\text{C}</math>, gradual cooling in an oil bath), <math>T_i = 50\text{ }^\circ\text{C}</math>, heating rate = <math>30\text{ }^\circ\text{C/hr}</math>, <math>T_s = 79\text{ }^\circ\text{C}</math>, gradual cooling in an oil bath).</b>	68
<b>Figure 5.6: Individual PHBHx(13mol%) single crystal grown by self-seeding and its EDP and color reverted EDP.</b>	69
<b>Figure 5.7: PHBHx(3.9mol%) crystals. Left, crystallization method: gradual cooling. Crystallization conditions: concentration = 0.027wt%, EtOH, <math>T_d = 110\text{ }^\circ\text{C}</math>, gradual cooling in an oil bath. Right, crystallization method: isothermal crystallization. Crystallization conditions: concentration = 0.01wt%, <math>\text{CHCl}_3/\text{EtOH}</math> ratio = 0.11, <math>T_c = 65\text{ }^\circ\text{C}</math>. Red arrows indicate locations of cracks.</b>	70
<b>Figure 5.8: PHBHx(7.6mol%) crystals. Crystallization method: gradual cooling. Crystallization conditions: concentration = 0.01wt%, <math>T_d = 110\text{ }^\circ\text{C}</math>, cooled in an oil bath. Red arrows indicate locations of cracks.</b>	70
<b>Figure 5.9: PHBHx(3.9mol%) folded crystals. Crystallization method: gradual cooling. Crystallization conditions: concentration = 0.027wt%, EtOH, <math>T_d = 110\text{ }^\circ\text{C}</math>, oil bath. Red arrows indicate folding positions.</b>	71
<b>Figure 5.10: PHBHx(3.9mol%) folded crystals. Crystallization method: gradual cooling. Crystallization conditions: concentration = 0.01wt%, EtOH, <math>T_d = 110\text{ }^\circ\text{C}</math>, cooled in an oil bath. Red arrows indicate location of folds.</b>	72
<b>Figure 5.11: PHBHx(13mol%) premature spherulites. Crystallization method: isothermal crystallization. Crystallization conditions: concentration = 0.01wt%, <math>\text{CHCl}_3/\text{EtOH}</math> ratio = 0.025, <math>T_c = 45\text{ }^\circ\text{C}</math>.</b>	73

<b>Figure 5.12. PHBHx(13mol%) twisted lamellae. They are created by ultrasonification of PHBHx(13mol%) spherulites. Crystallization method: gradual cooling. Crystallization conditions: concentration = 0.01wt%, EtOH, T<sub>d</sub> = 110 °C, air cooling.....</b>	<b>74</b>
<b>Figure 6.1: A schematic to show Al foil sandwiched PHBHx sheet and removal of one-side of the Al foil .....</b>	<b>75</b>
<b>Figure 6.2: The carbonyl regions of FITR-ATR spectra for PHBHx(13mol%) thick sheet. Black: the side of sheet without Al foil after a 4-hour at room temperature; Red: the side of sheet with Al foil after 12-hour at room temperature.....</b>	<b>77</b>
<b>Figure 6.3: AFM height images for gold, silver, aluminum, and copper surfaces and their corresponding R<sub>q</sub> .....</b>	<b>79</b>
<b>Figure 6.4: Typical XRR profile of spin coated ultrathin film.....</b>	<b>80</b>
<b>Figure 6.5: Schematic of processing procedures for spin coating and melt crystallization.....</b>	<b>81</b>
<b>Figure 6.6: IRRAS and 2nd derivative spectra of carbonyl stretching region (A) and the backbone region (B) for PHB crystallization on gold at room temperature. ....</b>	<b>82</b>
<b>Figure 6.7: The intensity plot of the IR peak at 1230 cm<sup>-1</sup> against crystallization time for PHB thin films on different substrates. ....</b>	<b>83</b>
<b>Figure 6.8: The intensity plot of the IR peak at 1230 cm<sup>-1</sup> against crystallization time for PHBHx (13mol%) thin films on different substrates.....</b>	<b>84</b>
<b>Figure 6.9: XPS profiles of the surface of the aluminum substrate. Left: Al 2p profile. Right: O 1s profile.....</b>	<b>85</b>
<b>Figure 6.10: XPS Cu 2p profiles of the surface of the copper substrate. ....</b>	<b>86</b>
<b>Figure 6.11: XPS Ag 3d profiles of the surface of a silver substrate before (red) and after (black) annealing treatment.....</b>	<b>87</b>
<b>Figure 6.12: Partially coated PHBHx on a Cu substrate after film melting. ....</b>	<b>88</b>
<b>Figure 6.13: Static contact angle measurement for a Au surface. Left: test liquid methyl iodide; right: DI water .....</b>	<b>89</b>

<b>Figure 6.14: Static contact angle measurement for Ag surface. Left: test liquid methyl iodide; right: DI water .....</b>	<b>89</b>
<b>Figure 7.1: A plot of relative crystallinity against time shows three crystallization stages: induction period, primary crystallization period, and secondary crystallization period.....</b>	<b>92</b>
<b>Figure 7.2: PHB and PHBHx time-dependent crystallinity profiles on gold as a function of 3HHx concentration. Red profiles are experimental data points. Black profiles are fittings based on Avrami analysis. ....</b>	<b>93</b>
<b>Figure 7.3: -C-O-C stretching region of the very first IRRAS spectrum of PHB crystallization on gold and aluminum substrates. Red profile: on gold. Black profile: on aluminum. ....</b>	<b>94</b>
<b>Figure 7.4: Relative crystallinity profiles of different polymers on gold and aluminum substrates. (A) PHB; (B) PHBHx(5.8mol%); (C) PHBHx(9.4mol%); (D) PHBHx(13mol%). Red curve: gold. Blue curve: aluminum.....</b>	<b>95</b>
<b>Figure 7.5: Avrami plot of PHB and PHBHx with varying 3HHx content on gold (red) and aluminum (blue) substrates. Black lines are the fits.</b>	<b>97</b>
<b>Figure 7.6: (A) Avrami index plot against 3HHx content on gold (black) and aluminum (red) substrates. (B) plot of retardation factor <math>F_r</math> against 3HHx content.....</b>	<b>99</b>
<b>Figure 7.7: XPS profiles of the surface of an aluminum substrate. Left: Al 2p profile. Right: O 1s profile.....</b>	<b>101</b>
<b>Figure 7.8: Comparison of IR carbonyl stretching region of atactic PHB (aPHB) nanolayer vs 40 nm layer on aluminum substrate (A), and gold substrate (B).....</b>	<b>103</b>
<b>Figure 7.9: Measured static contact angles of water and methylene iodide on gold and aluminum oxide surfaces.....</b>	<b>104</b>
<b>Figure 7.10: TEM high resolution micrograph of Al/AO cross-section area. Left: overall view of the cross section and diffraction pattern from the metal layer. Right: a zoom-in to show clear lattice imaging. ....</b>	<b>106</b>
<b>Figure 7.11: GIWAXD profiles for a PHB crystalline film on gold (A), a PHB crystalline film on AO (B), a PHBHx(13mol%) film on gold (C), and a PHBHx(13mol%) film on AO (D). ....</b>	<b>108</b>

<b>Figure 7.12: A simplified schematic to illustrate crystal orientation profiles in PHB and PHBHx(13mol%) ultrathin films on gold (left) and aluminum (right). Edge-on crystal (yellow) and flat-on crystal (blue).</b> .....	111
<b>Figure 8.1: XPS O 1s profiles of AO surface (before water treatment) and PB (after water treatment) surfaces.</b> .....	114
<b>Figure 8.2: (A) carbonyl stretching region of aPHB ultrathin films on AO and PB. (B) Peak decomposition for aPHB on AO. (C) Peak decomposition for aPHB on PB.</b> .....	115
<b>Figure 8.3: (A) carbonyl stretching region of aPHB on AO with immersing time at 0, 10, 20, and 70 mins in chloroform (B) Plots of wavenumber shift and the estimated film thickness as a function of immersing time.</b> .....	117
<b>Figure 8.4: Peak decomposition for carbonyl stretching region of aPHB films on PB at immersing times of 10 mins(A), 20 mins(B), and 70 mins(C).</b> .....	118
<b>Figure 8.5: Schematic processing procedures from spin coating to melt crystallization.</b> .....	118
<b>Figure 8.6: Carbonyl stretching region for supercooled amorphous iPHB on AO and PB (2mins after melt)</b> .....	119
<b>Figure 8.7: (A) Peak decomposition for the supercooled amorphous iPHB film on AO. (B) Peak decomposition for the supercooled amorphous iPHB film on PB</b> .....	120
<b>Figure 8.8: (A) Peak decomposition of carbonyl stretching region for iPHB on AO after 10-day crystallization at 23 C. (B) Peak decomposition of carbonyl stretching region for iPHB on PB after 10-day crystallization at 23 C.</b> .....	121
<b>Figure 8.9: (A) GIWAXD profile for iPHB on AO after 10-day crystallization at 23 C. (B) GIWAXS profile for iPHB on PB after 10-day crystallization at 23 C. (C) 1D profiles of iPHB on AO versus on PB. The broad peak at a high angle is from scattering from glass substrates.</b> .....	123
<b>Figure 8.10: POM images of crystalline iPHB on AO (A) and PB (B).</b> .....	123

**Figure 9.1: Molecular structure of 1-methoxy-2-(methylthio)ethane and two conformers. .... 127**

## ABSTRACT

Bacterially derived, biodegradable poly[(R)-3-hydroxybutyrate] (PHB) and its random copolymer poly[(R)-3-hydroxybutyrate-*co*-(R)-3-hydroxyhexanoate] (PHBHx) have gained substantial interest as environmentally friendly polymers. PHB and PHBHx serve as a carbon and energy storage material *in vivo* in micro-organisms. However, neat PHB suffers from an excessively high crystallinity, leading to high brittleness, a high melting point, and subsequent poor processing ability. Incorporating an unexpectedly high amount of 3HHx is required to decrease the crystallinity. These drawbacks limit the application areas for PHB and PHBHx. Why does the homopolymer PHB exhibit high crystallinity, and why does PHBHx require an abnormally high comonomer concentration to decrease the crystallinity? The goal of the current dissertation is to understand the crystallization mechanism for PHB and PHBHx. In addition, novel ways of tuning the crystallization are explored.

The first part of this thesis focuses on understanding the crystallization mechanism of PHBHx by isothermally growing single crystals. Single crystals of PHBHx, with a relatively high (R)-3-hydroxyhexanoate (3HHx) content of 3.9 mol% were grown from dilute solutions over a wide temperature range from -20 °C to 75 °C. PHBHx single crystals were found to adopt the  $\alpha$  crystalline form of the homopolymer for all temperatures. The comonomer, 3HHx, was found to be excluded from the crystal lattice as a non-crystallizable molecular defect. A unique needle-shaped anisotropic growth pattern was identified. This anisotropic growth pattern was

significantly enhanced at  $T_c=20\text{ }^\circ\text{C}$ , wherein the unit cell packing velocity along the  $a$  direction is approximately 55 times faster than that along the  $b$  direction.

The second part of this thesis focuses on investigating a crystallization retardation phenomenon of PHB and PHBHx ultrathin films on an aluminum oxide (AO) surface. Infrared reflection absorption spectroscopy (IRRAS) was used to study crystallization kinetics of polymer films. Avrami analysis showed that the crystallization rate constant  $k$  ( $\text{min}^{-1}$ ) for all of the polymers on AO is approximately 3 to 4 orders of magnitude less than that found for the same polymers on gold. The retardation mechanism was explained as being a sum of the dipole–dipole interactions of  $-\text{C}=\text{O}$  of PHB or PHBHx and the  $-\text{O}-\text{Al}-\text{O}-$  groups of AO coupled with the rigid disordered amorphous nature of the AO surface. In the most recent development, a poorly crystalline aluminum oxide hydroxide, or, pseudoboehmite (PB) was found to be capable of forming intermolecular H-bonding with PHB ultrathin films. Grazing incident wide-angle X-ray diffraction and polarized optical microscopy results indicate the crystallization of PHB films is inhibited for a longer term. These findings are believed to have practical potential to allow tuning of PHB and PHBHx crystallinity.

## **Chapter 1**

### **BACKGROUND**

#### **1.1 Plastic Pollution Overview**

Since the introduction of Bakelite by Leo Baekeland in 1907, synthetic polymers have found extensive uses in our daily life ranging from commodity products such as plastic bags, to performance products such as Kevlar<sup>TM</sup> fibers. The polymer revolution, originating in the 1950s, has helped to shape modern society. Compared with metallic and ceramic materials, polymers have several advantages including low density, processability (for example, lower temperature operation and solvent processing), and functionality. However, most of the polymers currently used on a largescale are not readily degradable under ambient conditions after disposal, which has led to a severe environmental problem. Plastic pollution is especially concerning in aquatic systems, such as lakes and rivers, underwater systems, and oceans. For example, in the ocean, plastic waste tends to float on the surface, leading to direct exposure to sunlight. This can cause a UV (Ultraviolet) induced photodegradation process which decomposes relevant polymers into small molecules, such as BPA (bisphenol A) and PS (polystyrene) oligomers, both of which are toxic to organisms and animals. In addition, a more pressing issue is the photodisintegration of plastics to small micro plastic particles without full photochemical degradation. Micro plastics are ingested by fish and birds, as well as by humans via sea salt contamination. Existing ways to process plastic waste include incineration, recycling, and transforming waste polymers into other useful materials. Incineration is not a

favorable approach due to its high energy cost. The latter two approaches to process waste are limited to specific types of polymers.

In addition, the polymers being used today are mostly derived from petroleum, a non-renewable monomer resource. Though the debate on the depletion of petroleum has been ongoing for years, the shifting from petroleum-based polymers to sustainable polymers is desirable and ongoing. Using renewable sources also helps to reduce the global CO<sub>2</sub> footprint of these materials. Current research efforts in both academia and industry are focusing on developing environmentally friendly polymers with good sustainable and degradable profiles.

Currently, environmentally friendly polymers derived from renewable sources can be, in general, classified into two major categories.<sup>1,2</sup> The first category includes polymers not directly derived from nature, but the associated monomers are derived from renewable resources. Polylactic acid (PLA), for example, is a representative of this category, with its monomers derived from starch (such as corn). The second category involves native polymers which can be directly separated from renewable resources, such as starch. However, it is not ideal for use as a plastic due to its high hydrophilicity. In addition, cellulose and cellulose derivatives also fall into the second category. For cellulose, strong hydrogen bonding and a rigid backbone structure prevent melt processing. Chemical modification of cellulose (e.g., cellulose acetate) to make it melt processable also destroys its biodegradability. PLA, in the first category, has been used as a plastic; however, its glass transition temperature ( $T_g$ ) is actually too low for many applications unless it is structurally modified. In addition, rigorously speaking, PLA can only be considered as compostable plastic, as it does not spontaneously biodegrade.

## 1.2 Polyhydroxyalkanoate (PHA)

Polyhydroxyalkanoates (PHA) belong to an aliphatic polyester family which can be made via either chemical or biological synthesis. Due to the high cost of the pure enantiomer monomer, chemical synthesis has not been undertaken commercially. Currently used PHAs are mostly derived from biological synthesis. Microorganisms such as bacteria and fungus have been used to biosynthesize PHA. If it is synthesized bacterially, the feed stock can be renewable materials such as fatty acids (e.g. canola oil) and sugars (e.g. starch and glucose). The most intriguing property of PHA is its superior biodegradability. It was found that PHA can be degraded in both terrestrial (e.g. soil) and aquatic (e.g. ocean) environments. This unique degradation profile is due to the fact that the bacteria/enzymes responsible for PHA degradation are widely present in both terrestrial and aquatic environments. The depolymerases excreted from these bacteria are the key to the degradation process.

The general backbone structure of PHA is shown in Figure 1.1.<sup>3</sup> The very first identified PHA, and also the most abundant PHA is polyhydroxybutyrate (PHB), which was first found in *bacillus* as early as 1923 by Lemoigne.<sup>4</sup> The specific molecular structure of PHB is shown in Figure 1.2. Bacterially synthesized PHB has its repeating unit, 3-hydroxybutyrate (3HB), exclusively in the R configuration due to a unique metabolic process. This chiral configuration gives PHB a very high chain regularity, which leads to high crystallinity. As shown in Figure 1.3, PHB melt crystallized film can have a crystallinity as high as 60%.

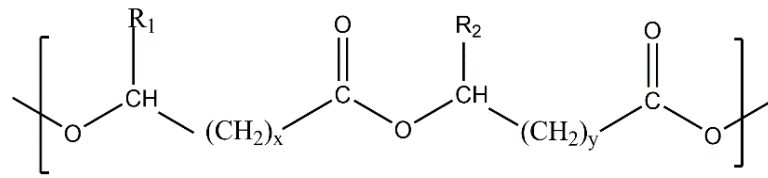


**Figure 1.1: General structure of PHA. R<sub>1</sub> and R<sub>2</sub> are alkyl groups with C<sub>1</sub> to C<sub>13</sub>. x and y = 1 to 4.**

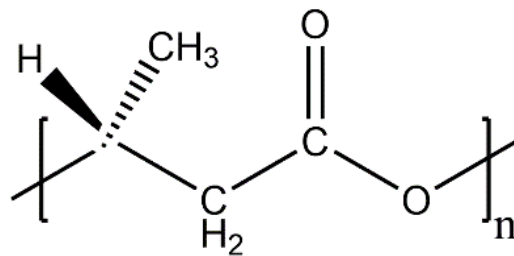


**Figure 1.2: molecular structure of PHB**

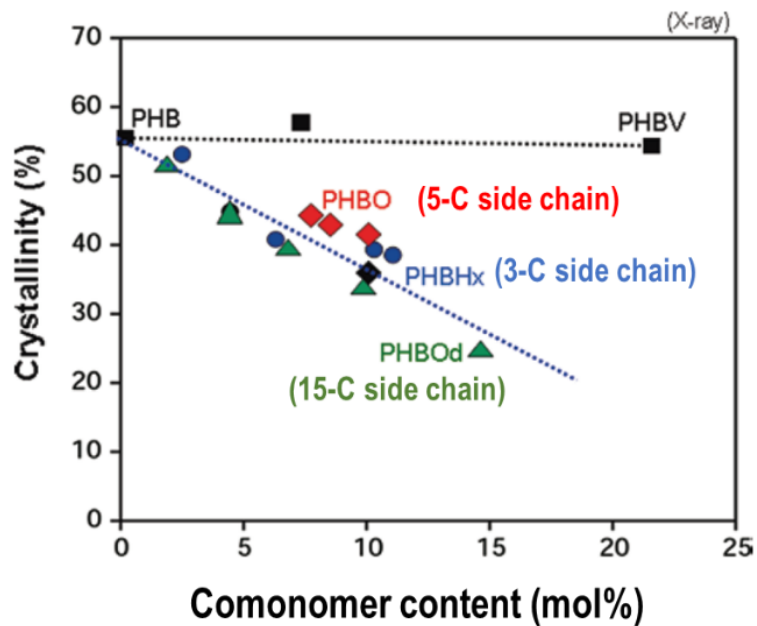


**Figure 1.3: Crystallinity of PHB copolymers as a function of comonomer content.<sup>5</sup>**

The high crystallinity of PHB also results in a high melting temperature (between 170 to 180 °C), which is close to the thermal decomposition temperature. This makes thermal processing of PHB very difficult. In addition, the high crystallinity also causes a significant brittleness, thereby significantly limiting applications.

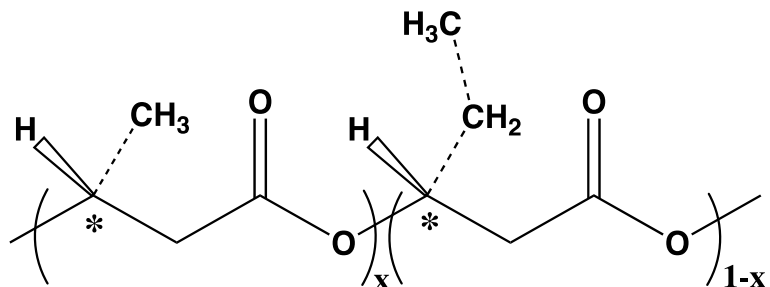


**Figure 1.4: molecular structure of PHBV**

Extensive efforts have been made to improve the physical properties of PHB. Inspired by polyethylene (PE) copolymers, where short-side-chain comonomers, such as a pentene comonomer, are copolymerized into the backbone to disrupt PE crystallization, Poly(3-hydroxybutyrate-*co*-3-hydroxyvalerate) (PHBV) (molecular structure shown in Figure 1.4) was developed. However, it turned out that the crystallinity decrease of PHBV from PHB is minimal, even with over 20mol% 3HV comonomer content, as shown in Figure 1.3. This unexpected and disappointing result was later found to be due to a scientifically important crystallization mechanism called isodimorphism, meaning 3HB and 3HV comonomer can co-crystallize into a crystal lattice over the entire composition range.

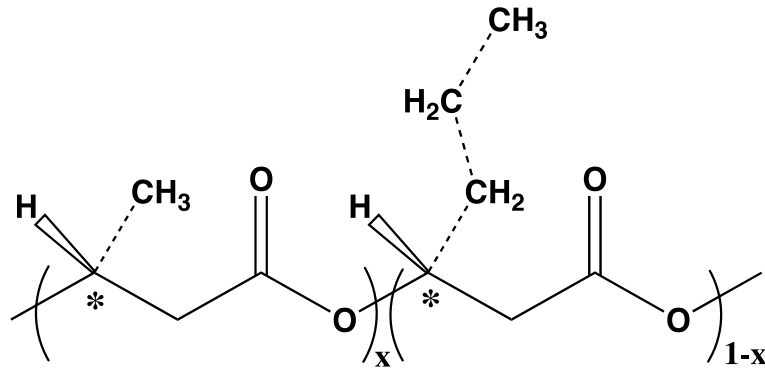


**Figure 1.5: molecular structure of PHBHx**

Later, after realizing that PHBV is isodimorphic, an attempt was made to make PHB random copolymers with the second comonomer having an even longer side chain. To that end, a series of medium- or long-side chain PHB copolymers were developed by Dr. Isao Noda at Procter & Gamble, and later at Danimer Scientific. As shown in Figure 1.5, when the side chain group of the comonomer has at least 3 carbons, the crystallinity drop from PHB is significant. This class of PHB copolymers is now commercialized under the trade name Nodax™. Nodax™ shows a lower crystallinity and much improved physical properties compared to PHB or PHBV. Poly[(R)-3-hydroxybutyrate-*co*-(R)-3-hydroxyhexanoate], or PHBHx is a representative Nodax™ copolymer. Depending on the comonomer content, PHBHx can have a melting point well below 130 °C, and exhibits elastomer like mechanical properties. Hence, Nodax™ is a promising candidate for real commercial applications.

However, as shown in Figure 1.3, the lowering of the crystallinity of PHBHx with increased 3HHx content is still not as efficient as expected. For example, to reach a crystallinity of 30wt%, more than 10mol% 3HHx is required, which is an unexpectedly high comonomer content compared with copolymers of PE. For PE, in

contrast, it was found a 2-3 mol% pentene comonomer content was sufficient to reach a crystallinity level of 30wt%.<sup>6,7</sup>

### **1.3 Research Overview**

The fundamental questions remain; why does PHBHx require an abnormally high comonomer concentration to lower crystallinity, and why does the PHB homopolymer exhibit exceptionally high crystallinity? These are questions to be answered in the current dissertation. In the work presented here, I describe the mechanisms of PHB and PHBHx crystallization at the molecular level and how the 3HHx comonomer concentration influences PHBHx crystallization. In addition, efforts directed towards decreasing PHB crystallinity have been mainly focused on making new copolymers, but no other approaches have been studied. Thus, alternative approaches to tuning PHB and PHBHx crystallization are also explored in this dissertation

#### **1.3.1 Understanding PHBHx crystallization in solution grown single crystals**

In this crystallization mechanism study, PHBHx single crystals will serve as the focus. Depending on the processing conditions, semi crystalline polymers can crystallize into different hierarchical structures, including spherulites. The basic building block is typically a lamellar crystal.<sup>8-10</sup> Understanding how the lamellar crystals form will provide a good understanding of how the polymer crystallizes. Polymer lamellae are two-dimensional in nature with the chain folding direction usually only tens of nanometers thick.<sup>11</sup> Due to this chain folding, the crystal will normally not grow much along the polymer backbone direction.

As shown in Figure 1.6, lamellar crystals can be prepared by either melt crystallization or solution crystallization. However, studying an individual lamellar crystal from melt crystallization is difficult because melt derived lamellar crystals are buried in spherulites, which makes it difficult to isolate them due to chain entanglement. Alternatively, isolated lamella can be prepared by crystallization of the polymers from a super dilute solution. An isolated single layered crystal is what we will refer to as a polymer single crystal. Transmission electron microscopy (TEM) can be used to visualize solution grown single crystals. It is worth noting that polymer single crystals are not rigorously single crystals in the classical sense since they still contain substantial non-crystalline domains near the fold surface. In this dissertation, a crystallization mechanism for PHBHx grown from dilute solution is presented.

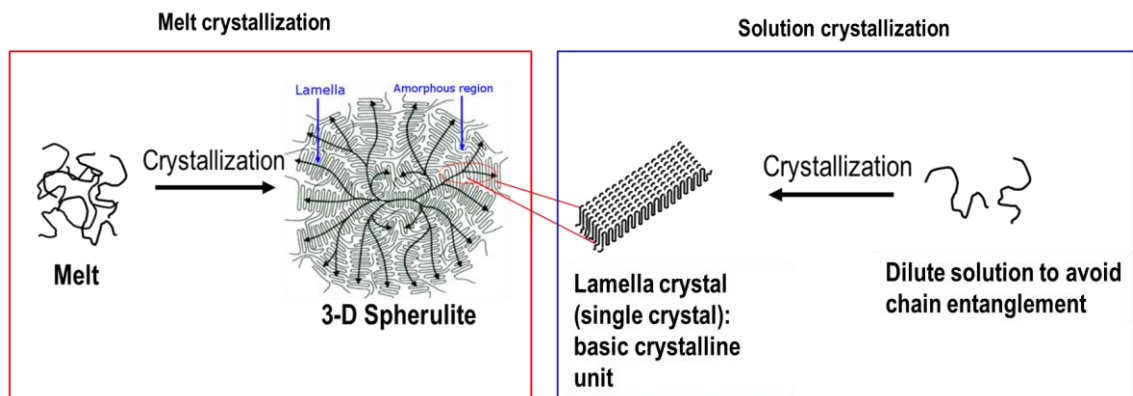


**Figure 1.6: Schematic illustrating two processing methods to prepare lamellar single crystals: melt crystallization(left) and solution crystallization (right)**

### **1.3.2 Using aluminum oxide (AO) and pseudoboehmite (PB) to retard or inhibit PHB and PHBHx crystallization**

In an accidental discovery, an aluminum foil surface was found to retard PHBHx thin film crystalline growth significantly. This process was quantified by making aluminum coated slides with spin coated PHB and PHBHx ultrathin films. Reflection absorption infrared spectroscopy (IRRAS) was used to monitor crystallization profiles of the thin films at room temperature. Since aluminum is replacing stainless steel as a molding material in the polymer processing industry, this discovery has practical implications. Pseudoboehmite (PB) is a poorly ordered crystalline aluminum oxide hydroxide which was found to inhibit PHBHx thin film crystallization.<sup>12</sup> PB is a low cost, source abundant mineral, and its use has the potential to allow tuning of PHB and PHBHx crystallinity.

## **1.4 Organization**

This dissertation consists of two major parts. Part 1 will focus on studying solution grown, single crystals of PHBHx. Part 2 will be focused on studying crystallization retardation and inhibition of PHB and PHBHx films on substrates made of aluminum oxide, other metal oxides, and pseudoboehmite. Chapter 2 presents the major materials and characterization methods used for this research. Chapter 3 covers the development of single crystal preparation methods used throughout the single crystal growth studies. Chapter 4 describes investigations of PHBHx crystallization mechanisms by isothermally growing PHBHx(3.9mol%) single crystals as a function of crystallization temperature. Chapter 5 provides detailed insights into how 3HHx comonomer content influences the solution crystallization behavior of PHBHx.

Part 2 is described in chapters 6, 7, 8, and 9. Chapter 6 explains the crystallization of PHB and PHBHx thin films on metal and metal oxide flat surfaces

while chapter 7 describes the crystallization retardation of PHB and PHBHx thin films on aluminum oxide substrates. Finally, chapter 8 covers the crystallization inhibition of PHB and PHBHx thin films on pseudoboehmite.

## Chapter 2

### MATERIALS AND CHARACTERIZATION METHODS

All the experimental materials including polymers and solvent are described in this chapter. Major characterization techniques used throughout this dissertation are also described.

#### 2.1 Materials

##### 2.1.1 PHBHx

Our laboratory currently has a series of PHBHx powders with 3HHx concentrations ranging from 3.9mol% to 13mol%, as well as multiple molecular weights with the same composition. A PHBHx library is listed in Table 2.1. Underscored polymers are those used in these studies. All the samples were generously provided by the Procter & Gamble Company (Cincinnati, OH, USA). The statistically random distribution of both the monomer units 3HB and 3HHx within the copolymer chain has been confirmed using electrospray ionization multistage mass spectrometry (ESI-MS<sub>n</sub>) as reported previously.<sup>13</sup> Chemically synthesized, atactic PHB (aPHB) was also provided by the Procter & Gamble Company.

**Table 2.1: A list of all PHBHx samples provided by Proctor and Gamble with their weight averaged molecular weight ( $M_w$ ), melting temperatures ( $T_m$ ), and polydispersity indices (PDI)**

<b>3HHx molar concentration[mol%]</b>	<b><math>M_w</math> [g/mol]</b>	<b><math>T_m</math> [°C]</b>	<b>PDI</b>
<u>3.9</u>	843,168	134.4(28%)/148.43(72%)	-
<u>5.8</u>	461,387	143.7/128	2.3
5.8	1,174,724	147.51	-
6.2	656,391	129.6/143.26	-
6.9	633,414	138.74	1.9
<u>7.6</u>	624,939	-	-
<u>9.4</u>	454,501	140.94	1.8
11.9	1,388,161	127.3/142	-
12 to 13	-	-	-
<u>13</u>	840,000	-	-

### 2.1.2 Other materials

Isotactic PHB with a 540,000 g/mol weight-averaged molecular weight was purchased from Sigma Aldrich, and used without further purification. Chloroform and ethanol were purchased from Fisher Scientific while, methylene iodide (MI), used for contact angle measurements was purchased from Sigma-Aldrich. Gold coated glass substrates were purchased from Platypus Technologies LLC and aluminum, silver, and copper coated glass substrates were purchased from Deposition Research Lab Inc.

## 2.2 Characterization

### 2.2.1 Transmission electron microscopy (TEM)

A Tecnai G2-12 TEM operating at 120 kV was used to investigate the morphology and crystal structure of PHBHx single crystals (Chapters 3-5). Droplets of crystal suspensions were deposited on a 300-mesh copper-grid substrate with an ultra-thin coated carbon film. The camera length used for recording the electron diffraction pattern was 2.1 m. A polycrystalline aluminum standard sample with a cubic lattice

$a=0.4041$  nm (determined by XRD), was used for calculating the unit cell parameters of PHBHx crystals.

In Chapter 6, a replica of the aluminum substrate cross section was prepared using a Focused Ion Beam (FIB) lift-out approach (Zeiss Auriga 60 dual beam SEM) in order to examine the structure of the aluminum substrate surface. The outmost layer was protected by sputtering a gold protection layer to prevent potential beam damage. A Talos<sup>TM</sup> F200C TEM operated at a voltage of 200 kV was used for recording the high-resolution image of the aluminum/aluminum oxide interfacial region.

### 2.2.2 X-ray diffraction

**Powder diffraction.** To study the crystal structure of PHBHx single crystals (Chapter 4), a Bruker D8 diffractometer was operated at 40 kV and 40 mA with an X-ray wavelength of 1.5418 Å (Cu K $\alpha$  radiation). One-dimensional, XRD experiments in reflection geometry (theta-theta) mode were conducted by positioning a crystal mat flat on the sample stage. Diffraction profiles were recorded by scanning  $2\theta$  from 10 to 40° with a 0.05° resolution and a 0.5 s exposure time per step.

**Grazing incident wide angle X-ray diffraction (GIWAXD).** For the crystal orientation study of PHBHx thin films (Chapter 6 and 7), a Xeuss 2.0 X-ray diffractometer equipped with a two-dimensional detector was used to examine the in-plane and out-of-plane crystallite orientation profiles. The instrument was operated at a current of 0.6 mA and a voltage of 50 kV using Cu K-alpha radiation with an X-ray wavelength of 0.154 nm. The grazing angle used was 0.2°, which is approximately 1.2 times the critical angle at these experimental conditions and ensures that the X-ray

beam penetrates the entire sample. All GIWAXD experiments were conducted at room temperature.

### **2.2.3 Fourier transform infrared (FTIR) spectroscopy**

**FTIR in ATR mode** (Chapter 4). Infrared experiments were conducted using a Thermo Nicolet 670 Nexus FT-IR spectrometer with a DTGS detector operating in an attenuated total reflection (ATR) mode using a Specac Golden Gate ATR accessory. The spectra were obtained by averaging 128 scans from  $600\text{ cm}^{-1}$  to  $4000\text{ cm}^{-1}$  with a resolution of  $2\text{ cm}^{-1}$ . The raw spectra were then processed using the Essential FTIR software for baseline correction and advanced ATR correction.

#### **Infrared reflection-absorption spectroscopy (IRRAS)** (Chapters 6-8).

IRRAS measurements were conducted using a Thermo Nicolet 670 Nexus FT-IR spectrometer with a DTGS detector. A specular reflectance accessory (PIKE Tech. 80Spec™) was used with a fixed incident angle of  $80^\circ$ . Gold and aluminum mirrors at  $80^\circ$  incident angle have the same absorption factor, as shown by Greenler.<sup>14</sup> Each spectrum was collected by averaging 32 scans with a  $4\text{ cm}^{-1}$  resolution from  $600\text{ cm}^{-1}$  to  $4000\text{ cm}^{-1}$ . The as-collected raw spectra were baseline-corrected using the Essential FTIR software.

### **2.2.4 X-ray photoelectron spectroscopy (XPS)**

The XPS spectra were collected on a Thermo Scientific K-Alpha XPS instrument with an Al  $K\alpha$  X-ray source at an energy of 1486.6 eV at a base pressure below  $5 \times 10^{-8}$  Torr. The takeoff angle was  $90^\circ$  with respect to the analyzer, ensuring maximum collection efficiency. The survey spectrum was collected with an energy range of 0 to 1200 eV. The high-resolution spectra for C 1s, O 1s and Al 2p were

collected with a pass energy of 20 eV. The data analysis was performed with CasaXPS (version 2.3.16) software. All peak positions and relative sensitivity factors were calibrated to the C 1s peak at 285 eV<sup>25</sup>.

## Chapter 3

### CRYSTALLIZATION METHODS DEVELOPMENT FOR SOLUTION GROWING PHBHx SINGLE CRYSTALS

In this chapter, three crystallization methods used to grow PHBHx single crystals are described. They are 1) isothermal crystallization, 2) self-seeding, and 3) gradual cooling method. The commonalities of these three methods are that they are all based on dilute solutions, with concentrations ranging from 0.01wt% to 0.1wt%. Chain entanglement at such low concentrations is minimal considering the  $M_w$  of these PHBHx polymers (Table 2.1). The fundamental crystallization mechanism for the three methods all involves adding a poor solvent to initiate crystallization of the polymer from solution. This procedure is called poor solvent induced crystallization. The good solvent for PHBHx used here is chloroform, and the poor solvent is ethanol (EtOH). After covering each method, the pros and cons for each method will be discussed.

#### 3.1 Isothermal crystallization method

The key to successfully using this method is to generate a homogeneous supercooled solution at the desired crystallization temperature or  $T_c$  and then letting the polymer slowly crystallizes to form crystal suspension. Two approaches to make supercooled solutions, route 1 and route 2, are shown in Figure 3.1.

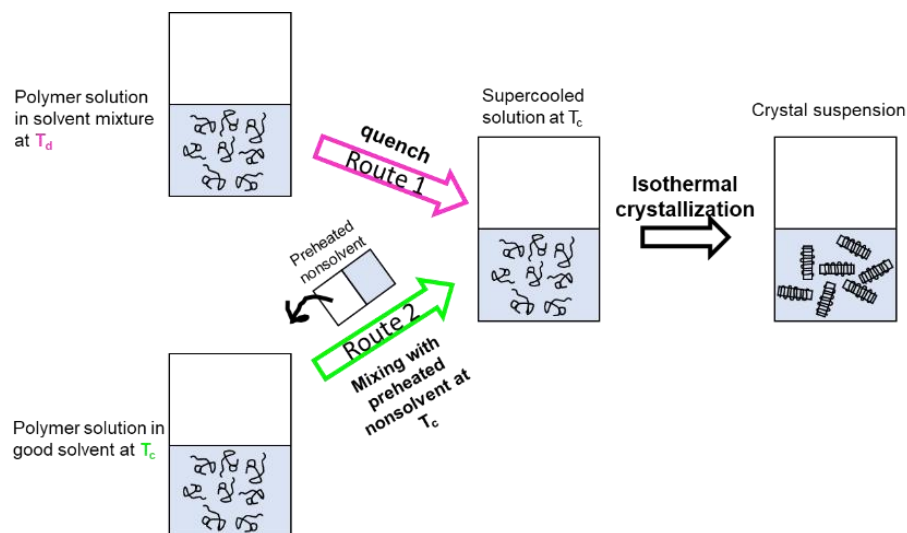


**Figure 3.1: A schematic to illustrate two routes to prepare supercooled solution in the isothermal crystallization method.  $T_d$  is the dissolution temperature.  $T_c$  is the crystallization temperature.**

Route 1 works best for a high  $T_c$  ( $T_c$  close to dissolution temperature, or  $T_d$ ). Specifically, the polymer is first dissolved in a solvent mixture at  $T_d$ , followed by quenching to the desired  $T_c$  in an oil bath. Due to the closeness of  $T_c$  and  $T_d$ , and due to a slow crystallization rate at small supercooling, a supercooled solution at  $T_c$  can be easily formed. Route 2 is designed for a low  $T_c$ , or a large supercooling. Instead of dissolving polymers at an elevated dissolution temperature, the polymer is first dissolved in a good solvent at the desired  $T_c$ . Then, a poor solvent is preheated separately to the same  $T_c$  in another vial and quickly mixed with the polymer solution at  $T_c$  to form a supercooled solution, which is then followed by isothermal crystallization. Route 2 avoids undesired crystallization of high Mw fractions at temperatures higher than  $T_c$  during the long cooling process involved in a low  $T_c$  experiment.

Extensive tests were first carried out to find out the correct solvent ratio of good and poor solvent since an excess amount of poor solvent can cause phase separation. Experimentally, TEM can be used to check whether phase separation or crystallization occurs. Phase separation gives rise to black spherical globules as shown in the inset micrograph in Figure 3.2A. Crystallization gives rise to crystals with a certain geometric shape, as shown in the inset in Figure 3.2B. An easy but empirical way to tell whether phase separation or crystallization occurs is to carefully observe the suspension development process. As shown in Figure 3.2A, typically, a phase separation induced turbidity develops faster (several to tens of minutes), and the suspension is more homogeneously dispersed. In contrast, a crystallization induced turbidity develops much slower (on the order of magnitude of hours or days depending on temperature). As shown in Figure 3.3, after a certain induction time, a small amount of visible “nuclei” crystals develops sporadically in the solution and sometimes also on the vial wall. The growing speed of existing “nuclei” crystals is much faster than forming new “nuclei”, suggesting that the crystal growth process is more time limited than the nucleation process.

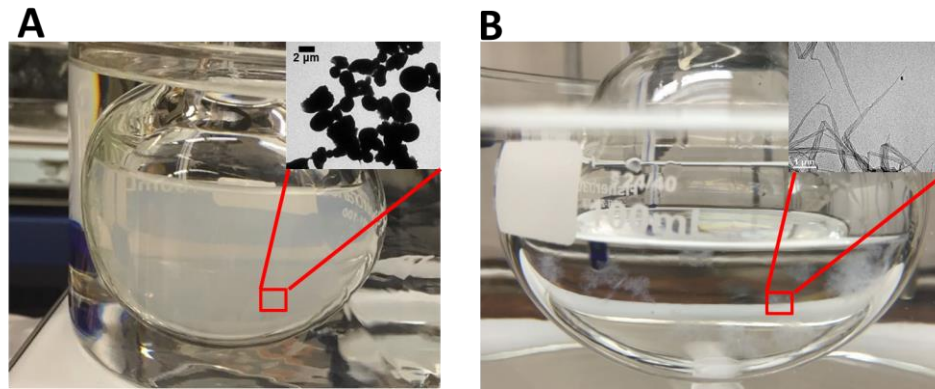


**Figure 3.2: A: suspension formed due to phase separation. Inset(A): micrograph of amorphous globules due to phase separation. B: suspension formed due to nucleation and growth. Inset(B): micrograph of PHBHx crystals.**

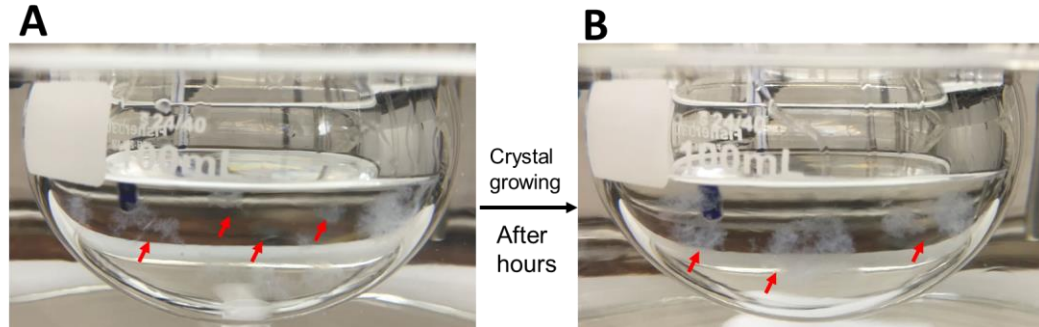


**Figure 3.3: A: white “nuclei” crystals formed in early crystallization stage. B: larger crystal aggregates formed after hours of crystallization.**

### 3.2 Self-seeding method

Self-seeding involves more processing steps compared to isothermal crystallization process. A schematic illustrating the stages in the self-seeding method is shown in Figure 3.4. A precursor crystal is prepared first, by isothermal crystallization or gradual cooling (discussed in section 3.3). Parameters involved in the precursor preparation step are  $T_d$ , and  $T_{c1}$  (crystallization temperature for precursor crystal preparation) if using isothermal crystallization. The next step is the seeding process, which starts by equilibrating the precursor suspension at an initial temperature  $T_i$ . This is followed by heating the precursor suspension to a seeding temperature  $T_s$ , to form seed crystals. The solution is then rapidly transferred to a lower  $T_{c2}$  or gradually cooled to room temperature to induce crystallization.

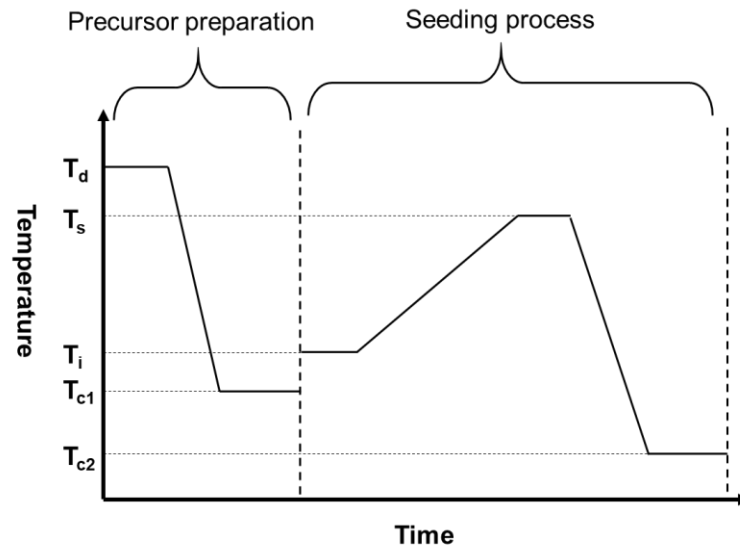


**Figure 3.4:** A schematic illustration of the steps in the self-seeding method.

Based on our experience, the most challenging part is the heating process and the choice of a proper  $T_s$ . Tests show that a too high heating rate causes dissolution of all the seeds resulting in a homogeneous solution instead of a suspension of seed crystals. A too low heating rate is equivalent to annealing the precursor crystals, making them much more difficult to dissolve and makes the whole self-seeding process time-consuming. Determining the precise  $T_s$  is difficult since polymer crystal seeds are not visible by eye and are only visible crystal aggregates.

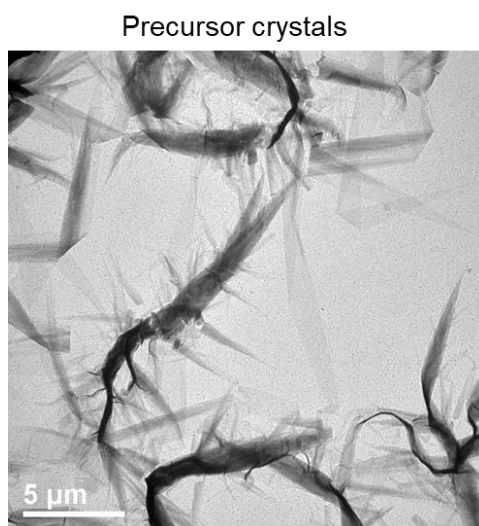
Initially, it was found that during heating, there is no obvious crystal dissolution until a specific temperature. Once this specific temperature is reached, the process from starting dissolution to the absence of visible crystals (total loss of turbidity) typically takes a long time. The seeding temperature is determined after the suspension loses turbidity.

The self-seeding method has been widely used to grow polymer single crystals. However, to our knowledge, there has been no documentation in the literature of the details during the seeding process. Polymer self-seeding is challenging and time-consuming. However, in the development of the self-seeding method to grow PHBHx single crystals, we were able to capture several critical steps during the seeding process near  $T_s$  using TEM. It is hoped that these findings can help other researchers and students gain insights into the polymer self-seeding process and help guide their crystal growth studies.

PHBHx(3.9mol%) was used to study the seeding process near  $T_s$  using pure EtOH and a PHBHx concentration of 0.027 wt%. The isothermal crystallization method was used to grow precursor crystals with  $T_{d1}=110$  °C, and  $T_{c1}=70$  °C. The seeding process started at  $T_i=70$  °C with a heating rate of 30 °C/hr. Once the solution

reached  $T_s$ , the sample was rapidly removed from the oil bath and allowed to cool to 20 °C in the air. Five experiments were conducted as a function of  $T_s$ .

A TEM image of precursor crystals is shown in Figure 3.5. They exhibit a needle shaped growth habit. Both single layer and multiple layered crystals are observed. Irregular growth habits such as branching, and folding can be identified. Size uniformity of the crystals is relatively poor.



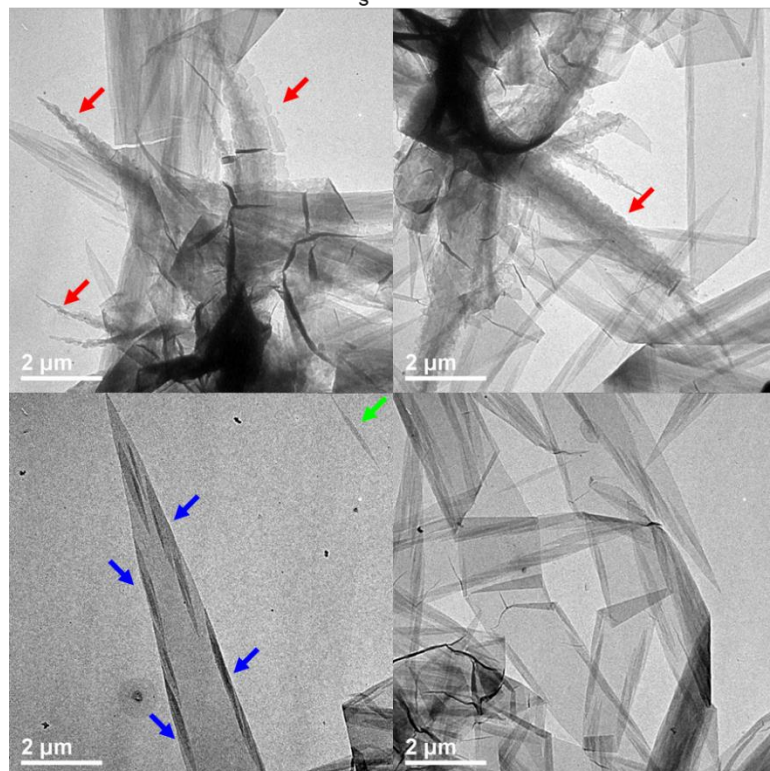
**Figure 3.5: TEM image of PHBHx(3.9mol%) precursor crystals**

Figure 3.6 shows self-seeded crystals grown at  $T_s = 95$  °C. Crystals with a similar size as the precursor crystals were found, suggesting precursor crystals still exist. A serrated structure can be frequently seen along the lateral side of the precursor crystals, as indicated by the red arrows in Figure 3.6. These notches suggest that during the seeding process, the dissolution of the lamellae starts from the edges. A green arrow indicates a well-defined but small-sized self-seeded single crystal,

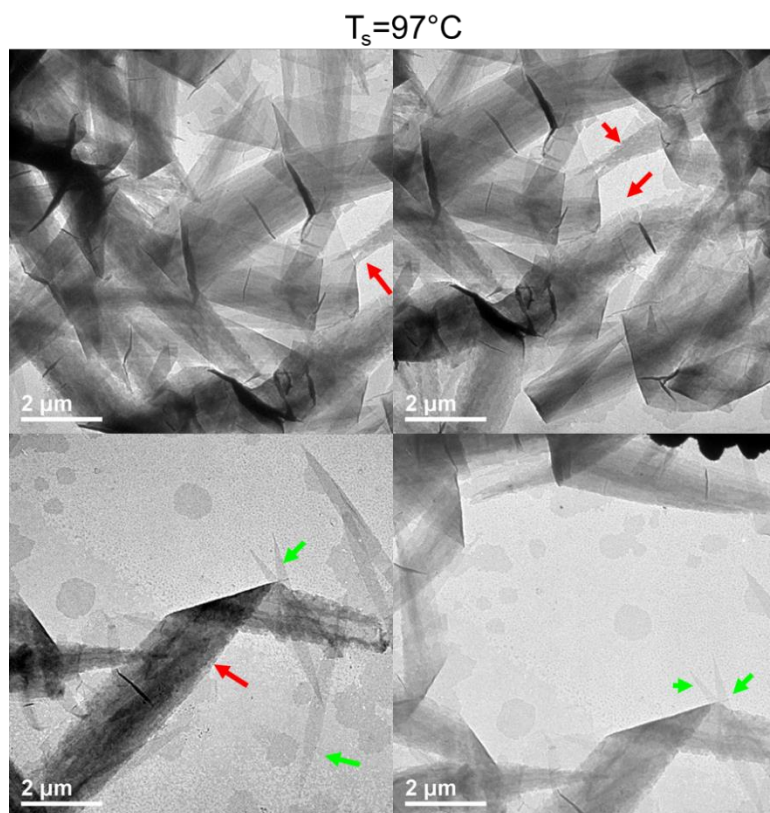
suggesting seeds are indeed created at  $T_s = 95$  °C. Interestingly enough, similar small self-seeded crystals were found to develop more frequently on the lateral edge of the precursor crystals, as indicated by blue arrows. Reasons for the formation of these small self-seeded crystals attached to the lateral edges are not well understood. One possible explanation is that the dissolution of the crystal near the lateral edge creates some coiled chains which cannot migrate into solution because part of the chain is still anchored to the main crystal. When crystallization occurs, for the 2<sup>nd</sup> time these chains will crystallize near their original location. Thus, at this low seeding temperature ( $T_s = 95$  °C), well isolated seeded single crystals are only rarely seen, suggesting that at this temperature the sample is in the early stage of forming a seed.

Figure 3.7 shows the case for  $T_s = 97$  °C where more self-seeded isolated single crystals can be identified as indicated by green arrows, suggesting that more seeds were actually generated at this temperature.

$T_s=95^\circ\text{C}$



**Figure 3.6: PHBHx (3.9mol%) crystals grown using self-seeding method with a  $T_s$  of  $95^\circ\text{C}$ . Red arrows indicate notches developed on the lateral side of lamellae. Green arrow indicates a well-developed self-seeded lamellae. Blue arrows indicate self-seeded crystals developed near lamellar lateral sides.**



**Figure 3.7: PHBHx (3.9mol%) crystals grown using self-seeding method with a  $T_s$  of 97 °C. Red arrows indicate notches developed on the lateral side of lamellae. Green arrows indicate a well developed self-seeded lamellae.**

$T_s=101^\circ\text{C}$

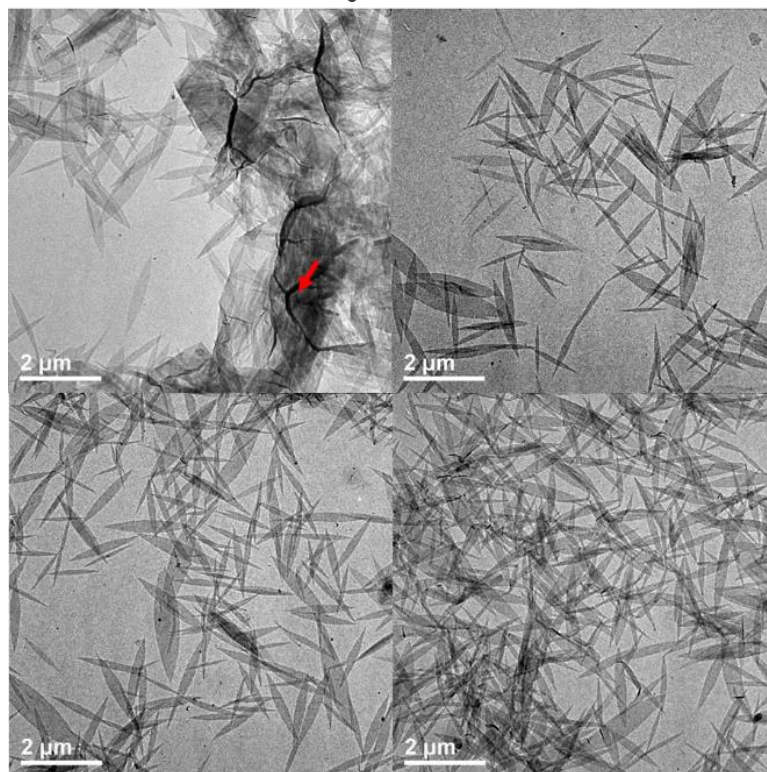


**Figure 3.8: PHBHx (3.9mol%) crystals grown using self-seeding method with a  $T_s$  of 101 °C. Red arrow indicates residual precursor crystals.**

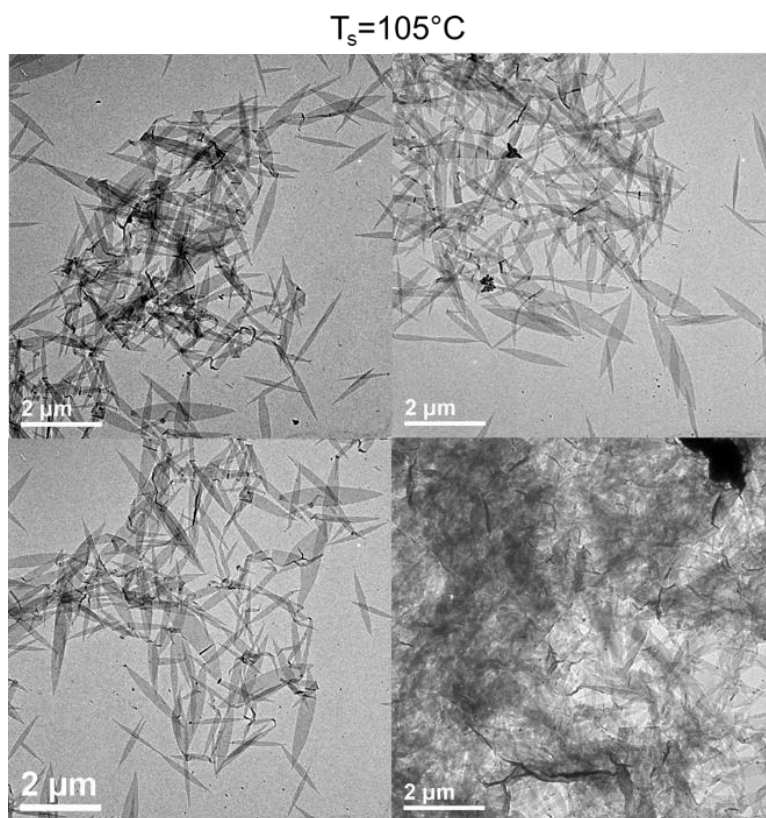


**Figure 3.9: PHBHx (3.9mol%) crystals grown using self-seeding method with a  $T_s$  of  $105^\circ\text{C}$ .**

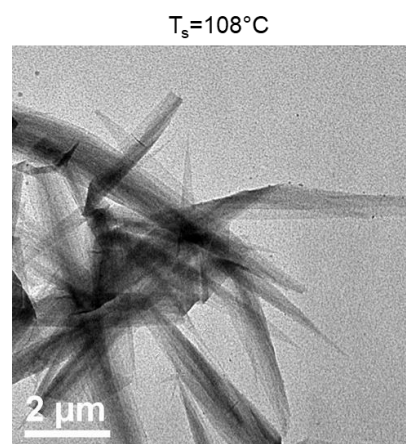


**Figure 3.10: PHBHx (3.9mol%) crystals grown using self-seeding method with a  $T_s$  of  $108^\circ\text{C}$**

Figure 3.8 shows the results for crystallization at  $T_s = 101$  °C. The red arrow indicates precursor crystal residue, which can still be seen. However, the population of well isolated single crystals is significantly increased, suggesting that  $T_s = 101$  °C is a good seeding temperature. When increasing  $T_s$  to 105 °C (shown in Figure 3.9), a similar crystal population profile was observed as for  $T_s = 101$  °C. In addition, at such high  $T_s$ , precursor crystal residues can still be seen. For an even higher  $T_s = 108$  °C, as shown in Figure 3.10, no seeded crystals are observed, but giant crystals morphologically similar to precursor crystals can be seen. This suggests that  $T_s = 108$  °C is so high that all seeds are dissolved, resulting in a homogeneous solution. Once the temperature is reduced, precursor crystal develops again.

Based on the observed crystal morphology during the seeding process, a schematic shown in Figure 3.11 was generated to illustrate the dynamics of the seeding process. During seeding, lamellae dissolution starts from the crystal periphery, forming both crystal seeds and coiled chains (route 1). With increasing temperature, the precursor crystals decrease in size to become crystal residue, seeds, and coiled chains (route 2). In the interim, the formed seeds decrease in size to become smaller seeds and coiled chains (route 3).

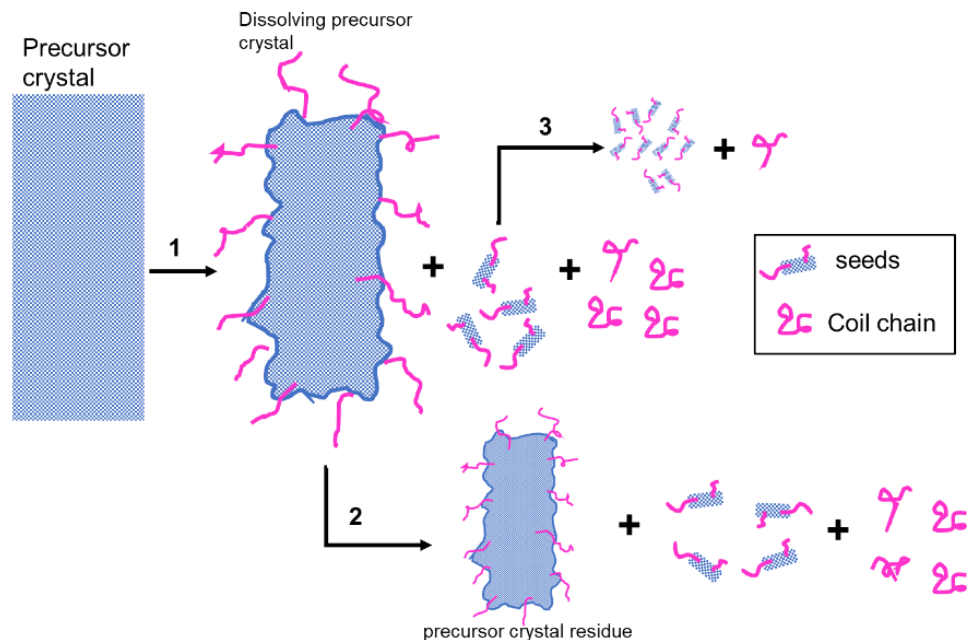


**Figure 3.11: A schematic to illustrate a proposed seeding process**

Based on the proposed seeding process, it is clear that the ultimate goal for self-seeding is to maximize the number of the seeds and minimize the precursor crystal residue and random coil chains, which is a temperature dependent dynamic process. Theoretically, a steady state exists where the number of seeds reaches a maximum. However, it is challenging to determine that point due to hot plate temperature control limitations. In our experiments, precursor crystal residues were always observed, and it is difficult to create a pure seed suspension.

### **3.3 Ultrasonication assisted self-seeding process**

In the seeding process, precursor dissolution starts on the crystal periphery. During the seeding process, there is also annealing of the crystals (perhaps lamellar thickening), making the undissolved part harder to be dissolved, and the already

formed seeds can be completely dissolved forming random coiled chains. This situation is unwanted. Hypothetically, if the dissolution can simultaneously initiate throughout the whole crystal (not limited to crystal periphery), the dissolution process may be shortened, and more seeds may be generated in a more uniform way.

It was found, prior to the seeding process, that if the precursor suspension is treated with ultrasonication at room temperature, more uniform self-seeded crystals can be obtained. Figure 3.12 shows the fragmented crystals of PHBHx(3.9mol%) after ultrasonication for 10mins. Keeping all the other seeding parameters constant, Figure 3.13 shows the self-seeded crystals grown with varying sonication times of 0 min, 4 min, and 10 mins. A longer sonication time gives rise to more and smaller self-seeded crystals, suggesting more seeds were generated during the seeding process. In addition, smaller PHBHx(3.9mol%) crystals appear having a lower aspect ratio. The sonication process may potentially induce molecular weight degradation. To check this possibility, we reused the same sample to grow precursor crystals, as shown in Figure 3.14. The crystal resembles typical PHBHx(3.9mol%) precursor crystals morphologically, suggesting no  $M_w$  degradation had occurred. However, HPLC examination is needed to determine definitive evidence that there was no  $M_w$  degradation.

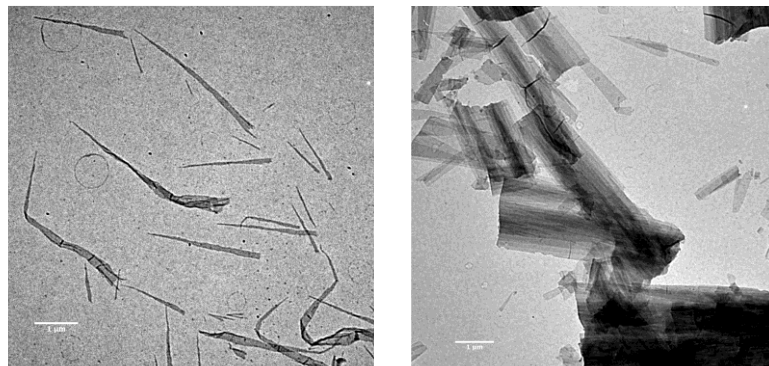


**Figure 3.12: Fragmented PHBHx(3.9mol%) precursor crystals after ultrasonication for 10mins.**

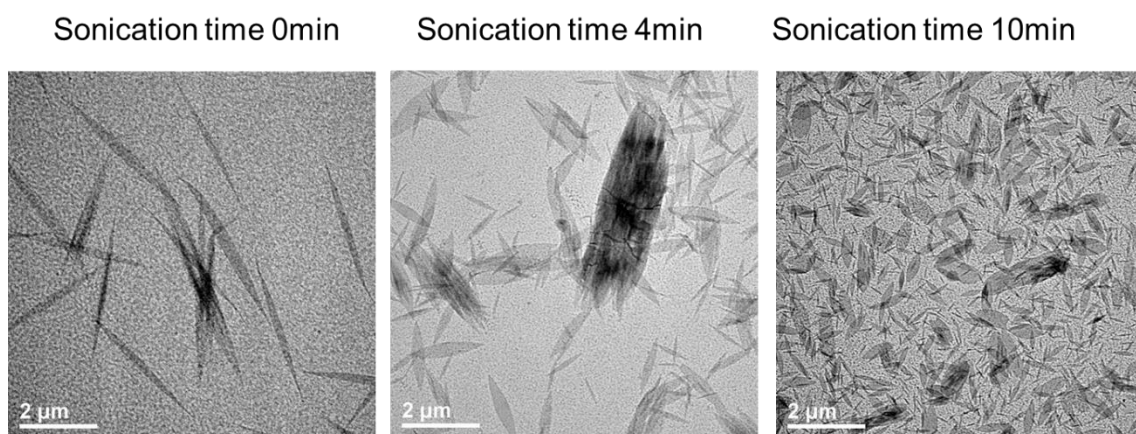


**Figure 3.13: PHBHx(3.9mol%) single crystals made by the ultrasonification assisted method as a function of sonication time.**

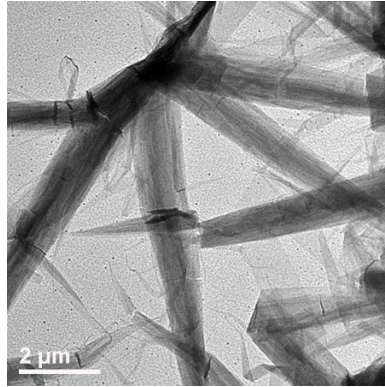


**Figure 3.14: PHBHx(3.9mol%) precursor crystals grown from ultrasonicated polymers.**

In ultrasonication assisted self-seeding experiments, an intriguing crystal morphology is frequently observed as shown by the green boxes and arrows in Figure 3.15. Careful observation indicates they consist of self-assembled, orderly packed individual self-seeded crystals. The self-assembled structure is comparable in size to the fragments of precursor crystals in Figure 3.12. Creating orderly packed polymer single crystals has been challenging. This is the first time such self-assembled structures have been generated. In addition, the observation of this structure supports our hypothesis that ultrasonication presumably enables dissolution of the precursor crystal from multiple locations instead of from the crystal periphery only. A proposed mechanism is schematically shown in Figure 3.16. It is seen that ultrasonication can break down precursor crystals and hence, this process may also be capable of creating internal defects in a crystal. These defects give rise to a crystal consisting of small crystalline domains with the defects arranged as grain boundaries (blue dashed line in the defective crystal schematic in Figure 3.16). The defect crystal dissolves in an outside-in fashion starting from these grain boundaries, to form seeds. The coiled

chains that form cannot go into solution because they are linked to the seed crystal. These inter-seed chains also help the seeds maintain a partially ordered network. Once subsequent crystallization occurs, the coiled chains linked to the seeds will crystallize, resulting in a self-assembled like structure with individual self-seeded polymer single crystals packed in an orderly fashion

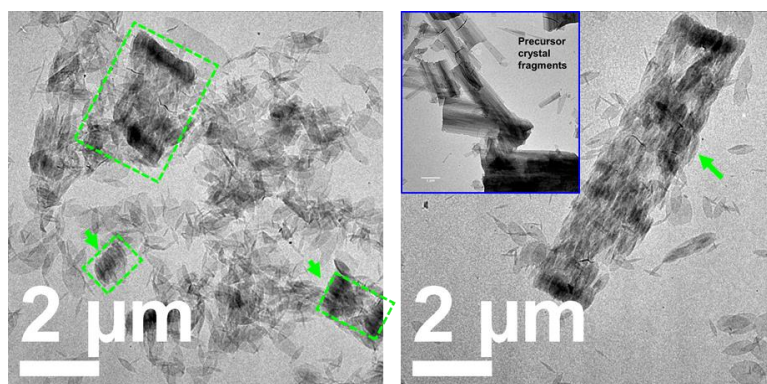


**Figure 3.15: PHBHx(3.9mol%) single crystals prepared using ultrasonification assisted self-seeding method. Green boxes and green arrows indicate self-assembled structures comprised of multiple individual self-seeded crystals. Insert is fragmented precursor crystals treated by ultrasonification.**

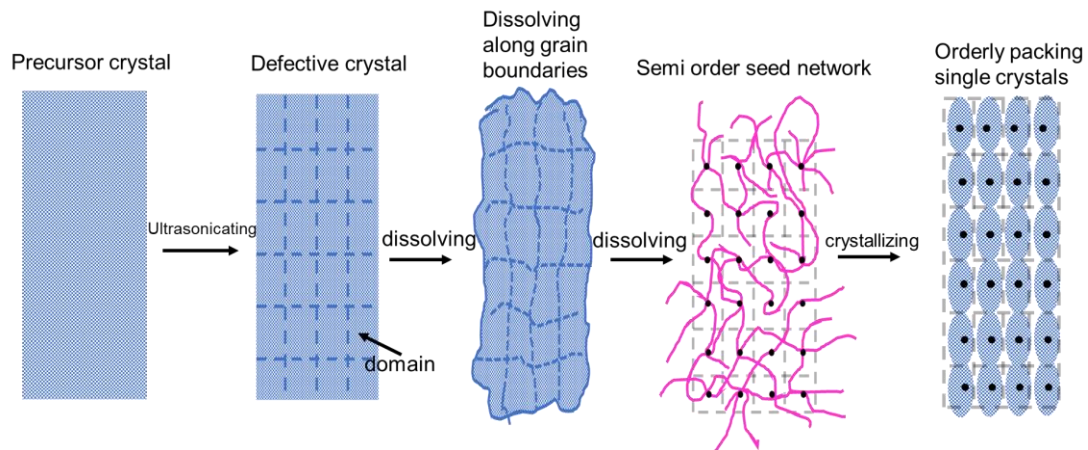


**Figure 3.16: A schematic illustrating the formation of self-assembled structure comprised of multiple individual self-seeded crystals.**

### 3.4 Gradual cooling method

The gradual cooling process is the simplest crystallization method and ironically, it was discovered last. It involves dissolving the polymer in EtOH at a specific  $T_d$ , followed by gradually cooling to a desired temperature. Hence, it is a non-isothermal crystallization process. PHBHx crystals (from spherulites to single crystals) can be prepared by this approach.

This method relies on the unique properties of EtOH. Though EtOH has long been used as a poor solvent, it was found EtOH alone can serve as a good solvent to dissolve PHBHx at elevated temperatures (above the normal boiling point of EtOH, or 78 °C) in a well-sealed vial. The specific  $T_d$  depends on 3HHx content and polymer concentration in solution.  $T_d$  for PHBHx(13mol%) can be as low as 90 °C, whereas  $T_d$  for PHBHx(3.9mol%) is above 110 °C. The transition for EtOH from a poor solvent to a good solvent occurs around 80 °C, which is near the disassociation temperature of H-bonds in EtOH. Once the polymer is dissolved at  $T_d$ , the solution is cooled down to room temperature at a selected cooling rate. The cooling rate is a critical parameter. In

order of the cooling rate from high to low, three cooling methods are typically used: 1) switching off heating element while leaving sample in the oil bath (thereafter called “naturally cooling in oil bath”), 2) rapidly transferring the sample to a ice water bath (thereafter called “cooling by ice water” ); and 3) rapidly putting the sample to into ambient air (thereafter called “cooling by air”). Cooling too fast leads to phase separation because the transition from poor to good solvent for EtOH is faster than the crystallization rate. Experimentally, this method is the simplest compared with the self-seeding method since it involves only two steps. However, the actual crystallization mechanism is complicated and not well understood since the crystallization process and solvent transition process occur simultaneously.

One tunable parameter is  $T_d$ . For example, PHBHx(13mol%) crystals were grown using a gradual cooling method. Figure 3.17 shows the resulting crystals appearing as spherulites and eventually as single crystals with decreasing  $T_d$ . For  $T_d = 105\text{ }^\circ\text{C}$ , hedrites were observed, which are typically viewed as premature spherulites. For  $T_d = 100\text{ }^\circ\text{C}$ , multi-layered lamellar crystals were observed. These structures are believed to be the even earlier development stage of spherulites.  $T_d = 90\text{ }^\circ\text{C}$  gives rise to single crystals. Being able to successfully grow single crystals for PHBHx(13mol%) (such a high comonomer content) without using a self-seeding method was a surprise .

$T_d=110^\circ\text{C}$

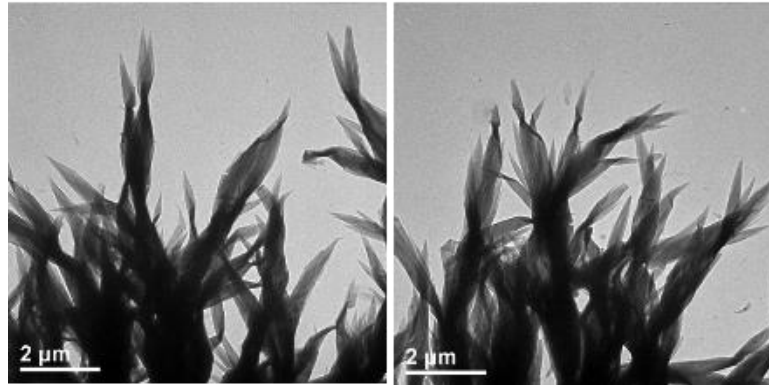


**Figure 3.17: PHBHx(13mol%) spherulites grown using a gradual cooling method with  $T_d = 110^\circ\text{C}$**

$T_d 105^\circ\text{C}$

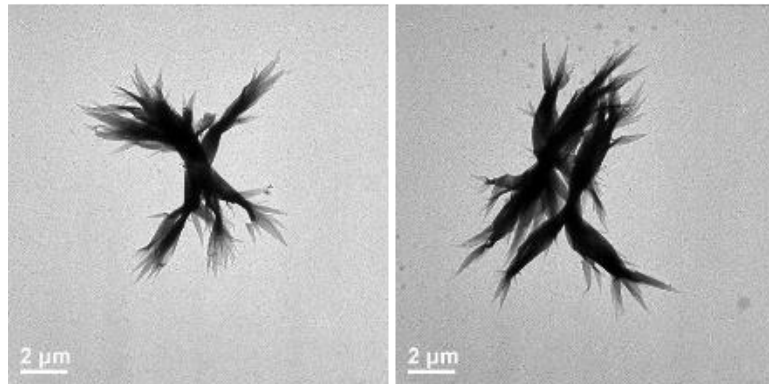


**Figure 3.18: PHBHx(13mol%) spherulites grown using a gradual cooling method with  $T_d = 105^\circ\text{C}$**

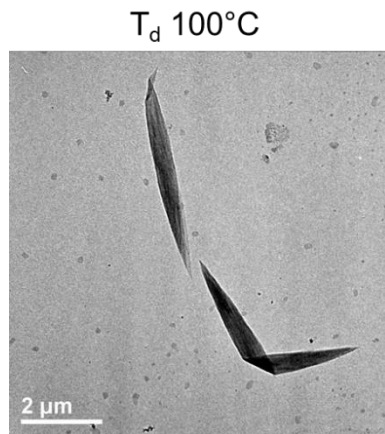


**Figure 3.19: PHBHx(13mol%) spherulites grown using a gradual cooling method with  $T_d = 100$  °C**

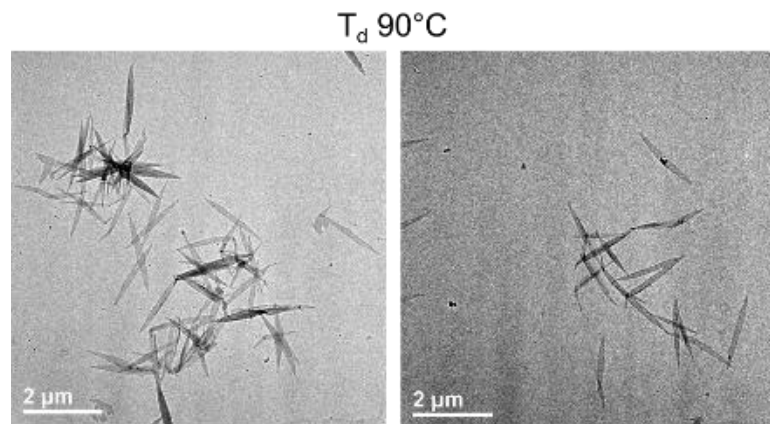


**Figure 3.20: PHBHx(13mol%) spherulites grown using a gradual cooling method with  $T_d = 90$  °C**

### 3.5 Comments on the three crystallization methods

The isothermal crystallization method is an excellent way to study temperature effects on crystal habits since crystallization can be strictly controlled. It is the favored method for a crystallization mechanism study. However, this technique typically gives giant lamellar crystal aggregates or spherulites. Lamellar crystals can be found near

the spherulite edge. The key for successful application of this method is choosing the right ratio of chloroform and ethanol and preventing crystallization from occurring during the cooling step.

The self-seeding technique can result in beautiful single crystals. It is favored if the goal is to control crystal uniformity. However, this technique involves multiple steps, which are typically time consuming. Once seeds are formed, crystallization typically occurs during the cooling process. The knowledge gained from conducting self-seeding experiments for polymer crystals may provide information on how to grow nano crystals of other materials since the self-seeding technique has a much broader application in materials science.

The gradual cooling technique is a useful, simple method for growing single crystals, but its mechanism is less well understood. However, identifying a working solvent is critical and is not favored for mechanistic crystallization studies.

## Chapter 4

### CRYSTALLIZATION MECHANISM FOR PHBHx(3.9mol%) SINGLE CRYSTALS UNDER ISOTHERMAL GROWTH

While solution grown, single crystals of the homopolymer PHB have already been studied, single crystals of PHBHx have not. In addition, the effect of temperature on crystallization of either PHB or PHBHx has not been investigated. PHBHx (3.9mol%) single crystals were prepared by isothermal growth at temperatures ranging from -20 to 80 °C and the crystal structure, growth habits, and properties have been studied.

Several technical challenges present themselves when growing single crystals of PHBHx. First, the PHBHx sample used in this study has an ultrahigh  $M_w$  of 800,000g/mol. Second, 3.9mol% 3HHx content is a relatively high defect level. Third, 3HHx is statistically distributed along the backbone. All these factors will hinder the growth of single crystals of PHBHx.

#### 4.1 Preparation conditions

A chloroform/ethanol mixture was used as the solvent. From preliminary results, a phase diagram was created as shown in Figure 4.1. In the Figure, the horizontal axis is the molar fraction of good solvent (chloroform) in the mixture. The experimentally determined red (upper limit  $T_c$ ) and blue (cloud point) profiles, approximately divide the phase diagram into three regions. In the right upper region, i.e., above the upper limit  $T_c$  line, due to a higher temperature and higher chloroform content, the polymer was not observed to crystallize but remained in solution. In the

left bottom region, i.e., below the cloud point line, due to a low temperature and higher ethanol content, the polymer chains are isolated in solution, collapsing into amorphous globules via phase separation. The region between red and blue lines is the crystallization area where single crystals can be grown.

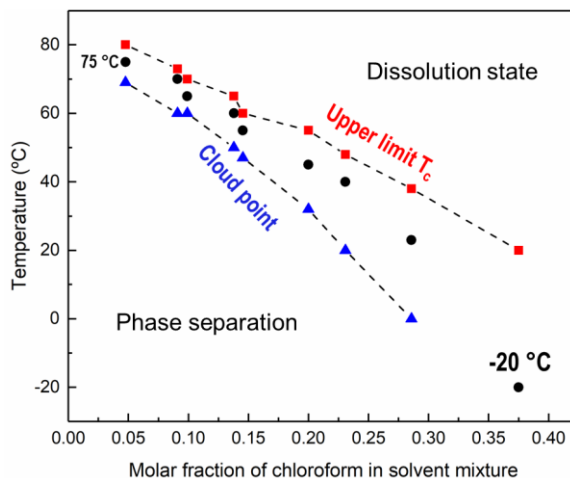


**Figure 4.1: A phase diagram of PHBHx(3.9mol%) in the solvent mixture of chloroform and ethanol.**

Crystals were grown at  $T_c$  (-20, 20, 40, 45, 50, 55, 60, 65, 70, and 75 °C), represented by the black data points in the above figure. Solvent conditions corresponding to each  $T_c$  are shown in Table 4.1.

**Table 4.1: Crystallization conditions**

Crystallization temperature/°C	-20	20	40	55	60	65	75
Molar fraction of CHCl <sub>3</sub> in solvent mixture/mol%	38.00%	29.00%	23.00%	15.00%	14.00%	10.00%	5.00%

## 4.2 Crystal morphology and crystal polymorph as a function of $T_c$

A Tecnai G<sup>2</sup> 12 TEM was used operating at 120 kV. During sample preparation, crystal suspension droplets were deposited onto an amorphous carbon coated copper grid. After solvent evaporation, the sample grid was loaded into the TEM.

Figure 4.2 shows TEM results of single crystals of PHBHx grown at -20 °C. The crystals show irregular growth behavior, but a needle-like growth habit can be identified. A twisting hierarchical structure can also be identified. The Electron Diffraction Pattern (EDP) from the yellow-boxed area shows rings with two distinct radii. The inner and outer rings can be indexed with (020), and (110) atomic planes of the alpha crystal form of the homopolymer PHB, respectively. The crystals are not single crystals judging from the morphology and diffraction pattern. PHBHx has a glass transition temperature ( $T_g$ ) near 0 °C. The successful crystallization of PHBHx at -20 °C is presumably attributed to an enhanced chain mobility in dilute solution. However, the degree of chain mobility is indeed decreased, which can be seen from the less well-defined crystal geometry. The significance of this low  $T_c$  study is that the PHBHx crystal still adopts the alpha crystalline form of PHB. This is the first time crystallization of PHBHx has been observed at such a low temperature and the result indicates that the alpha crystal structure is still thermodynamically stable at such a low temperature.

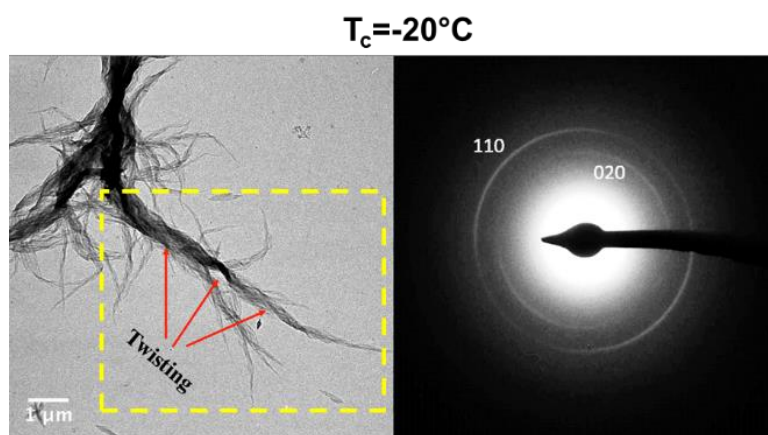


**Figure 4.2: Morphology and diffraction pattern (from yellow boxed area) of PHBHx(3.9mol%) crystals grown at  $-20^\circ\text{C}$ .**

Figure 4.3 shows the morphology and EDP for single crystals grown at  $20^\circ\text{C}$ . A very sharp, needle-shaped crystal structure can be found on the edges of the crystal aggregates. Selected area EDP was conducted on the red highlighted crystal. An identifiable, yet blurry single crystal-like diffraction pattern can be seen. The diffraction pattern can still be indexed with (020) and (110) atomic planes of the alpha crystals of the homopolymer PHB. Experimentally, obtaining a diffraction pattern for this crystal was challenging because of two factors. First, the diffraction intensity of this crystal is intrinsically low, presumably due to limited crystal growth along the b-direction. Second, increasing beam dose to obtain a brighter diffraction pattern failed due to increased sample damage. Nevertheless, optimizing dose rate and applying low-dose function enabled successful recording of the diffraction pattern. The significance of this study is, first, at a low  $T_c$ , the highly defective PHBHx can crystallize into a well-defined single crystal, suggesting superior crystallization ability; second, this is the first observation of PHB or PHBHx crystals with such a high anisotropic

geometry; third, the diffraction pattern indicates that the long-axis of the crystal is along the a-axis in the unit cell of the alpha form.

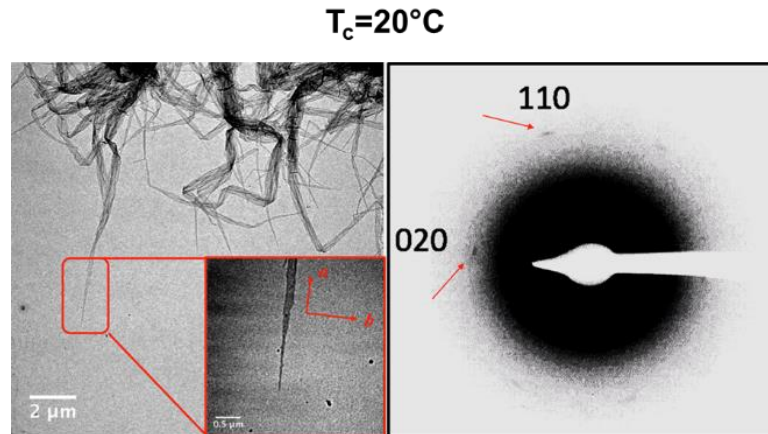


**Figure 4.3: Morphology and diffraction pattern (from red highlighted area) of PHBHx(3.9mol%) crystals grown at 20 °C.**

Figures 4.4 to 4.8 show the morphologies and EDPs of single crystals grown at 40, 55, 60, 65, and 75 °C, respectively. All the crystals still have a needle-shaped growth pattern and adopt the alpha crystalline form of PHB. In addition, as  $T_c$  increases, the single crystals have a less anisotropic geometry and the diffraction intensity increases. The increased diffraction intensity is believed to arise from an enhanced growth along the b direction at higher  $T_c$ .

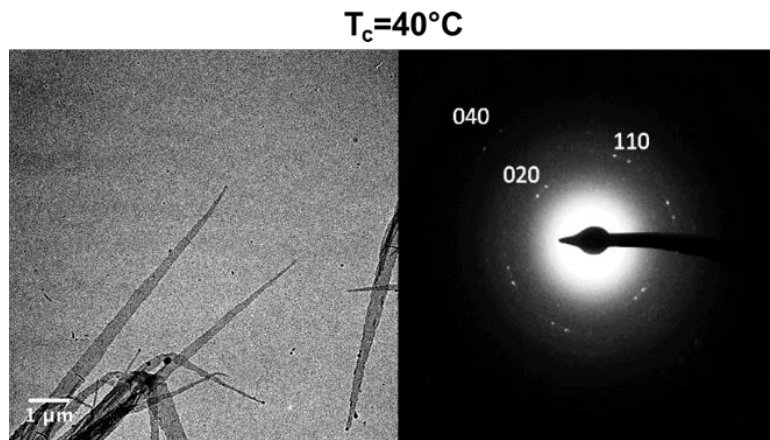


**Figure 4.4: Morphology and diffraction pattern of PHBHx(3.9mol%) crystals grown at 40 °C.**

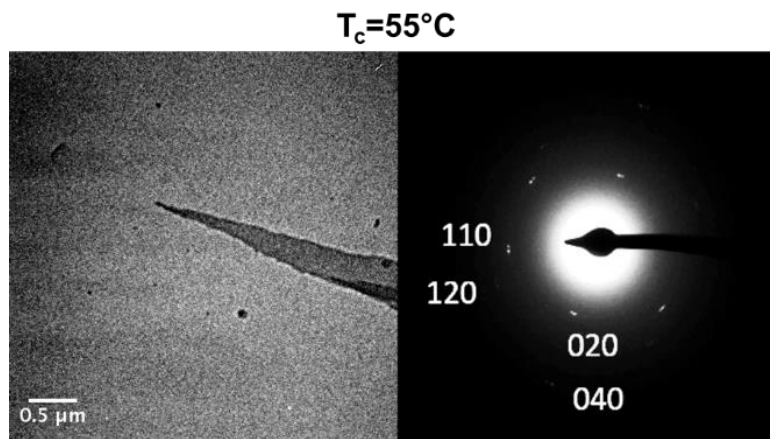


**Figure 4.5: Morphology and diffraction pattern of PHBHx(3.9mol%) crystals grown at 55 °C**

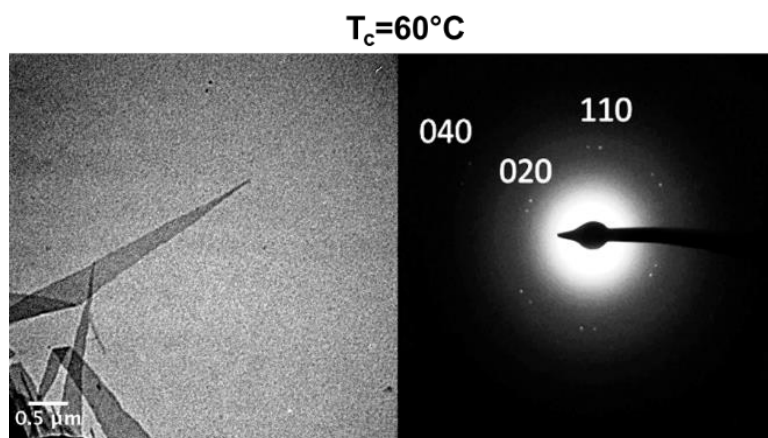


**Figure 4.6: Morphology and diffraction pattern of PHBHx(3.9mol%) crystals grown at 60 °C**

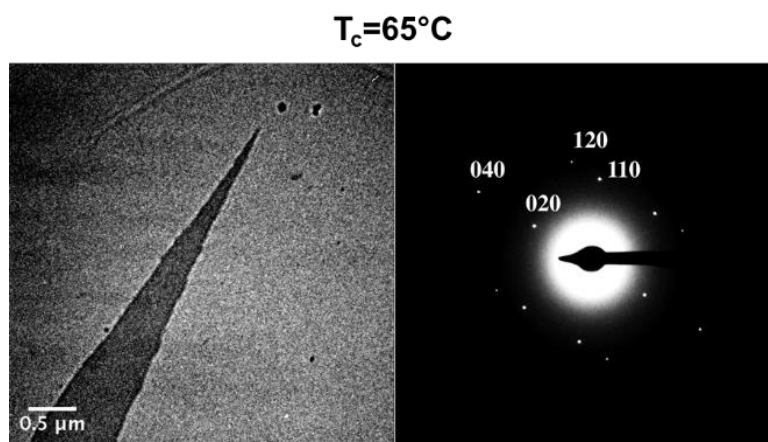


**Figure 4.7: Morphology and diffraction pattern of PHBHx(3.9mol%) crystals grown at 65 °C**

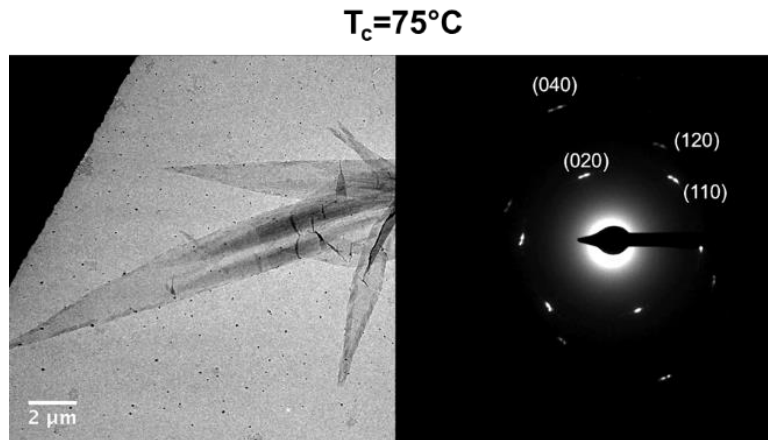


**Figure 4.8: Morphology and diffraction pattern of PHBHx(3.9mol%) crystals grown at 75 °C**

The needle-shaped growth pattern originates from the growth rate difference of the crystal along the a and b directions, which can be experimentally determined by measuring the apex angle of the needle-shaped crystals. As shown in Figure 4.9, the growth rate ratio can be calculated as  $r = x/y = 1/(\tan(\Theta/2))$ . The unit cell packing rate ratio  $r_u = r^*(b/a)$  reflects the crystal growth rate difference along the a and b directions, since the unit cell is the basic building unit during crystal growth. In order to have statistical significance, 36 crystals were randomly selected and their apex angles  $\Theta$  were measured for each  $T_c$ . The statistical histograms are shown in Figure 4.10. Figure 4.11 shows the plot of apex angle, growth rate ratio, and unit cell packing rate ratio along the a- and b- directions of the single crystal as a function of  $T_c$ . The result shows that at  $T_c$  20 °C, the unit cell is adding to the growth front 55 times faster along the a-axis than that along b-axis. At 70 °C, the ratio decreases to 22 times.

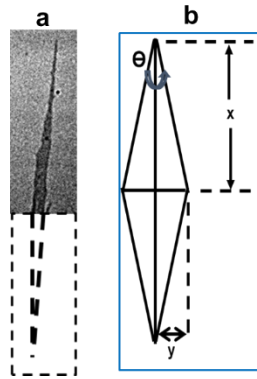


**Figure 4.9: A schematic to illustrate the needle-shaped crystal, apex angle  $\Theta$ , and growth dimension  $x$  and  $y$  along two directions.**

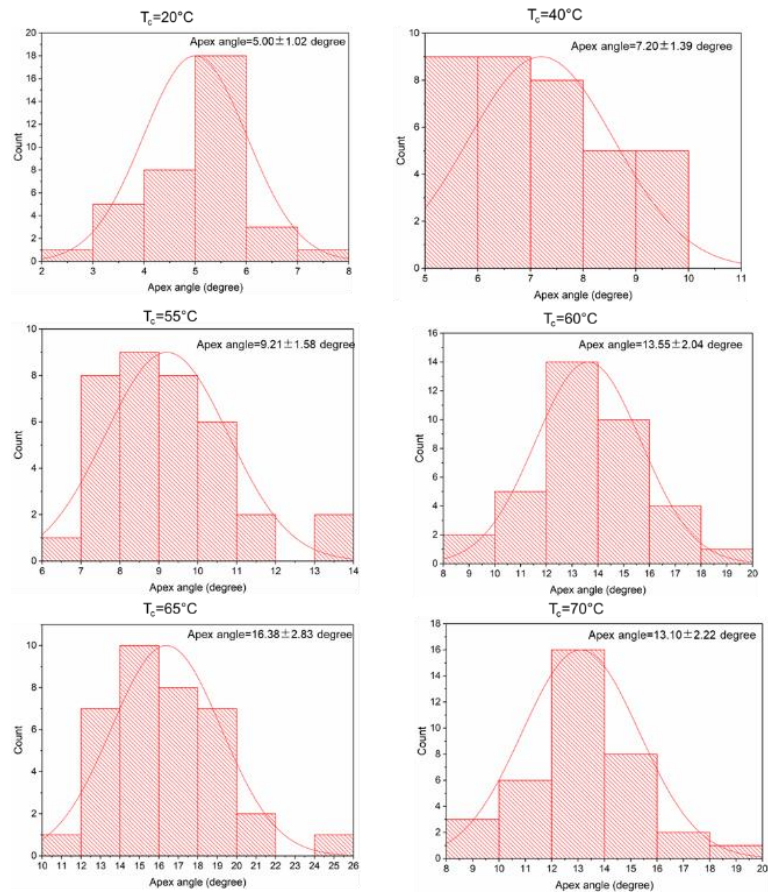


**Figure 4.10: Histograms of measured apex angle of crystals at each  $T_c$ .**

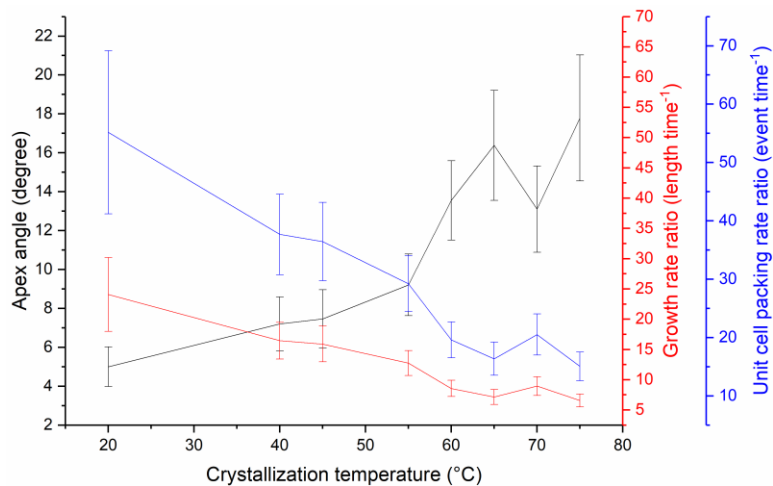


**Figure 4.11: The plot of apex angle, growth rate ratio, and unit cell packing rate ratio along the a- and b- axes as a function of  $T_c$ .**

### 4.3 Variations of lattice parameters, a and b, as a function of $T_c$

The lattice parameter, a, for crystals grown at  $T_c$  from -20 to 75 °C, have values of  $0.574 \text{ nm} \pm 0.003 \text{ nm}$ , indicating no lattice expansion along the a direction. This finding suggests it is very difficult to disrupt the crystal structure along the a direction. However, the b parameter has values of  $1.324 \text{ nm} \pm 0.003 \text{ nm}$  for all the  $T_c$  except -20 °C, and expands to  $1.330 \text{ nm} \pm 0.003$  at -20 °C. Expansion along the b direction suggests the comonomer 3HHx may be included into the lattice along the b direction. This phenomenon is possibly due to a low temperature induced kinetic effect. In summary, the 3HHx was found to be excluded from the crystal lattice, and is presumably located in the fold surface. A schematic is shown in Figure 4.12.

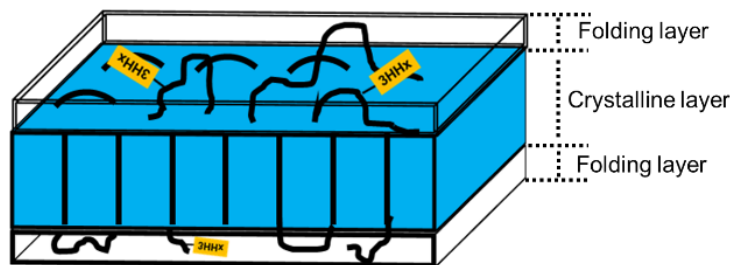


**Figure 4.12: A schematic to illustrate a lamella crystal model with 3HHx excluded from the crystalline layer and located on the folding layer.**

#### 4.4 Lamellar thickness evaluation

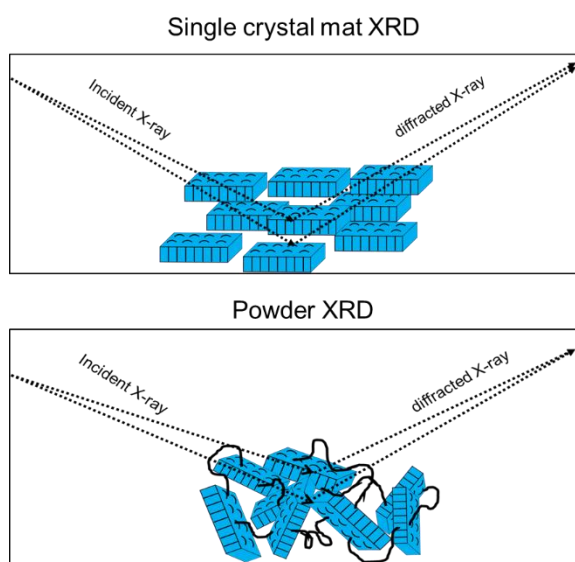
Lamellar thickness is one of the characteristic parameters for polymer single crystals. As shown in Figure 4.12, one lamellar crystal consists of a crystalline layer and two fold layers. The thickness of the crystalline layer reflects the energetic potential a polymer has to crystallize. A thinner crystalline layer implies the crystalline state has a lower Gibbs free energy per volume, leading to a higher crystallization potential.

Single crystals were collected by reduced pressure filtration, resulting in a single crystal mat with the crystals flat-on oriented. 1-D X-ray Diffraction (XRD) in the reflection mode was then used to collect a diffraction pattern. Figure 4.13 shows a schematic to compare single crystal mats and powder XRD.

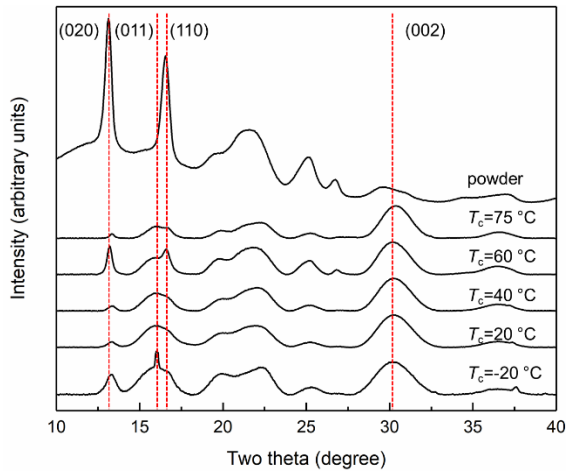
From the XRD data in Figure 4.14, diffraction patterns for all the single crystals were similar to each other but differ dramatically from that of powder XRD. The high intensity of the (020) peak suggests the single crystals are preferentially flat-on oriented. At -20 °C, the (011) peak is high possibly due to lamellae twisting observed under TEM examination for the same sample.

A well resolved (002) peak for the single crystal samples enables evaluation of crystalline layer thickness by using the Scherrer equation. Crystallite size along the c

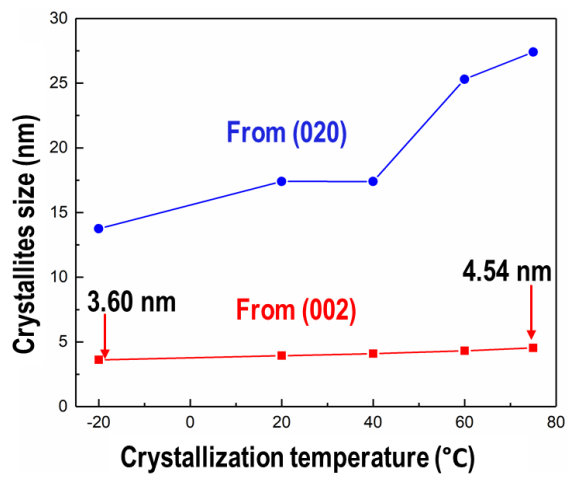
direction (crystalline layer thickness) and b direction plotted against  $T_c$  are shown in Figure 4.15. Crystalline layer thicknesses for all the  $T_c$  are very thin, reaching 3.60 nm at  $T_c$  -20 °C, corresponding to less than 6 consecutive 3HB repeating units in the crystal. Such a small amount of required 3HB units may be one of reasons why incorporating low concentration of 3HHx comonomer is not enough to stop the 3HB from crystallizing. In addition, the crystalline layer thickness is slightly dependent on  $T_c$ , with a higher  $T_c$  giving a thicker crystalline layer. Crystallite size along the b axis increases dramatically, suggesting the crystals tend to have an enhanced growth along the b axis with increased  $T_c$ . This observation is consistent with TEM result, where the anisotropic growth habit is attenuated with increased  $T_c$ .



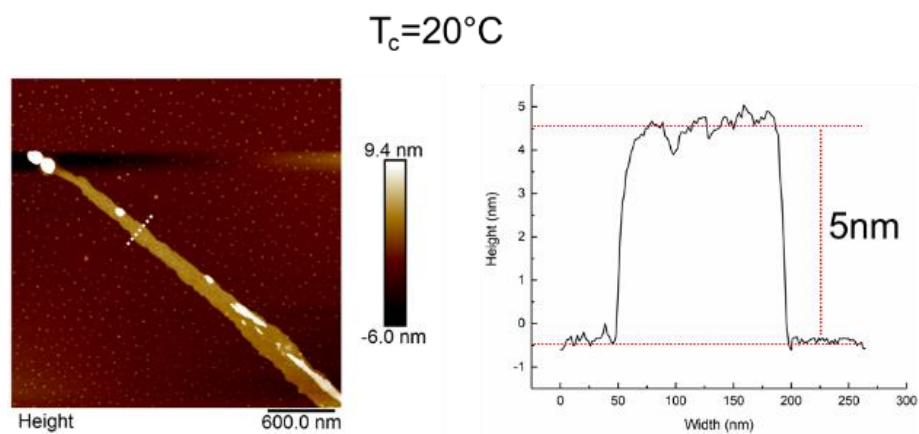
**Figure 4.13: A schematic to compare single crystal mat and powder XRD.**



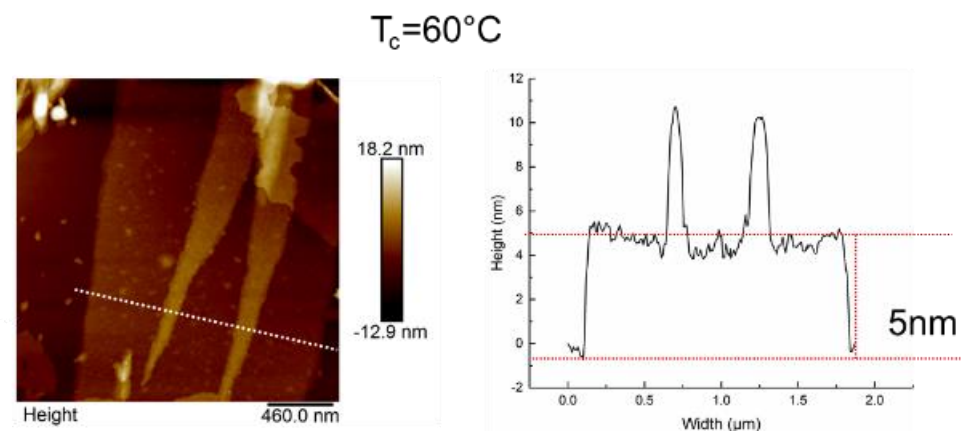
**Figure 4.14: XRD data for PHBHx(3.9mol%) single crystal mats at different  $T_c$  and powder diffraction data.**



**Figure 4.15: The plots of crystallites size along the b and c axis as a function of  $T_c$ .**



**Figure 4.16: AFM height image of PHBHx(3.9mol%) single crystals at 20 °C**



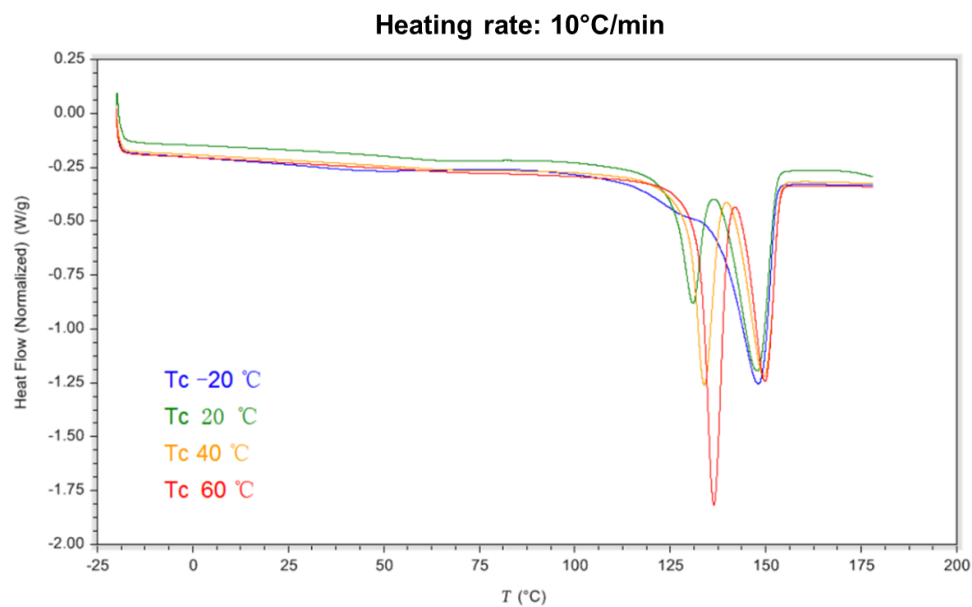
**Figure 4.17: AFM height image of PHBHx(3.9mol%) single crystals at 60 °C**

Figure 4.16 and 4.17 show AFM height images of single crystals grown at a  $T_c$  of 20 °C and 60 °C. AFM measurements yield the overall lamellar thickness (refer to Figure 4.12). Both crystals have a thickness of approximately 5 nm, suggesting the overall thickness is not changing with  $T_c$ . Knowing that the crystalline thickness

slightly increases from 20 to 60 °C, we can conclude that the folding layer thickness is decreasing with increased  $T_c$ .

#### **4.5 DSC studies of PHBHx(3.9mol%) grown at different $T_c$**

DSC studies were performed on single crystals grown at -20, 20, 40, and 60 °C with a heating rate of 10 °C/min. In Figure 4.18, all traces show two exothermic (melting) peaks. The higher temperature peaks (2<sup>nd</sup> peak) for all the samples appear at nearly the same temperature, suggesting this peak is not dependent on  $T_c$ . This 2<sup>nd</sup> peak may result from a recrystallization process or a lamellar thickening process. Variable temperature small angle X-ray scattering (SAXS) can be conducted to confirm this hypothesis. Real-time SAXS studies on the annealing behavior of PHB single crystals have been performed by Tomoharu Sawayanagi et al.,<sup>15</sup> indicating the 2<sup>nd</sup> peak arises from a thickened crystal. The temperature of the 1<sup>st</sup> peak increases with increased  $T_c$ , suggesting a higher  $T_c$  results in a thicker lamella, which is consistent with crystalline layer thickness variation derived from XRD measurement (see Figure 4.15).



**Figure 4.18: DSC heating curves for PHBHx(3.9mol%) single crystals grown at -20, 20, 40, and 60 °C.**

We selected crystals grown at  $T_c$  60 °C to conduct a DSC experiment as a function of heating rate, as shown in Figure 4.19. The inset is from a trace with a 0.5 °C/min heating rate. The data shows that the 1<sup>st</sup> peak doesn't change its temperature with heating rate. The peak area (enthalpy) ratio of the 2<sup>nd</sup> to the 1<sup>st</sup> peak decreases with increased heating rate, suggesting a slower heating rate facilitates the development of the 2<sup>nd</sup> peak. A slower heating rate also gives rise to a higher melting temperature of the 2<sup>nd</sup> peak. Thus, we deduce that the 2<sup>nd</sup> peak is from the melting of thickened or recrystallized crystals, since either the thickening or recrystallizing process is time dependent. A slower heating rate gives rise to more (larger peak area for the 2<sup>nd</sup> peak) and thicker (higher melting temperature for the 2<sup>nd</sup> peak) crystals.

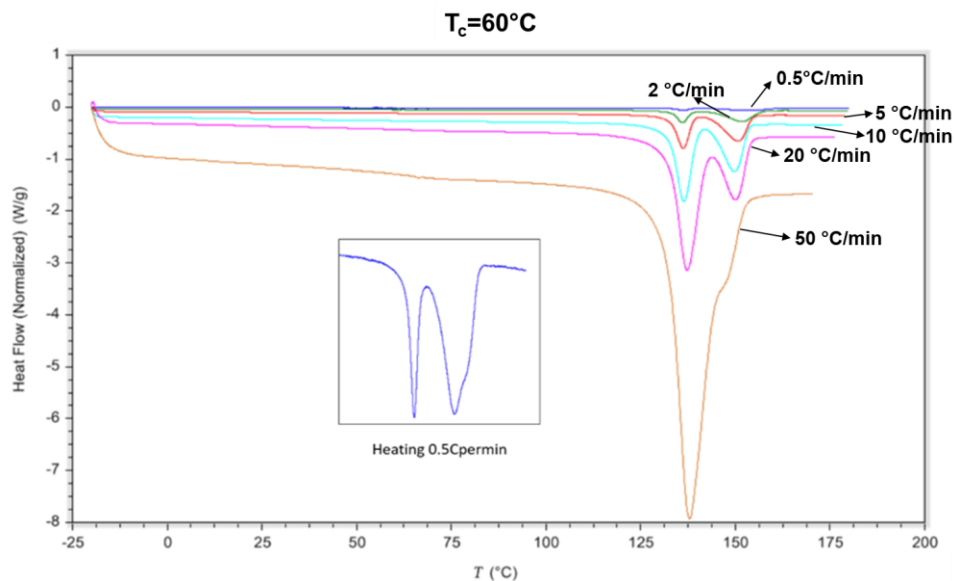


**Figure 4.19: DSC heating traces for PHBHx(3.9mol%) single crystals grown at 60 °C as a function of heating rate.**

#### 4.6 FTIR study of PHBHx(3.9mol%) single crystals

Infrared spectroscopy is a powerful tool used to study molecular structure and intermolecular interactions for polymers in the solid-state. FTIR ATR measurements were performed on single crystals grown at -20, 20, 40, and 60 °C. The carbonyl stretching region and CH stretching region are shown in Figure 4.20. The raw spectra were corrected using the “advanced ATR correction” function in the Essential FTIR software. In the carbonyl region, all samples show a 1722  $\text{cm}^{-1}$  peak and a 1743  $\text{cm}^{-1}$  shoulder. The 1722  $\text{cm}^{-1}$  band is indicative of the formation of alpha crystals and 1743  $\text{cm}^{-1}$  band is attributed to amorphous material. The existence of a significant amount of amorphous material confirms that PHBHx single crystals have substantial amorphous component. In the CH stretching region, a blue-shifted CH stretching peak

at  $3009\text{ cm}^{-1}$  is interesting. Typically, a CH stretching frequency is located below  $3000\text{ cm}^{-1}$ . The  $3009\text{ cm}^{-1}$  peak was first found in melt crystallized PHB films and since then has been attributed to a special H-bonding interaction formed between the H atom of  $-\text{CH}_3$  group from one crystalline stem and the O atom of  $-\text{C}=\text{O}$  from an adjacent crystalline stem. Given the relatively low bonding energy (below  $-4\text{ kcal/mol}$ ) compared to the conventional H-bonding [strong ( $4\text{-}15\text{ kcal/mol}$ ) and very strong ( $15\text{-}40\text{ kcal/mol}$ ) as categorized in Gautam and Thomas's book<sup>16</sup>], this special interaction has been described as a weak H-bonding interaction. Though the debate is ongoing over whether this interaction is a real H-bond, for the sake of simplicity, we will use the term “weak H-bonding” to describe this unusual interaction. This is the first time that this weak H-bonding has been observed in a PHBHx single crystal.

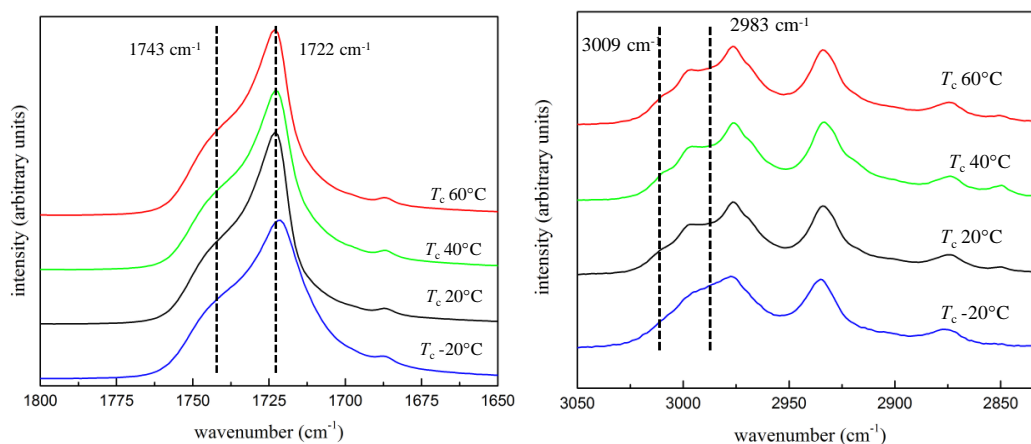


**Figure 4.20: FTIR spectra of PHBHx(3.9mol%) single crystals at different  $T_c$ . The carbonyl stretching region is on the left and the CH stretching region is on the right.**

## 4.7 Crystal structure analysis

Using lattice parameters and atomic coordinates determined elsewhere,<sup>17</sup> we constructed the unit cell and a schematic of the crystal structure is shown in Figure 4.21. The weak H-bonds are represented by green and blue dashes. Viewing the crystal along the c-axis (Figure 4.21 left), we can find that inter-stem interactions along the a-axis have the H-bonds involved whereas inter-stem interactions along the b-axis have only Van der Waals interactions. This direction dependent interaction is believed to be the underlying reason responsible for the anisotropic growth habit of the PHBHx single crystals. In addition, according to the Boltzmann distribution, at a certain crystallization temperature  $T_c$ , the possibility of forming one mole stems packing along the a-axis is proportional to  $\text{Exp}[-\Delta E_a/k_b T]$ , and the counterpart along the b-axis is proportional to  $\text{Exp}[-\Delta E_b/k_b T]$ . Here  $k_b$  is Boltzmann constant,  $\Delta E_a$  and  $\Delta E_b$  are the energy drop from a random coil state to a  $2_1$  helix added to the growth front along the a and b direction, respectively. Thus, the ratio of the two possibilities is proportional to  $\text{Exp}[-\Delta E/k_b T]$ , where  $\Delta E = \Delta E_a - \Delta E_b$ . The H-bonding interaction is dominantly along the a direction, leading to  $\Delta E_a > \Delta E_b$ . Therefore, as  $T_c$  decreases, the ratio increases exponentially, giving rise to a highly anisotropic crystal growth habit at a low  $T_c$  (sharp needle-shaped crystal at 20 °C).

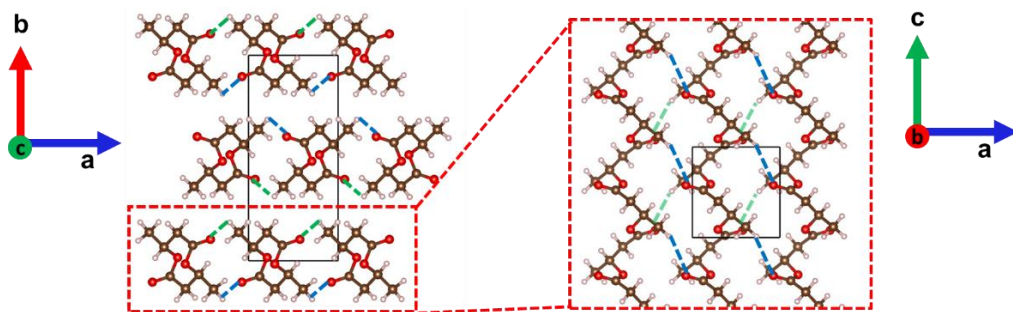


**Figure 4.21: Schematic of PHB alpha crystalline structure viewed along c (left) and b (right) directions.**

Viewing the crystal along the b-axis (Figure 4.21 right), the hydrogen bonded H atom and the hydrogen bonded O atom in the same 3HB monomer have very close z coordinates. This alignment results in H-bonds packing along the c-axis in a high-density fashion. Therefore, it is proposed that although the H-bonding energy for one individual H-bond is relatively low, when all the H-bonds are packed in the crystal structure in a compact way. It should result in a cooperative H-bonding network, leading to a significant Gibbs energy drop during the alpha crystallization from the melt state. The network also does not allow 3HHx to be accommodated into the crystal structure.

Though the  $3009\text{ cm}^{-1}$  band in the FTIR spectrum is typically taken as the evidence for H-bonding formation, it is still difficult to explain why such a H-bond can cause a blue shift. Therefore, the most important scientific impact of the current single crystal work is that we were able to provide strong morphological evidence to demonstrate the possible presence of H-bonding along the a direction, since otherwise, we should not have observed such a anisotropic growth habit of the single crystal.

#### 4.8 Critical dose measurement of PHBHx single crystals

Due to electron beam sensitivity of polymer single crystals, it is typically recommended to determine the critical dose value for the crystals, which helps choosing the right dose rate during TEM imaging experiment. Critical dose can also be used as an indicator for electron beam resistance of the crystals, reflecting in some degree the stability of the crystals. Figure 4.22 shows an example of how morphology and diffraction pattern changes for PHBHx(3.9mol%) single crystals as a function of electron dose.

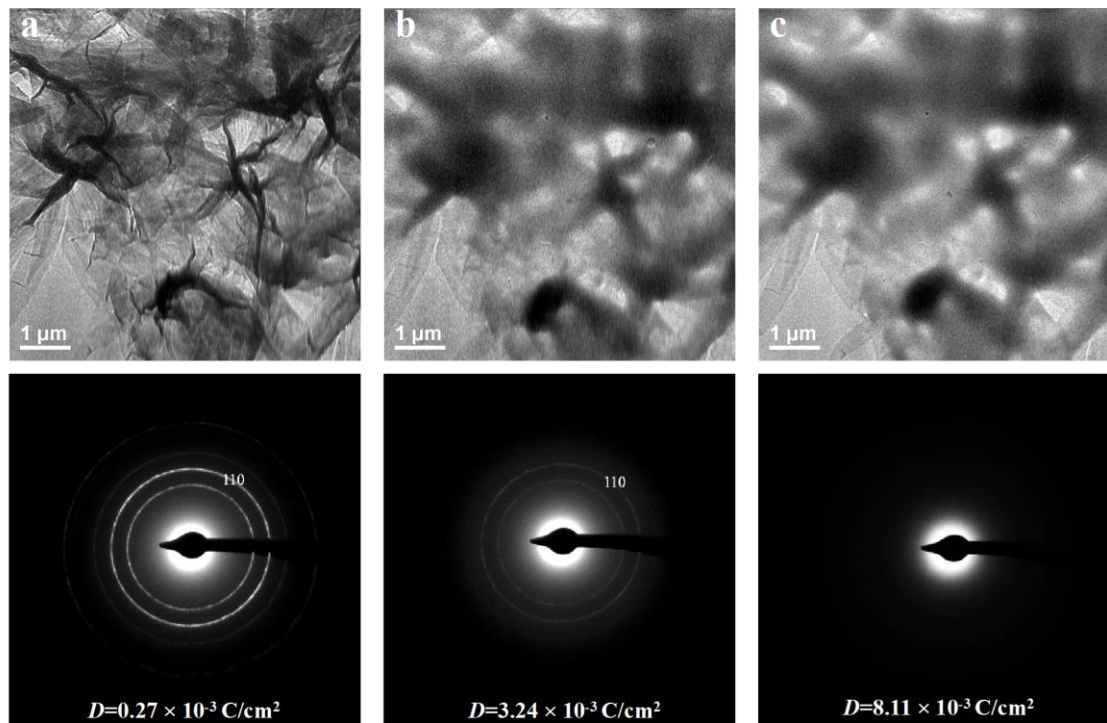


**Figure 4.22: Morphology and diffraction pattern changes of PHBHx(3.9mol%) single crystals as a function of electron dose.**

The equation

$$I(D) = I_0 \exp\left(-\frac{D}{D^*}\right) + I_R$$

is typically used to derive critical dose value. It is an empirical equation and so far, the nature of the damage mechanism is not quite clear. The debate over the beam damage process is whether it is melting or degradation driven. In the equation,  $D^*$  is the to-be-determined critical dose in units of  $C/cm^2$ .  $I_0$  is the initial diffraction intensity.  $I_R$  is the residual intensity including background and scattering from the damaged crystals.  $D$  is electron dose, which is equal to dose rate multiplied by exposure time, so the dose is proportional to exposure time. In our case, a constant dose rate of  $3.86 \times 10^{-5} C/(cm^2 \text{ sec})$  was used, Such a dose rate allowed us to record about 30 diffraction patterns every 7 sec with a 0.1 sec exposure time for each one. Taking the logarithm to have  $\text{Ln}[I-I_R] = -D/D^* + \text{Ln}I_0$ , then  $D^*$  can be derived from the slope of the linear plot of  $\text{Ln}[I-I_R]$  against  $D$ .

The software Image J was used for data processing. The first recorded 20 diffraction patterns were used to make the plot. As shown in Figure 4.23, a radial line was drawn on a diffraction pattern to obtain 1-D diffraction profile (Figure 4.24). The “*Macros*” plugin in ImageJ was used to ensure the crossed lines drawn for every diffraction pattern from the same crystal are along the same angle and with the same origin. The integrated peak area of (110) was used for  $I(D)$ . The logarithm plots of integrated area of (110) peak against electron dose for different  $T_c$  were displayed in Figure 4.25.

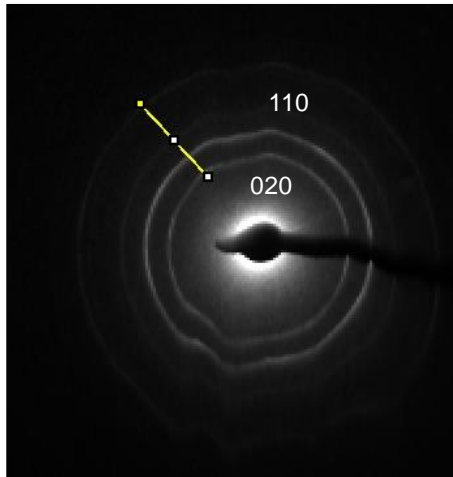


**Figure 4.23: Representative radial cross line drawn on raw diffraction pattern.**

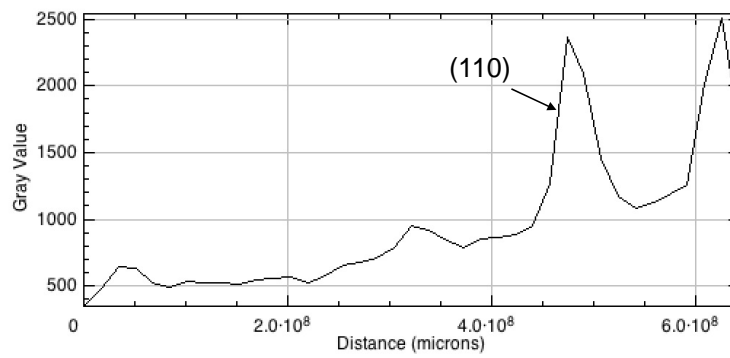


**Figure 4.24: 1-D profile from the cross line draw in Figure 3.23.**

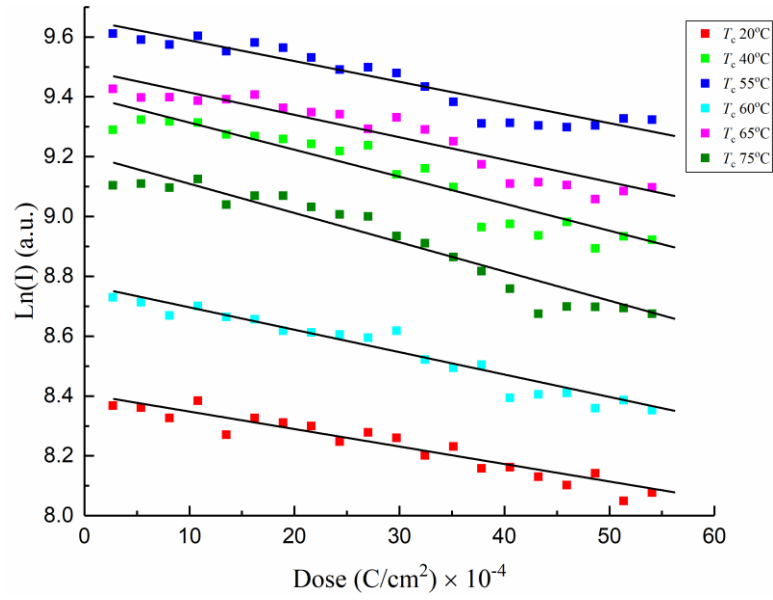


**Figure 4.25: Logarithm plots of (110) diffraction peak intensity as a function of electron dose for PHBHx(3.9mol%) single crystals grown at different  $T_c$ .**

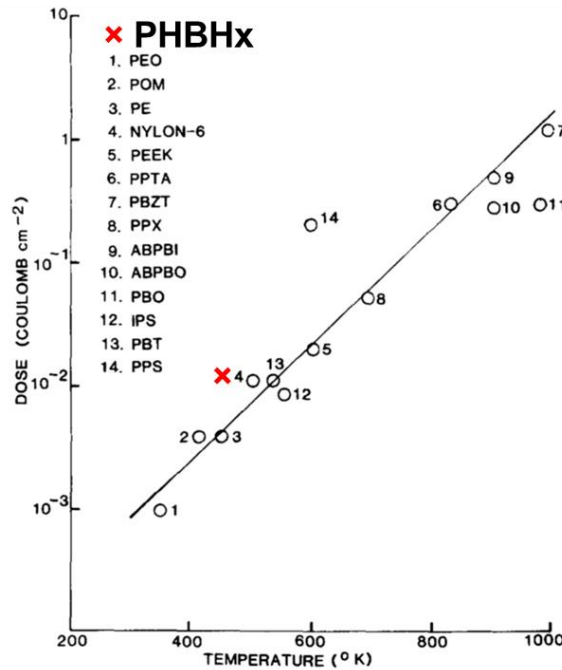


**Figure 4.26: Plot of critical dose vs melting temperatures for different polymers.<sup>18</sup> The red cross represents data point for PHBHx(3.9mol%).**

We found all the lines have similar slopes, suggesting similar  $D^*$  values for all  $T_c$ . This observation is reasonable since crystals grown at all  $T_c$  have the alpha crystal form. The actual values are around  $0.01C/cm^2$ . Comparing this value to other polymers' (Figure 4.26), we see PHBHx has a similar  $D^*$  as Nylon-6, higher than that of PE single crystals at similar operation voltages (0.0043 at 100 kV and 0.012 at 125 kV). This result reflects the relatively high stability of PHBHx crystal due most likely to the cooperative H-bonding network.

## Chapter 5

### EFFECT OF 3HHX ON THE MORPHOLOGY OF SOLUTION GROWN PHBHx CRYSTALS

In this chapter, detailed crystallization conditions for each sample are listed in the caption of corresponding Figures.

#### 5.1 Effect of 3HHx content on single crystal morphology

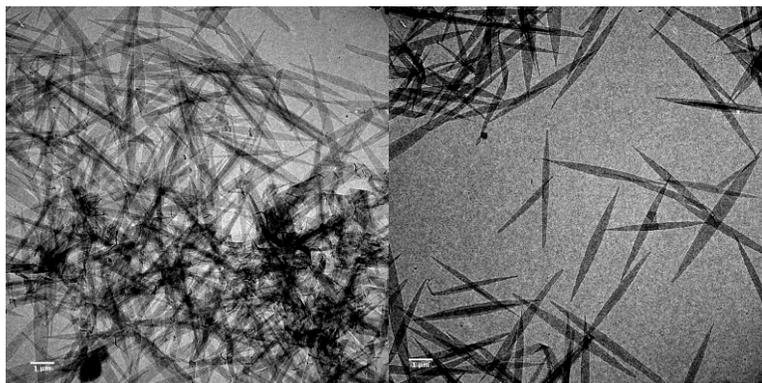
Using the self-seeding method, well isolated and well-defined single crystals of PHBHx(3.9mol%), PHBHx(7.6mol%), to PHBHx(13mol%) were grown. Figure 5.1 shows well isolated PHBHx(3.9mol%) single crystals while Figure 5.2 shows an individual PHBHx(3.9mol%) single crystal with its high-quality diffraction pattern. Such a high-quality crystal typically can only be achieved using the self-seeding technique.

Figure 5.3 shows self-seeded PHBHx(7.6mol%) single crystals and two types of single crystals were found. Type A single crystals have a round end whereas Type B crystals has a sharp needle-shaped end. Type A crystals still adopt the alpha crystalline form of PHB as shown in the EDP in Figure 5.4. Type A crystals were only found for PHBHx(7.6mol%) and the growth mechanism for this type of crystal is not well understood.

Figure 5.5 shows self-seeded PHBHx(13mol%) single crystals while Figure 5.6 shows one individual PHBHx(13mol%) crystal and its EDP. Though the diffraction intensity is much weaker, it can still be indexed using the alpha crystalline

form of PHB. Since PHBHx(13mol%) can form a well-defined single crystal, it is not surprising that PHBHx(3.9mol%) can also do so.

In summary, all PHBHx crystals adopt the alpha crystalline form of the homopolymer PHB, suggesting that the underlying driving force is governed by crystallization of 3HB monomer. The 3HHx comonomer is excluded from the lattice and exists on the fold surface. The effect of 3HHx has a very minimal influence on the morphology of single crystals prepared by the self-seeding method.



**Figure 5.1: PHBHx(3.9mol%) single crystals. Crystallization method: self-seeding. Crystallization conditions: concentration = 0.027wt%, precursor crystallization (pure EtOH,  $T_d = 110\text{ }^\circ\text{C}$ , gradual cooling in an oil bath), seeding process ( $T_i = 70\text{ }^\circ\text{C}$ , heating rate =  $30\text{ }^\circ\text{C/hr}$ ,  $T_s = 100\text{ }^\circ\text{C}$ , gradual cooling in an oil bath).**

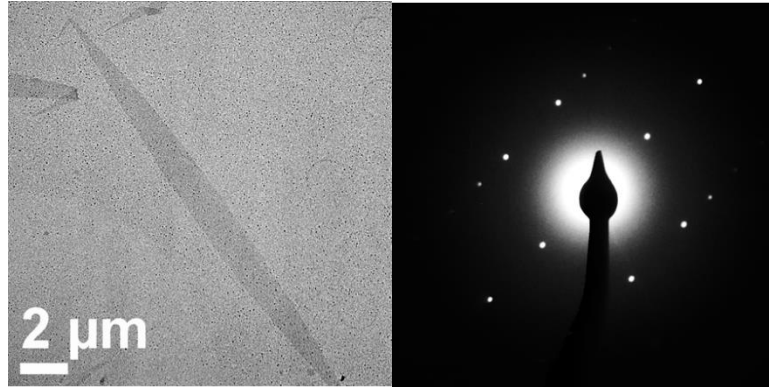


**Figure 5.2: An individual PHBHx(3.9mol%) single crystal grown by the self-seeding method and its EDP.**

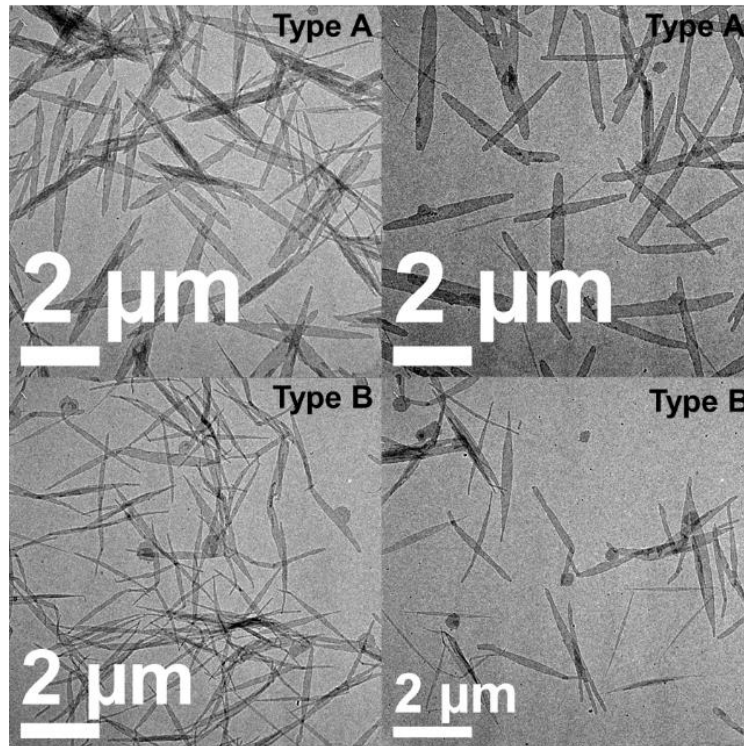


**Figure 5.3: PHBHx(7.6mol%) single crystals. Crystallization method: self-seeding. Crystallization conditions: concentration = 0.01wt%, precursor crystallization (pure EtOH,  $T_d = 110\text{ }^\circ\text{C}$ , gradual cooling in an oil bath), seeding process ( $T_i = 50\text{ }^\circ\text{C}$ , heating rate =  $30\text{ }^\circ\text{C/hr}$ ,  $T_s = 68\text{ }^\circ\text{C}$ , gradual cooling in an oil bath). Type A crystals (upper) and Type B crystals (bottom).**

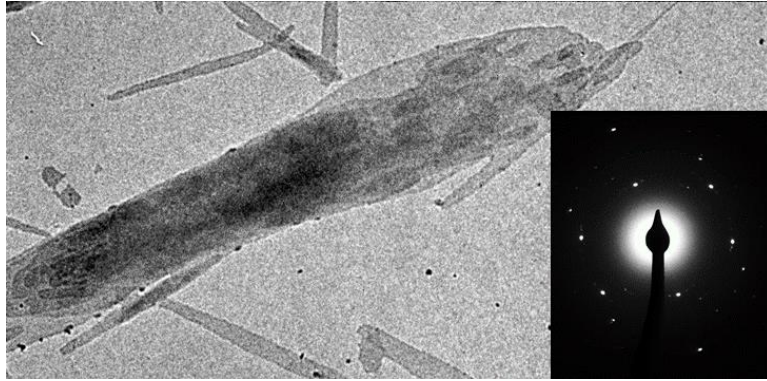


**Figure 5.4: An individual PHBHx(7.6mol%) single crystal grown by self-seeding and its EDP.**

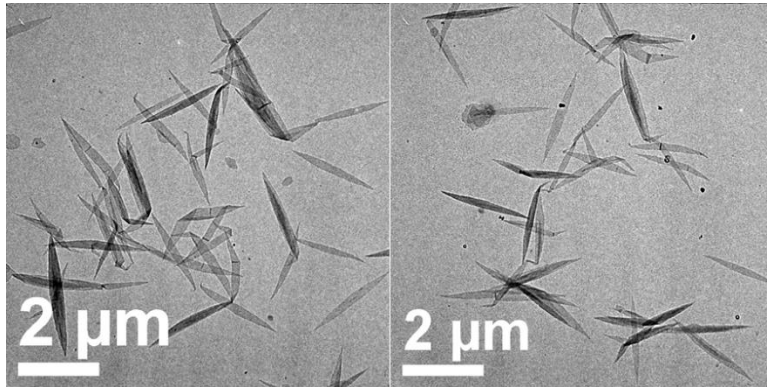


**Figure 5.5: PHBHx(13mol%) single crystals. Crystallization method: self seeding. Crystallization conditions: concentration = 0.01wt%, precursor preparation (pure EtOH,  $T_d = 110\text{ }^\circ\text{C}$ , gradual cooling in an oil bath),  $T_i = 50\text{ }^\circ\text{C}$ , heating rate =  $30\text{ }^\circ\text{C/hr}$ ,  $T_s = 79\text{ }^\circ\text{C}$ , gradual cooling in an oil bath)**

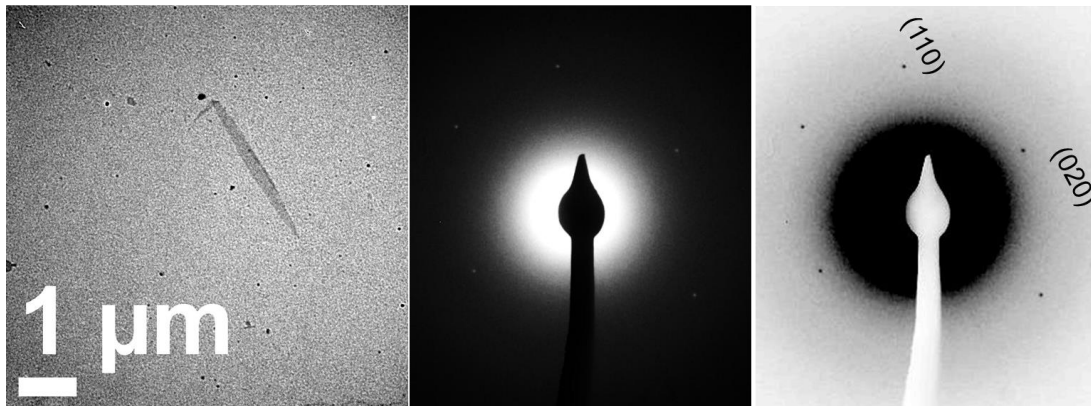


**Figure 5.6: Individual PHBHx(13mol%) single crystal grown by self-seeding and its EDP and color reverted EDP.**

## **5.2 Characteristic morphology of PHBHx(3.9mol%), PHBHx(7.6mol%), and PHBHx(13mol%) crystals**

Characteristic morphological features for each PHBHx crystals are discussed here.

A cracking behavior frequently occurs along the b direction for large single crystals of PHBHx(3.9mol%) and PHBHx(7.6mol%), as shown in Figure 5.7 and 5.8. Such cracking behavior was rarely found for PHBHx(13mol%) crystals and for self-seed single crystals. In addition, self-seeded crystals typically have a smaller size and it is possible that cracking is crystal size dependent.

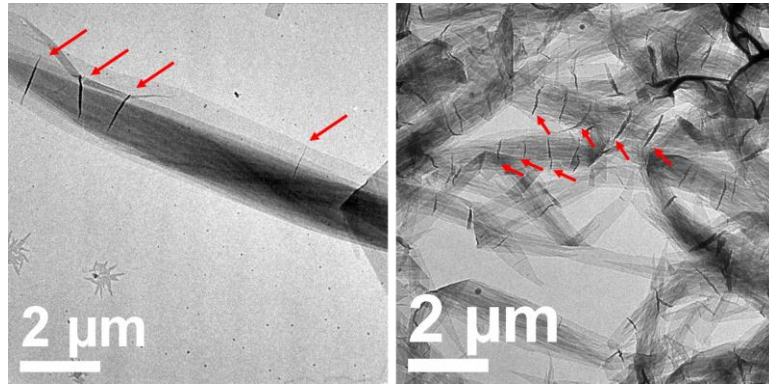


**Figure 5.7: PHBHx(3.9mol%) crystals. Left, crystallization method: gradual cooling. Crystallization conditions: concentration = 0.027wt%, EtOH,  $T_d = 110\text{ }^\circ\text{C}$ , gradual cooling in an oil bath. Right, crystallization method: isothermal crystallization. Crystallization conditions: concentration = 0.01wt%,  $\text{CHCl}_3/\text{EtOH}$  ratio = 0.11,  $T_c = 65\text{ }^\circ\text{C}$ . Red arrows indicate locations of cracks.**

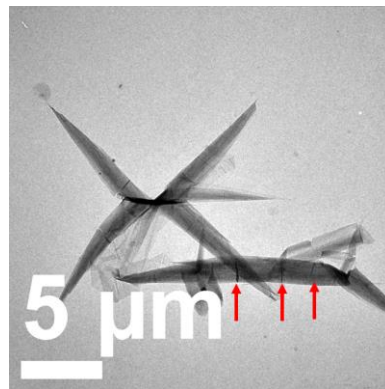


**Figure 5.8: PHBHx(7.6mol%) crystals. Crystallization method: gradual cooling. Crystallization conditions: concentration = 0.01wt%,  $T_d = 110\text{ }^\circ\text{C}$ , cooled in an oil bath. Red arrows indicate locations of cracks.**

An abrupt folding phenomenon for PHBHx(3.9mol%) and PHBHx(7.6mol%) crystals was frequently found. These are shown by the red arrows in Figure 5.9 and

5.10. No folded crystals were found for PHBHx(13mol%) crystals. This possibly is indicative of significant brittleness in low 3HHx content PHBHx.

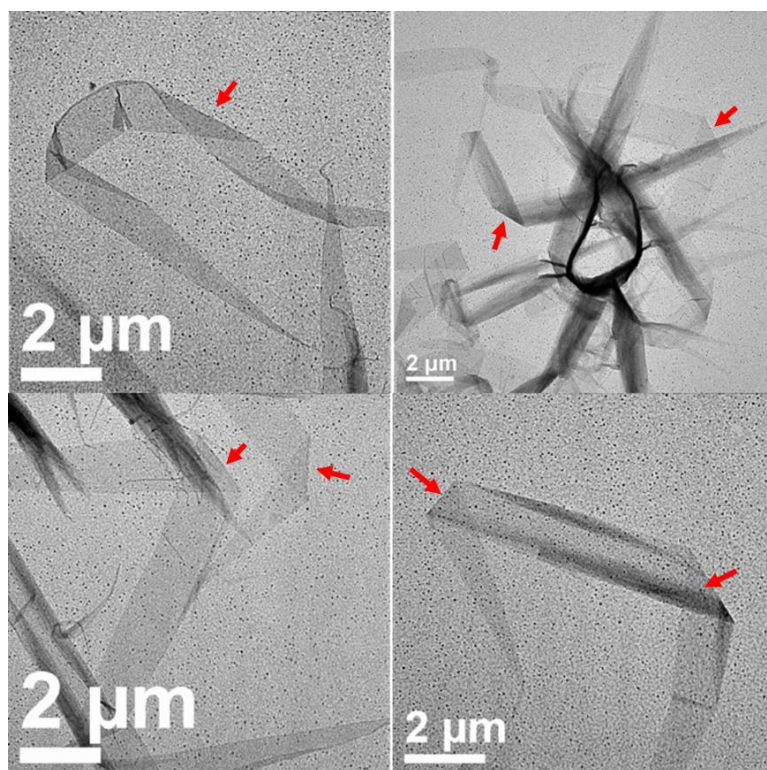


**Figure 5.9: PHBHx(3.9mol%) folded crystals. Crystallization method: gradual cooling. Crystallization conditions: concentration = 0.027wt%, EtOH,  $T_d = 110\text{ }^\circ\text{C}$ , oil bath. Red arrows indicate folding positions.**

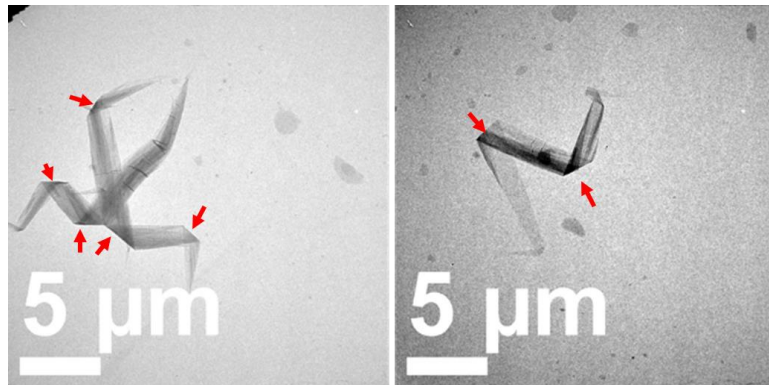


**Figure 5.10: PHBHx(3.9mol%) folded crystals. Crystallization method: gradual cooling. Crystallization conditions: concentration = 0.01wt%, EtOH,  $T_d = 110\text{ }^\circ\text{C}$ , cooled in an oil bath. Red arrows indicate location of folds.**

Branching and twisting was found only for PHBHx(13mol%), which frequently had spherulites developed with branching and twisting, as shown in Figure 5.11 and 5.12. We also found lamellar twisting that increases from the single crystal to the early stages of spherulite formation and then on to mature spherulites. Such twisting is not seen for PHBHx(3.9mol%) crystals. One potential twisting mechanism involves repulsion from neighboring lamellae.<sup>19</sup> However, this does not explain our case due to the fact that we are using such dilute solutions. In our case, twisting is most likely related to the congested packing of excluded 3HHx on the fold surface. The formation of twists may help relieve local stresses caused by bulky 3HHx packing.

In summary, we conclude that 3HHx groups have very small effect on the PHBHx crystal form and growth habits of single layered single crystals, but has a prominent effect on influencing hierarchical crystal morphologies.

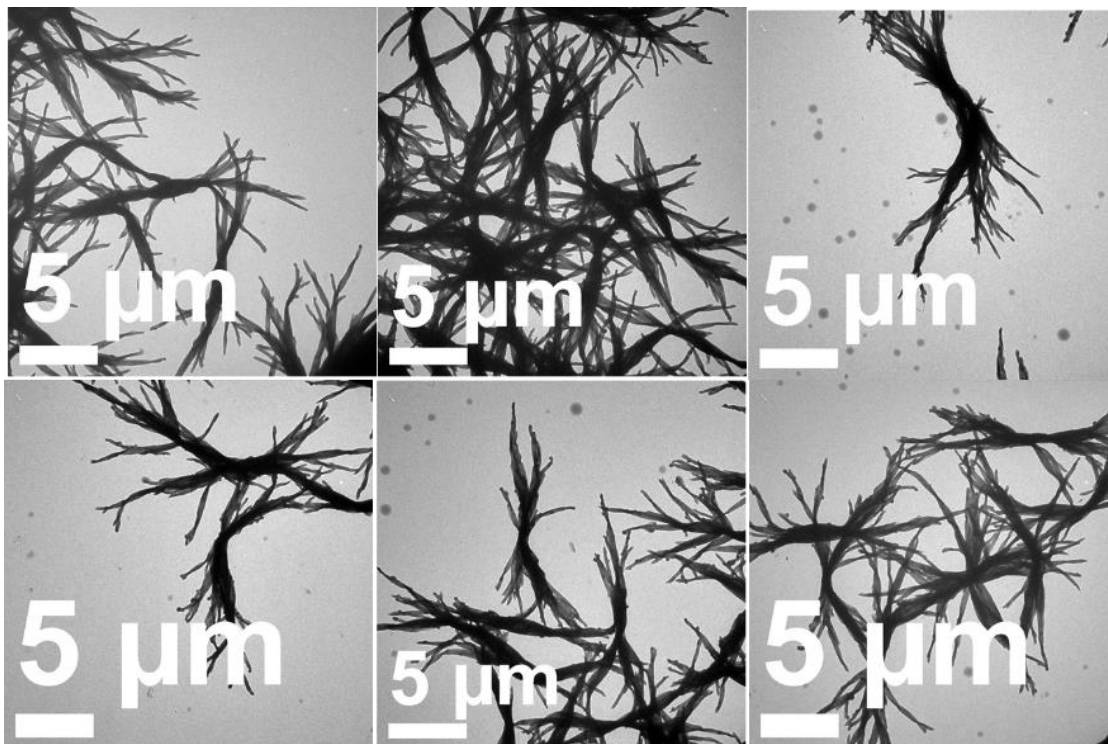


**Figure 5.11: PHBHx(13mol%) premature spherulites. Crystallization method: isothermal crystallization. Crystallization conditions: concentration = 0.01wt%, CHCl<sub>3</sub>/EtOH ratio = 0.025, T<sub>c</sub> = 45 °C.**

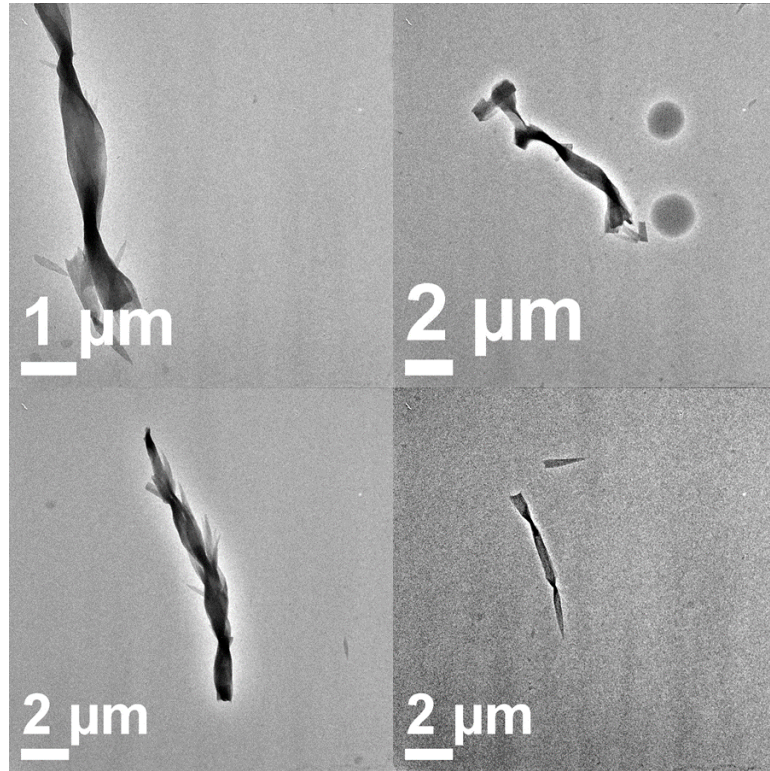


**Figure 5.12. PHBHx(13mol%) twisted lamellae. They are created by ultrasonification of PHBHx(13mol%) spherulites. Crystallization method: gradual cooling. Crystallization conditions: concentration = 0.01wt%, EtOH,  $T_d = 110\text{ }^{\circ}\text{C}$ , air cooling.**

## Chapter 6

### CRYSTALLIZATION OF PHB AND PHBHx ULTRATHIN FILMS ON METAL OXIDE FLAT SURFACES

#### 6.1 Discovery of the crystallization retardation of PHBHx(13mol%) thick sheet sandwiched by Al foil

The unexpected discovery of aluminum oxide, or AO, induced PHBHx crystallization retardation effect was accidental. Originally, we attempted to induce the beta crystalline form of PHBHx by applying static electric fields across a PHBHx film. The beta crystal form of PHB has useful properties including piezoelectricity.<sup>20–22</sup> To apply an electric field for poling, two pieces of commercial Al foil were attached to a thick PHBHx(13mol%) sheet (approximately 3 to 4 mm). In this and the following chapters, a sheet and a film are referred to as having a thickness over 200  $\mu\text{m}$ , and below 200 $\mu\text{m}$ , respectively. The whole processing route is shown in Figure 6.1. In order to fabricate a sandwiched structure, a Carver Press was used. An amount of as received PHBHx(13mol%) powder was placed between two pieces of Al foil, and then pressed at 160 °C for 2 mins to form a sandwich structure. Then the laminate was quickly removed from the Carver Press and quenched into ice water to prevent crystallization.

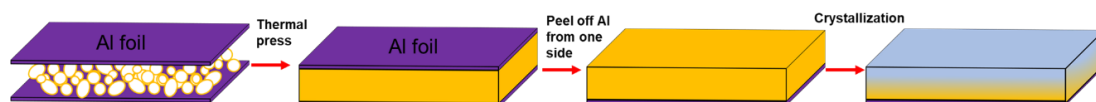


**Figure 6.1: A schematic to show Al foil sandwiched PHBHx sheet and removal of one-side of the Al foil**

The laminate was quickly brought to room temperature to remove one-side of the Al foil (Figure 6.1), leaving the other side untouched, and the whole sample was allowed to crystallize at room temperature. Thus, the side of sheet without Al will crystallize naturally, and the side with Al foil crystallizes under contact with Al. After crystallization for a given amount of time, FTIR in ATR mode was used to examine the crystallinity of the film by looking at the carbonyl stretching region. Experimentally, the exposed side of the film without Al foil can simply be placed in contact with the ATR crystal. For the side of film still in contact with the Al foil, a small Al foil patch, approximately  $0.5 \times 0.5 \text{ cm}^2$ , was peeled off, followed by quickly placing it on the ATR crystal for spectral acquisition. The time from the actual peeling-off process to the taking of a spectrum is less than 3 mins. Figure 6.2 shows the carbonyl region of the side with Al foil after 12 hrs and without Al foil after 4 hrs crystallization. For the side without Al foil, after 4 hrs, the alpha crystal peak at  $1723 \text{ cm}^{-1}$  clearly developed, and the  $1742 \text{ cm}^{-1}$  amorphous carbonyl band is also observed. For the Al-coated side after 12 hrs, the peak maximum is found at  $1736 \text{ cm}^{-1}$ . The apparent occurrence at  $1736 \text{ cm}^{-1}$  is most likely due to the combination of  $1723 \text{ cm}^{-1}$  and  $1742 \text{ cm}^{-1}$ , indicating that the polymer is at the early stage of crystallization. It is expected that after longer times, the red spectrum should have a similar line shape as that of black spectrum. Therefore, this experiment indicates that PHBHx(13mol%) crystallizes much slower when it is in contact with Al foil. It is worth noting that when removing the Al foil, we could even feel the adhesion of the Al foil and the polymer interface.

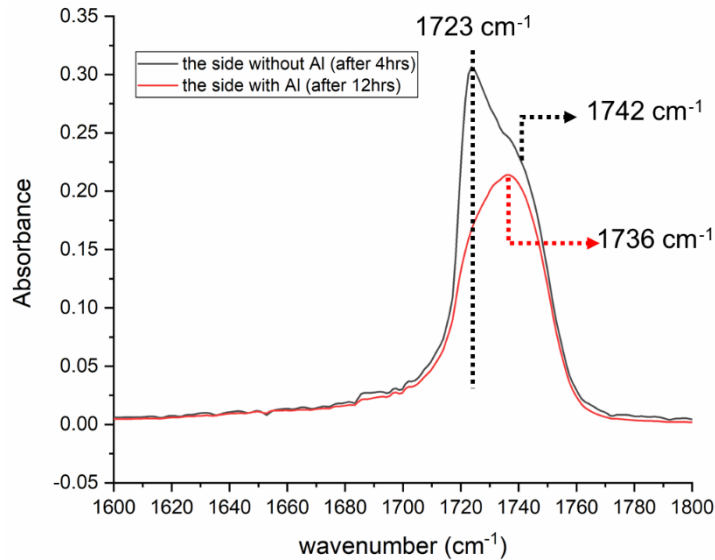


**Figure 6.2: The carbonyl regions of FITR-ATR spectra for PHBHx(13mol%) thick sheet. Black: the side of sheet without Al foil after a 4-hour at room temperature; Red: the side of sheet with Al foil after 12-hour at room temperature.**

The above discovery is very intriguing but also raises some issues which hinder the conclusion that the crystallization retardation is indeed due to PHBHx interacting with the Al surface. First, the surface chemistry of commercialized Al foil is not very clear. Commercialized Al foil may have a thin coating layer, which may also interact with PHBHx to disrupt its crystallization. Second, due to a relatively high ductility and flexibility of Al foil, the thermal pressing process may lead to the Al foil inserting into the interstitial region between PHBHx spheres (powders) both macroscopically and microscopically, resulting in an increased effective contact area between Al and PHBHx. Increasing contact area is known to also help reduce crystallization rate. Third, the thermal pressing process may induce a thermal

decomposition of PHBHx, leading to the formation of a new species such as acrylic acid and crotonic acid,<sup>23,24</sup> a small molecule which is not capable of crystallizing at room temperature but can act as a retarder for polymer crystallization. Due to these potential interference factors, therefore, a rigorous experimental design with improved control is required. In addition, we also studied other metals with an oxidized surface to see if they can also retard crystallization of PHBHx.

## **6.2 Flat metal coated glass substrates**

Flat aluminum, silver, and copper coated glass substrates were purchased from Deposition Research Lab Inc. The metal layer was deposited on a flat glass substrate by physical vapor deposition. All the deposited layers have a thickness of approximately 100 nm. After receiving the substrates, they were allowed to naturally oxidize by being exposed to ambient air at room temperature (around 23 °C). Flat gold-coated glass substrates prepared by chemical vapor deposition were purchased from Platypus Technologies LLC. The deposited layer is also approximately 100 nm thick. Surface roughness for all the surfaces was determined using a Dimension 3100 atomic force microscope. The measured height profiles for an area of  $5 \times 5 \mu\text{m}^2$  are shown in Figure 6.3. Measured  $R_q$ , or root mean square for all the samples are listed in the Figure. It was observed that the Al substrate has the highest surface roughness whereas the Cu substrate has the lowest. However, the surface roughness for all the substrates are on the same order of magnitude.

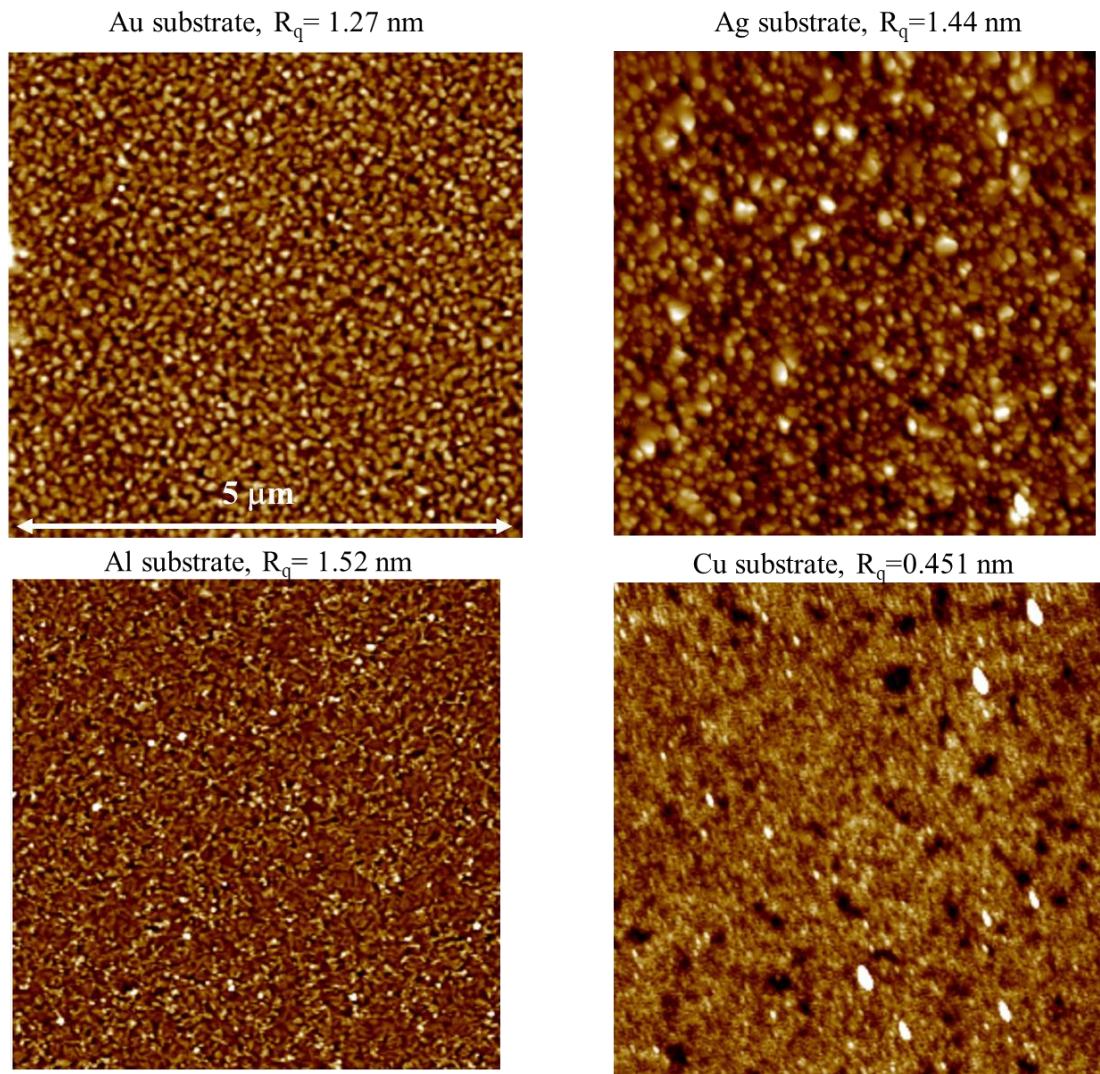


**Figure 6.3: AFM height images for gold, silver, aluminum, and copper surfaces and their corresponding  $R_q$ .**

### 6.3 Thin film preparation and melt crystallization on surfaces

All thin films were prepared by spin coating onto the substrate. Specifically, before spin-coating, the substrates were purged in the spin coater chamber under

nitrogen for 30 mins to remove physically adsorbed water. A solution of 0.5 wt% of PHB or PHBHx in chloroform was used for spin coating and a 0.5 ml of polymer solution was used. A 1300 rpm/sec acceleration rate was used, and the spin coater was operated at 4000 rpm for 3 mins. These spin coating conditions resulted in a thin film of approximately 40 nm in thickness, which was determined using X-ray reflectometry (XRR). The XRR experiment was conducted using a Rigaku XRD operating with Cu K-alpha radiation and an X-ray wavelength of 0.154 nm. Film thickness was determined by taking the Fourier Transform of the fringe pattern as shown in Figure 6.4.

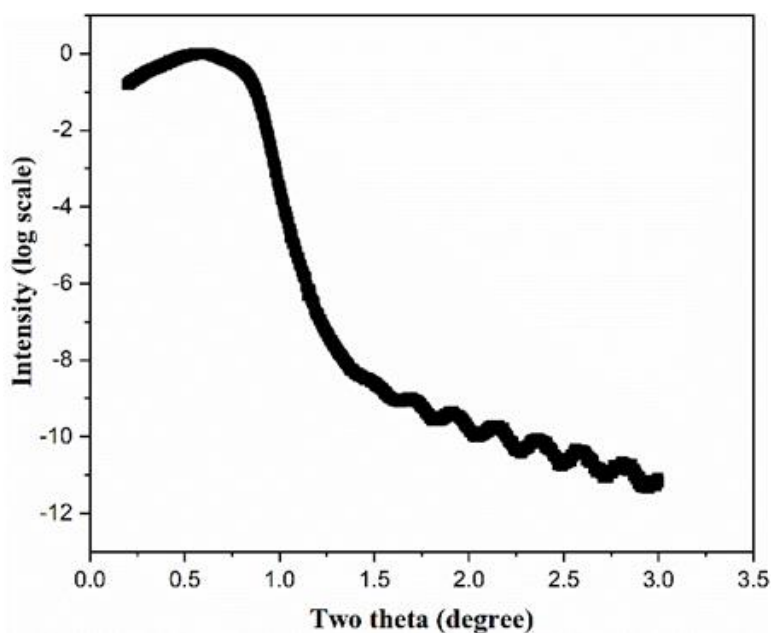


**Figure 6.4: Typical XRR profile of spin coated ultrathin film**

A schematic for the thin film processing steps is shown in Figure 6.5. After spin coating, the as-spin-coated film was placed on a preheated hotplate with a

ceramic surface so as to melt the PHB or PHBHx. After melting occurred, the sample was immediately placed in contact with a 5 °C copper surface to cool it down to room temperature. The sample was then rapidly transferred into the infrared spectrometer equipped with a grazing incident infrared reflection absorption spectroscopy (IRRAS) accessory. Room temperature crystallization of the thin film was then monitored by recording the IR spectra as a function of time. The interval between cooling and recording the first spectrum was 2 min. The exact melting time applied for each sample was dependent on the specific polymer and substrate used.

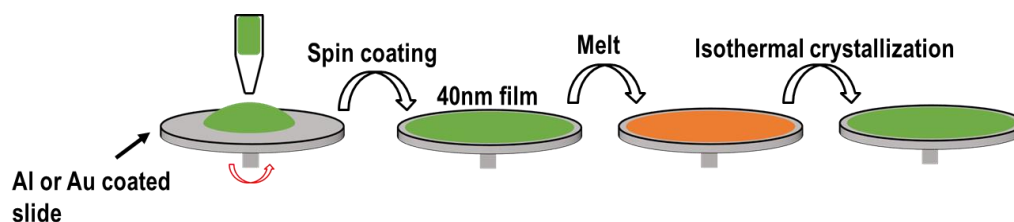


**Figure 6.5: Schematic of processing procedures for spin coating and melt crystallization.**

#### **6.4 Typical IRRAS spectra changes during crystallization at room temperature**

A PHB thin film on Au was used as an example to show the typical IR bands. It was found that the crystallization of PHB on gold was complete within 120 mins. IRRAS spectra taken at 2, 5, 10, 15, and 120 mins are displayed in Figure 6.6 to show the typical changes for the carbonyl and backbone regions during crystallization.

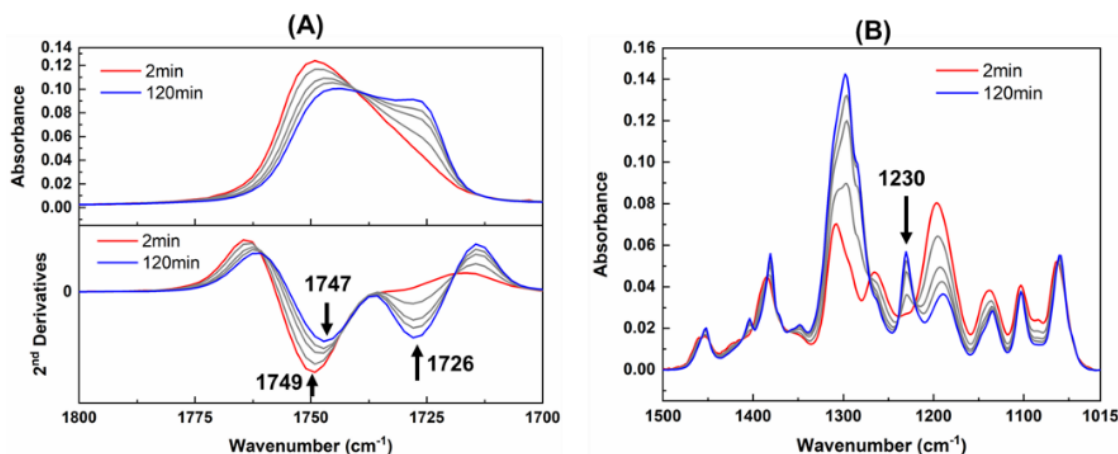


**Figure 6.6: IRRAS and 2nd derivative spectra of carbonyl stretching region (A) and the backbone region (B) for PHB crystallization on gold at room temperature.**

In the carbonyl stretching region (Figure 6.6(A)), only a peak at  $1749\text{ cm}^{-1}$  appears at the very beginning, which is attributed to the carbonyl stretching vibration from the amorphous component of the ultrathin film material. As crystallization proceeds, a peak located at  $1726\text{ cm}^{-1}$ , assigned to the carbonyl stretch in alpha crystals<sup>25</sup>, grows. In addition, with increased crystallization, the amorphous peak maximum at  $1749\text{ cm}^{-1}$  shifts to approximately  $1747\text{ cm}^{-1}$  indicating the local environment of an amorphous carbonyl changes from a less restricted environment to a more restricted environment. Crystallization of the alpha form is also observed by examining the backbone region (Figure 6.6(B)). The peak located at  $1230\text{ cm}^{-1}$  has been assigned to a  $\text{-C-O-C-}$  stretching band in the crystalline region.<sup>26</sup> The bands at  $1230\text{ cm}^{-1}$  and  $1726\text{ cm}^{-1}$  were observed to increase in intensity simultaneously. The  $1230\text{ cm}^{-1}$  band is well isolated, which makes data processing simpler, so this band is used to reflect crystallization of PHB and PHBHx.

### 6.5 Crystallization of PHB and PHBHx (13mol%) thin films on different surfaces.

Let us first examine the crystallization profiles of PHB on different surfaces. Figure 6.7 shows the plot of peak intensity of the  $1230\text{ cm}^{-1}$  band as a function of crystallization time (up to 120 mins) for PHB on Au, Al, Ag, and Cu substrates. That the four curves have different y-axis values at the start is most likely due to slightly different absorption factors for different metal surfaces, as documented in Greenler's paper.<sup>14</sup> PHB shows the fastest crystallization rate on gold and it crystallizes on a Ag substrate at a slightly slower rate. Crystallization of PHB is significantly retarded on both Al and Cu substrates and the rates are similar.

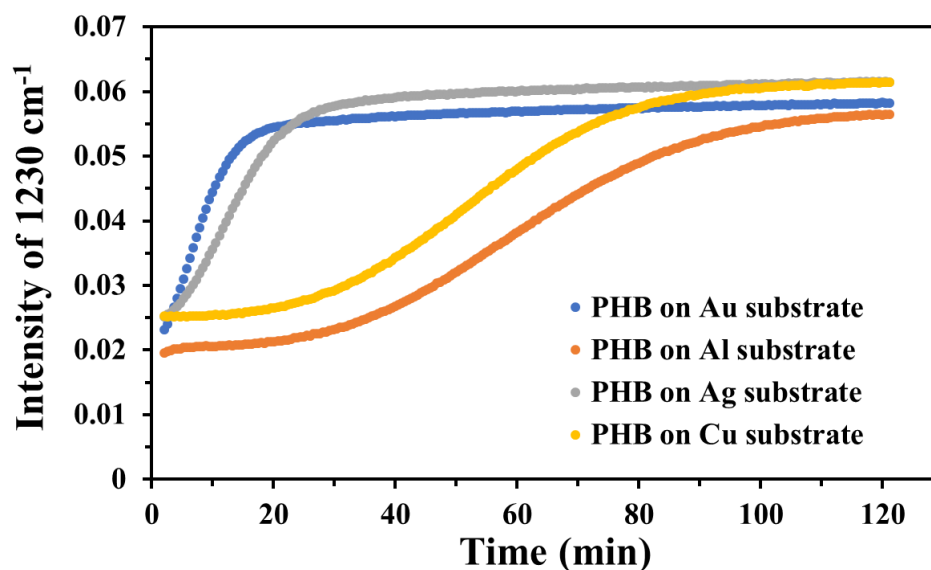
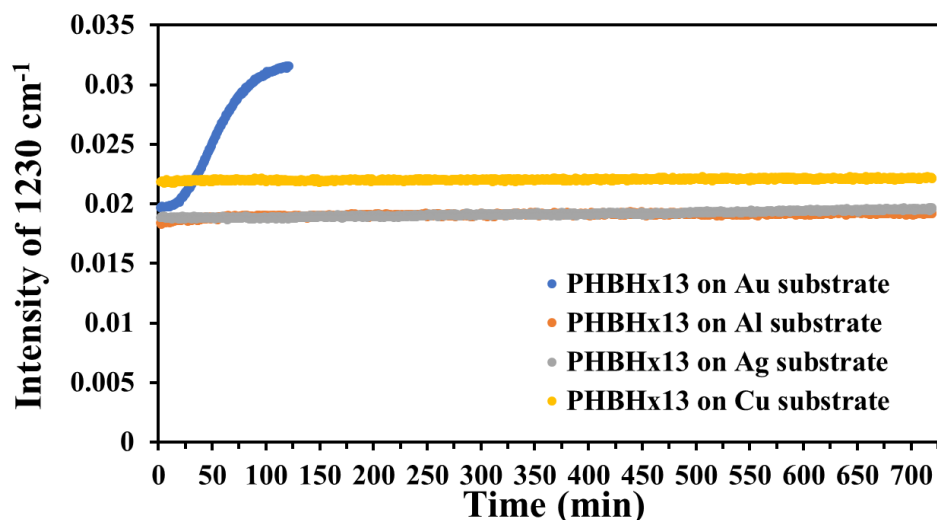


Figure 6.7: The intensity plot of the IR peak at  $1230\text{ cm}^{-1}$  against crystallization time for PHB thin films on different substrates.

Figure 6.8 shows the plot of intensity of the  $1230\text{ cm}^{-1}$  band as a function of crystallization time (up to 720 mins) for PHBHx(13mol%) on Au, Al, Ag, and Cu substrates. At around 100 mins, primary crystallization has finished for PHBHx (13mol%) on a Au substrate. The peak intensity of the  $1230\text{ cm}^{-1}$  band for PHB on Au (blue profile in Figure 6.7) can reach a value as high as around 0.06, whereas that for PHBHx (13mol%) on Au (blue profile Figure 6.8) only reaches a value of 0.03. This is most likely due to the intrinsically low crystallinity of PHBHx (13mol%). The most intriguing observation in Figure 6.8 is that all three substrates, Ag, Al, and Cu significantly hinder PHBHx (13mol%) crystallization as indicated by the fact that after 720 mins, the polymer shows no sign of crystallizing. In addition, the behavior of the Ag substrate is interesting and shows a slight retardation effect on the PHB crystallization, but can be observed to retard PHBHx crystallization significantly, similar to the Al and Cu substrates.



**Figure 6.8:** The intensity plot of the IR peak at  $1230\text{ cm}^{-1}$  against crystallization time for PHBHx (13mol%) thin films on different substrates.

## 6.6 XPS studies on different metal surfaces

*Al substrate.* Elemental analysis of the surface of an Al substrate was investigated using XPS, as shown in Figure 6.9. Al 2p and O 1s profiles clearly indicate the presence of aluminum oxide (AO) on the surface. This is expected since aluminum is readily oxidized under ambient conditions. In addition, a weak hydroxyl peak (from peak fitting) from Al-OH was observed, indicating that a trace amount of chemically bound -OH is present on the AO surface.

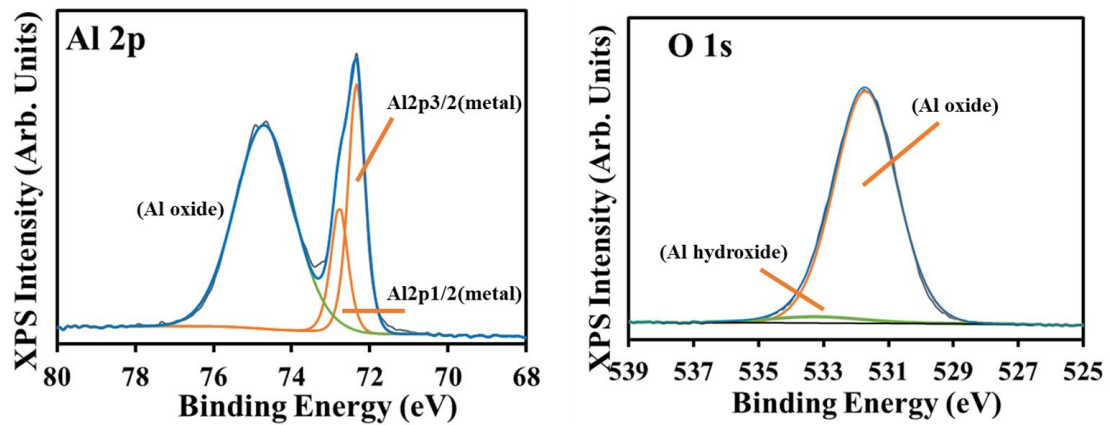


**Figure 6.9: XPS profiles of the surface of the aluminum substrate. Left: Al 2p profile. Right: O 1s profile.**

*Cu substrate.* Figure 6.10 shows the Cu 2p profile for the Cu surface. A CuO (the shoulder indicated by red arrow) peak can be identified. The 952.5 eV and 932.9 eV peaks may arise from metallic copper or Cu<sub>2</sub>O.

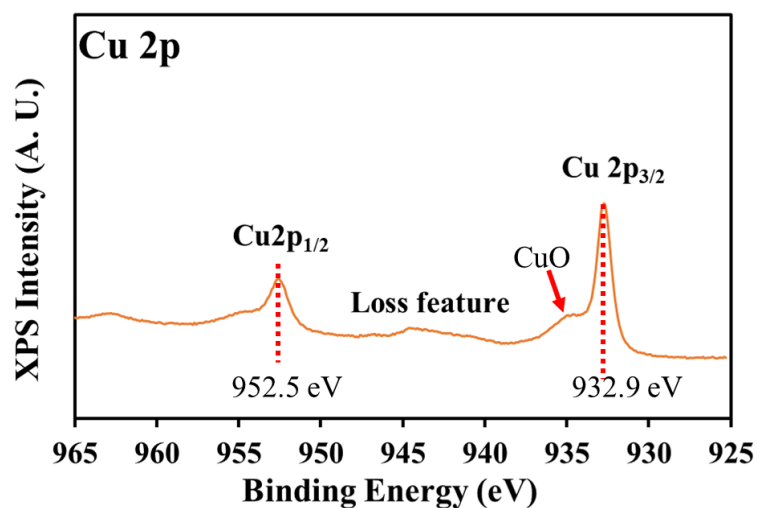


**Figure 6.10: XPS Cu 2p profiles of the surface of the copper substrate.**

*Ag substrate.* Figure 6.11 shows the Ag 3d profile. The red profile for as received Ag substrates shows two peaks assigned to metallic silver, suggesting the Ag surface is not oxidized. Though it is typically believed that silver can be oxidized to form a thin oxide layer, the oxidation kinetics depends on the preparation methods for metallic silver. Physical vapor deposition is more likely to give rise to Ag metal due to the vacuum environment. In contrast, the preparation of Ag metal by the reduction of silver salt in solution can lead to a relatively thick oxide layer.

An annealing experiment was carried out by placing the as-received Ag substrate on a 400 °C hotplate at normal pressure. The XPS profile for the annealed sample corresponds to the black curve in Figure 6.11. An obvious peak shift for both Ag 3d peaks can be identified, suggesting the surface is indeed converted to silver oxide after the annealing treatment. This result confirms that no oxide layer exists before annealing.

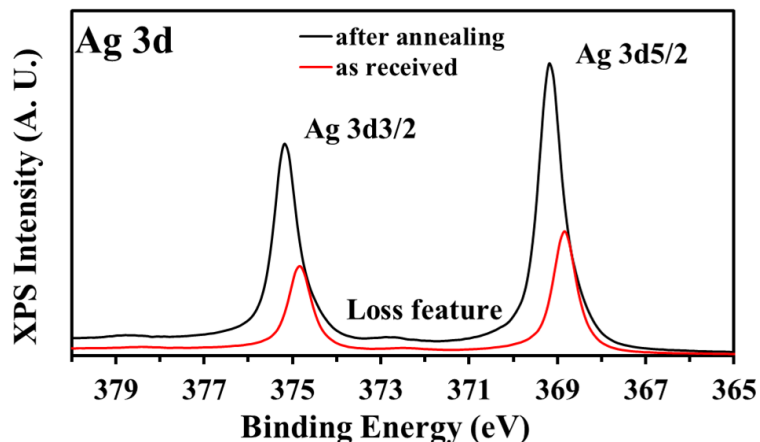


**Figure 6.11: XPS Ag 3d profiles of the surface of a silver substrate before (red) and after (black) annealing treatment.**

In summary, as expected, Al and Cu substrates were found to have oxide layers, whereas the Ag substrate stays in a metallic phase in an ambient environment. The detailed retardation mechanism for an Al substrate will be presented separately in chapter 7. No in-depth study was conducted for the case of a Cu substrate since it was found that the Cu substrate was easily oxidized during heating in the film melting process, suggesting a high reactive nature for the copper surface. Thus, we decided not to further study the effect of Cu substrate on polymer crystallization. However, the oxidation process of the Cu substrate during heating while coated with PHB or PHBHx is intriguing as shown in Figure 6.12. The as-received Cu substrate at room temperature appears golden. During film melting (heating), it was noticed that two exposed areas, originally golden colored, turned to a deep red color within 2 mins. Interestingly, copper under the polymer coated area remains golden in color with no

evidence of changing color. This observation implies that PHB and PHBHx ultrathin films exhibit good oxygen barrier properties even when the polymer is melted.

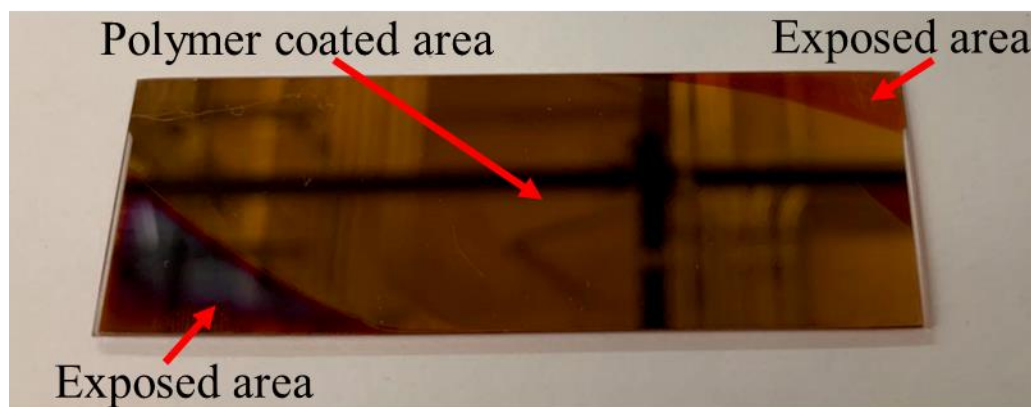


**Figure 6.12: Partially coated PHBHx on a Cu substrate after film melting.**

Figure 6.13 shows the contact angle measurement on Ag and Au substrates using a polar liquid, water, and a dispersive liquid, methyl iodide, or MI. The relative polarity of each surface can be evaluated using an Owens and Wendt analysis.<sup>27</sup> The Owens and Wendt equation has the form of:

$$1 + \cos \theta = 2\sqrt{\gamma_s^d} \left( \frac{\sqrt{\gamma_l^d}}{\gamma_{lv}} \right) + 2\sqrt{\gamma_s^p} \left( \frac{\sqrt{\gamma_l^p}}{\gamma_{lv}} \right)$$

where  $\theta$  is the measured contact angle of a test liquid on the substrate,  $\gamma_s^d$  and  $\gamma_s^p$  are the dispersion component and the polar component of the surface energy of the solid substrate, respectively.  $\gamma_l^d$  and  $\gamma_l^p$  are the dispersion component, and the polar component for the test liquid.  $\gamma_{lv}$  is the surface free energy of the test liquid droplet under equilibrium with its vapor phase. Measured contact angle and derived surface energies are shown in Table 6.1. It is seen that Ag and Au substrates have very similar

surface energy profiles. For both surfaces, the dispersive component dominates the total surface energy. Thus, the interaction between the polymer and both Au and Ag substrates should be similar. So far it is not well understood why PHBHx(13mol%) crystallizes much slower on a Ag substrate than on a Au substrate.

#### Contact angle measurement on Au substrate

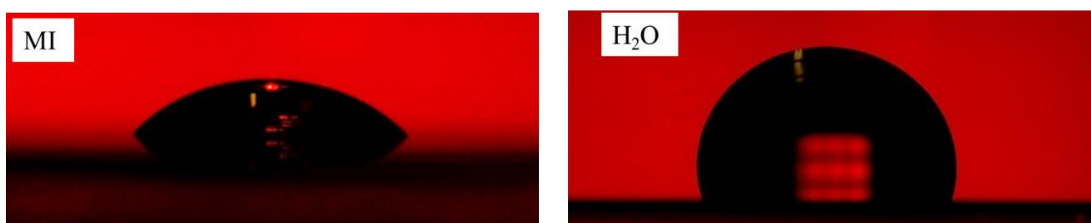


**Figure 6.13: Static contact angle measurement for a Au surface. Left: test liquid methyl iodide; right: DI water**

#### Contact angle measurement on Ag substrate

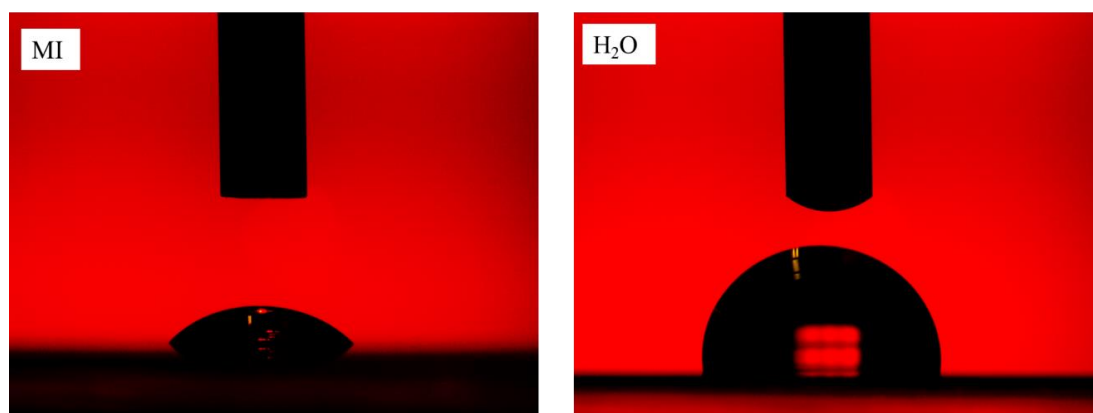


**Figure 6.14: Static contact angle measurement for Ag surface. Left: test liquid methyl iodide; right: DI water**

**Table 6.1: Calculated surface energy for gold and silver surfaces**

Surface	Measured contact angle (°)		Total surface energy (ergs cm <sup>-2</sup> )	Surface energy composition (ergs cm <sup>-2</sup> )		Dispersive percentage	Polar percentage
	H <sub>2</sub> O	MI*		dispersive	polar		
<b>Au</b>	90.3	29.1	44.7	44.2	0.5	98.8%	1.2%
<b>Ag</b>	96.4	50.0	34.3	33.8	0.5	98.5%	1.5%

## Chapter 7

### CRYSTALLIZATION RETARDATION OF ULTRATHIN FILMS OF POLY[(R)-3-HYDROXYBUTYRATE] (PHB) AND A RANDOM COPOLYMER POLY[(R)-3-HYDROXYBUTYRATE-CO-(R)-3- HYDROXYHEXANOATE] (PHBHx) ON AN ALUMINUM OXIDE SURFACE

Among all the metals or metal oxides tested in Chapter 6, aluminum has practical applications in the polymer industry. Thus, detailed studies on the crystallization retardation effect of PHB and PHBHx ultrathin films on an Al substrate are explored in this chapter.

#### 7.1 Crystallization kinetics of PHB, PHBHx(5.8mol%), PHBHx(9.4mol%) and PHBHx(13mol%) on gold and aluminum substrates

As mentioned in Chapter 6, the 1230 cm<sup>-1</sup> IR peak can be used as a measure of crystallization of PHB and PHBHx. Therefore, the relative crystallinity of the film at any given time during crystallization can be described by

$$X_t = \frac{I_t - I_0}{I_\infty - I_0}$$

Where  $X_t$  is the relative crystallinity at time  $t$ , and  $I_0$ ,  $I_t$ , and  $I_\infty$  are 1230 cm<sup>-1</sup> peak intensities at time zero, time  $t$ , and time infinity. The value used for  $I_\infty$  was taken from the sample after five-day crystallization at room temperature. This is because the major development of the overall crystallinity is derived from primary crystallization, which is defined below. The overall crystallization can be typically divided into three

regions as shown in Figure 7. They are the induction period, primary crystallization, and secondary crystallization.

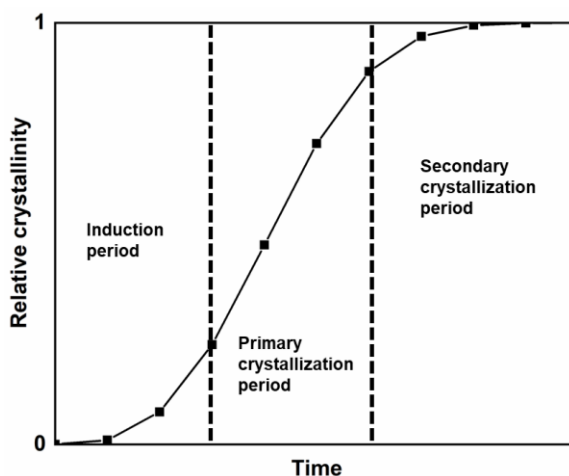


**Figure 7.1: A plot of relative crystallinity against time shows three crystallization stages: induction period, primary crystallization period, and secondary crystallization period.**

For our samples, the primary crystallization was mostly complete within five days, even for PHBHx(13mol%) on Al, which has the lowest crystallization rate. We will initially examine the kinetic curves of PHB and PHBHx films on a gold substrate as a function of 3HHx content as shown in Figure 7.2. First, the overall crystallization rate decreases with increasing 3HHx content. This is because a higher 3HHx comonomer content makes nucleation and growth more difficult. Chain mobility is reduced due to the steric effect of 3HHx, a relatively bulky medium-length-chain side group. Second, crystallization occurs relatively quickly for all the polymers on gold.

Even for PHBHx (13mol% 3HHx), after 120 mins, the primary crystallization was complete and the sample was well into the secondary crystallization period. This rapid crystallization rate implies the polymer has enough chain mobility to crystallize, possibly due to a weak interaction between polymer chains and a gold surface and the surface in contact with ambient air. We note that the very first spectrum for the PHB/Au sample already showed a small peak at  $1230\text{ cm}^{-1}$  (shown in Figure 7.3) indicating crystallization already occurred during cooling.

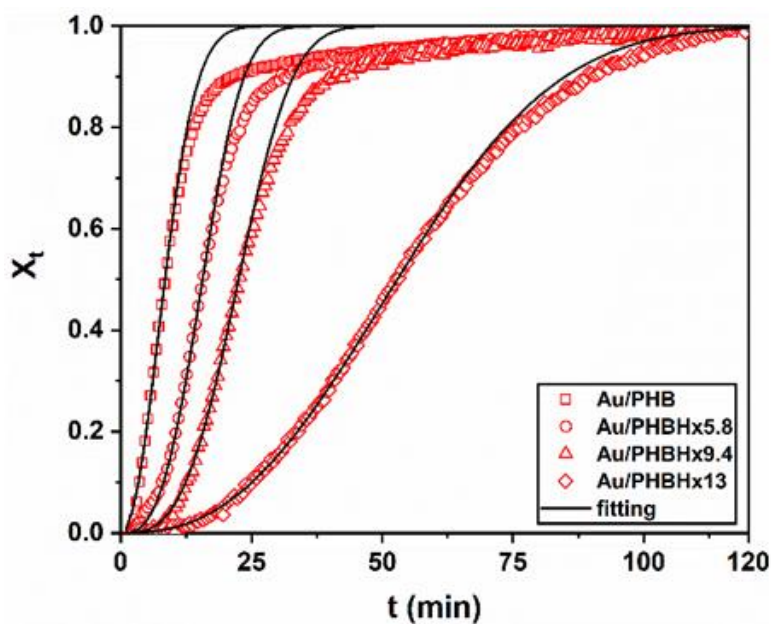


**Figure 7.2: PHB and PHBHx time-dependent crystallinity profiles on gold as a function of 3HHx concentration. Red profiles are experimental data points. Black profiles are fittings based on Avrami analysis.**

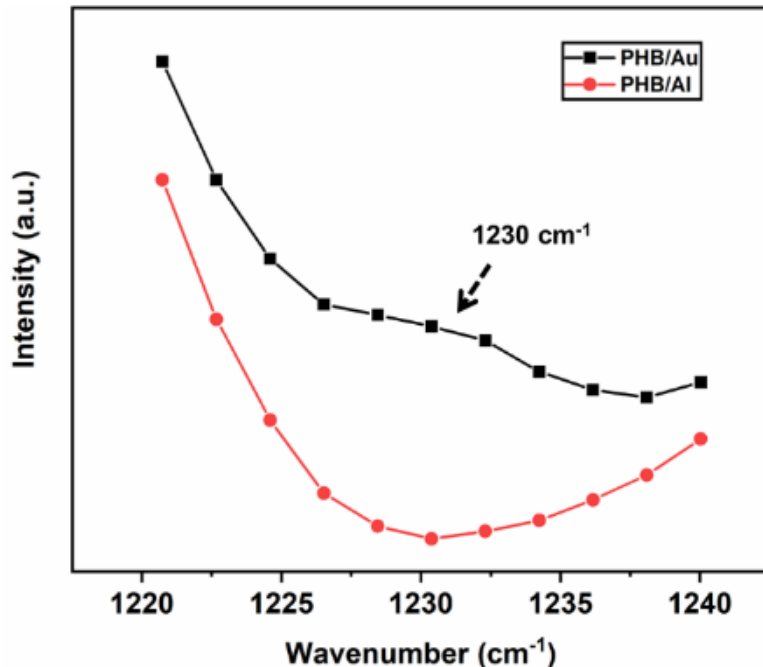


**Figure 7.3: -C-O-C stretching region of the very first IRRAS spectrum of PHB crystallization on gold and aluminum substrates. Red profile: on gold. Black profile: on aluminum.**

The kinetic curves for different polymers on Al and Au substrates are shown in Figure 7.4. For all polymers, crystallization on an aluminum substrate is significantly slower than that for a gold substrate. Especially interesting is the case of PHBHx(13mol%) (Figure 7.4(D)), where the induction period can last as long as 12 hours. It was also found that it took 48 hours for PHBHx(13mol%) to reach a crystallinity of 50%. Because we have previously shown that Au and Al surfaces have similar roughness, the explanation for the observed crystallization originates from the nature of the Al surface, or the aluminum oxide (AO) surface since Al oxidizes immediately in air.

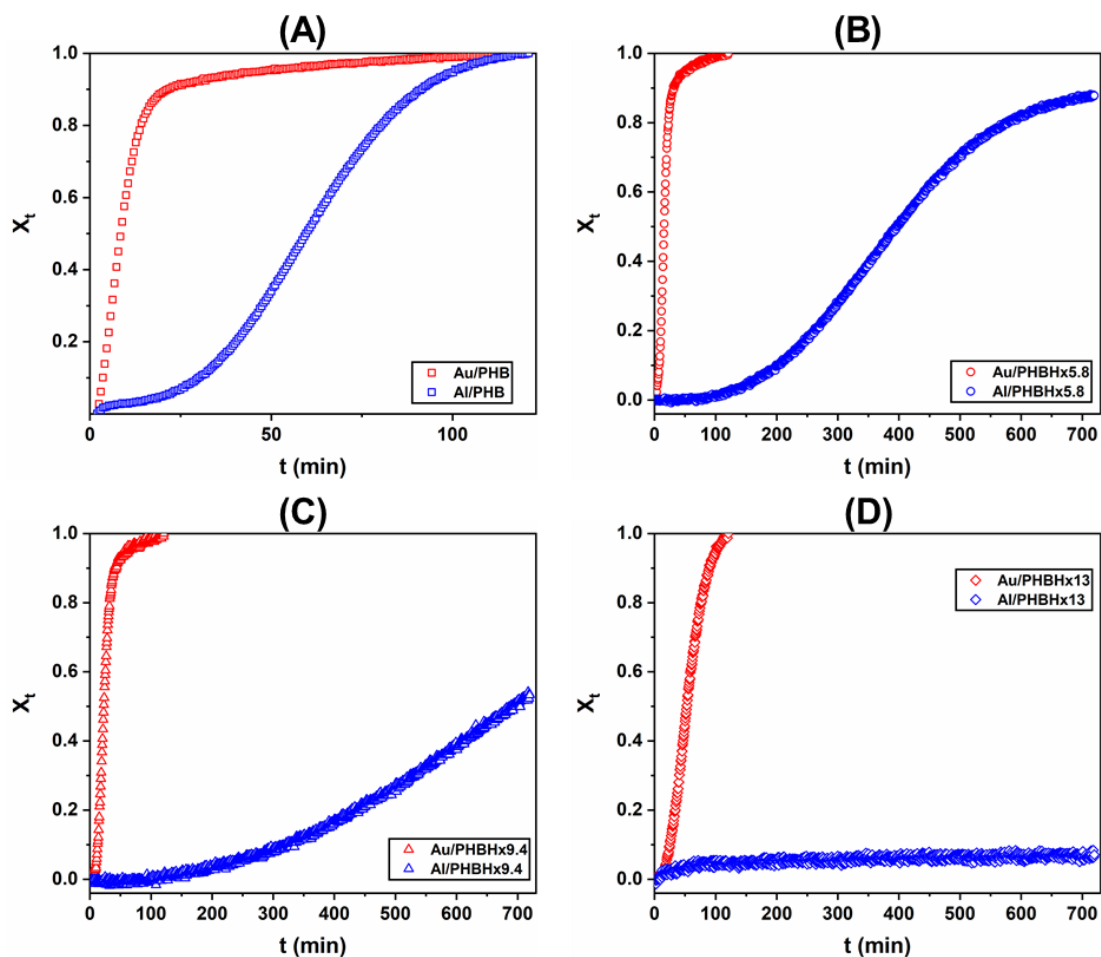


**Figure 7.4: Relative crystallinity profiles of different polymers on gold and aluminum substrates. (A) PHB; (B) PHBHx(5.8mol%); (C) PHBHx(9.4mol%); (D) PHBHx(13mol%). Red curve: gold. Blue curve: aluminum.**

## 7.2 Avrami analysis of crystallization kinetics

In order to further elucidate the effect of an aluminum substrate on the crystallization mechanisms, fitting the kinetic data to a classic Avrami equation was

attempted. The validation of applying the Avrami equation to two-dimensional ultrathin films has been demonstrated in previous work by others.<sup>28-30</sup> The Avrami equation can be expressed as  $X_t=1-\exp(-kt^n)$ ,<sup>31</sup> or in the form of double logarithm,  $\ln(-\ln(1 - X_t)) = \ln k + n \ln t$ , where,  $X_t$  is the relative crystallinity as mentioned before.  $k$  ( $\text{min}^{-1}$ ) is the overall crystallization rate constant accounting for both nucleation and growth processes, and  $n$  is the Avrami index, describing a crystallization mechanism. The overall Avrami index  $n$  can be further decomposed and described by,  $n = n_1 + cn_2$ , where  $n_1$  is the nucleation index,  $n_2$  is the growth dimensionality, and  $c$  is the growth index.<sup>32</sup> In our case, the growth dimension is 2 for all the samples so  $n_2 = 2$  because all the samples are two-dimensional ultrathin films. For a complete instantaneous nucleation,  $n_1 = 0$ , whereas for a complete sporadic nucleation,  $n_1 = 1$ . Nonintegral  $n_1$  were also found in many cases due to processes in between instantaneous and sporadic nucleation. The growth index  $c$  describes whether the crystallization mechanism is interface controlled or diffusion controlled. For a complete interface control,  $c = 1$ , whereas for a complete diffusion control,  $c = 0.5$ . Values in between 0.5 and 1 can be interpreted as both control factors contributing to the overall growth mechanism.

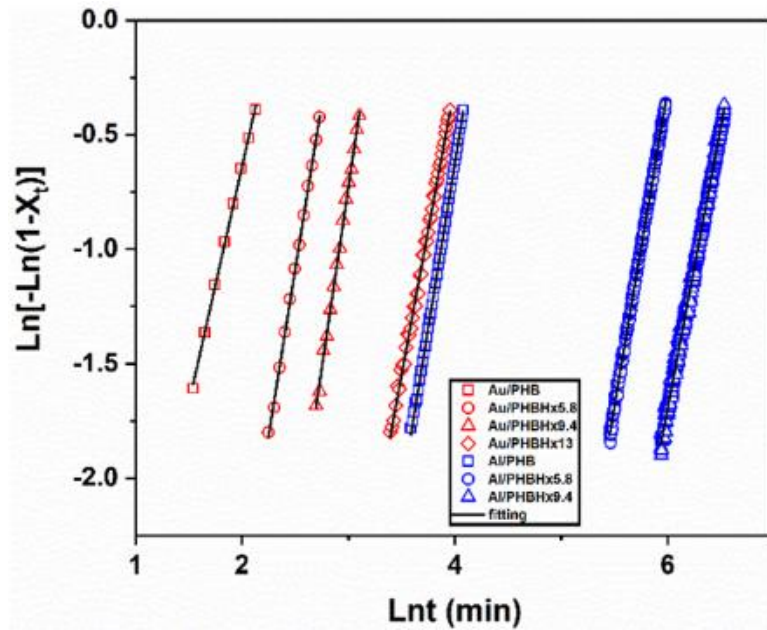


**Figure 7.5: Avrami plot of PHB and PHBHx with varying 3HHx content on gold (red) and aluminum (blue) substrates. Black lines are the fits.**

In the current study, kinetic data in the crystallinity range of  $15\% < X_t < 50\%$  was used for the curve fitting for all the samples. Results are shown in Figure 7.5. Due to an extensively long induction period, the fitting for PHBHx(13mol%)/Al failed, so it is not included in the figure. For all the other samples, the overall Avrami index  $n$  and rate constant  $k$  can be directly extracted from the curves, and they are listed in Table 7.1.

**Table 7.1: kinetic parameters derived from experimental Avrami analysis**

Surface Polymer	<i>n</i>	<i>k</i> (min <sup>-1</sup> )	<i>t</i> <sub>1/2</sub> (min)	
<b>Au</b>	<b>PHB</b>	2.07	8.41E-03	8
	<b>PHBHx5.8</b>	2.91	2.35E-04	16
	<b>PHBHx9.4</b>	3.16	3.71E-05	23
	<b>PHBHx13</b>	2.53	3.04E-05	53
<b>Al</b>	<b>PHB</b>	2.87	5.50E-06	60
	<b>PHBHx5.8</b>	2.76	4.65E-08	395
	<b>PHBHx9.4</b>	2.46	6.96E-08	693

The extracted values of *n* are plotted as a function of 3HHx content for gold and aluminum substrates, in Figure 7.6(A). When PHBHx is deposited on gold one observes that as 3HHx increases, *n* first increases, then decreases (for PHBHx(13mol%)). This result indicates that on gold, as 3HHx increases, nucleation becomes more difficult, making *n*<sub>1</sub> increase leading to an overall increase in *n*. When the 3HHx concentration increases to 13mol%, it is possible that diffusion occurs causing *c* to decrease, and thus leading to a decrease in *n*.

For crystallization on an Al substrate, two conclusions can be made from Figure 6(A). First, for PHB, the Avrami index *n*(Al) is greater than *n*(Au), indicating that the nucleation is more difficult on an Al substrate. Second, *n*(Al) decreases with increased 3HHx content. This monotonic decrease is different from the variable trend of *n*(Au) where *n*(Au) first increases and then decreases. Hypothetically this difference occurs because diffusion control starts taking effect at 5.8 mol% 3HHx content in the Al case. Since Avrami analysis is a semi-empirical method, supplementary experimental techniques, such as dielectric spectroscopy and quasi elastic neutron scattering, may be applied in the future to reveal more details of chain dynamics of PHB/PHBHx on AO surfaces.<sup>33</sup>

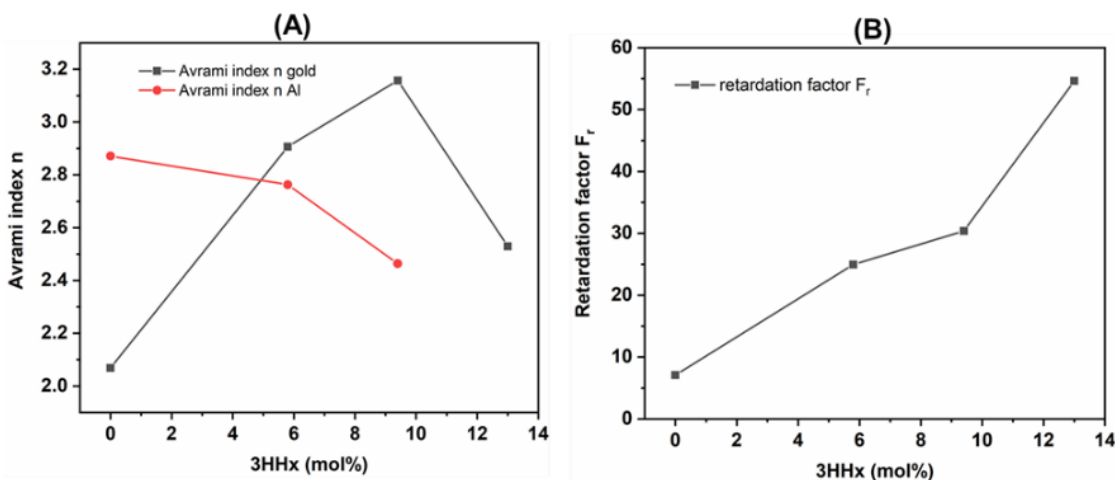


**Figure 7.6: (A) Avrami index plot against 3HHx content on gold (black) and aluminum (red) substrates. (B) plot of retardation factor  $F_r$  against 3HHx content.**

Now let us examine the overall rate constant  $k$ , as shown in Table 7.1. We found that on gold, all the polymers exhibit a rate constant,  $k$ , with a comparable order of magnitude to that found in the bulk.<sup>34</sup> This observation suggests that we have an ultrathin film system with comparable crystallization kinetics compared to the bulk. This result is most likely because the chain has enhanced mobility on the film/air interface, and has a weakened mobility on the substrate surface. These two effects cancel each other, giving rise to bulk-like crystallization kinetics. Our system, thus, is very different from the confined systems, such as in an AAO porous scaffold and in two-plate sandwiched structures.<sup>33,35</sup> In addition,  $k$  for PHB/Au is high, equivalent to a bulk crystallization rate at 48 °C or 90 °C.<sup>34</sup> This observation is additional evidence that, for this particular sample, the nucleation starts during cooling, consistent with the previous IR observation. However, the  $k$  values for polymers on aluminum, in general, are about 3 to 4 orders of magnitude less than those found on gold. For PHBHx with

high 3HHx content,  $k$  can be as low as  $10^{-8} \text{ min}^{-1}$ . The crystallization half time, denoted as  $t_{1/2}$  can be calculated from  $t_{1/2}=[(\log 2)/k]^{1/n}$  (or  $X_t=1-\exp(-kt_{1/2}^n)$ ). A retardation factor, hence, can be defined as  $F_r=t_{1/2}[\text{Al}]/t_{1/2}[\text{Au}]$  reflecting the inhibition effect of Al on crystallization for different polymers. The plot of  $F_r$  as a function of 3HHx is shown in Figure 7.6(B). One can clearly see that an aluminum substrate shows an increasing crystallization retardation effect for the copolymers with increased 3HHx, suggesting that at high 3HHx, the retardation effect is enhanced. This observation is consistent with our Avrami index analysis, i.e., at a higher 3HHx content, the diffusion control factor dominates, and Al has a more prominent hindering effect on the diffusion process.

### **7.3 Mechanistic study of crystallization retardation**

#### **7.3.1 H-bonding study between PHB/PHBHx and AO surface**

XPS data on the surface of an Al substrate, which was already shown in Chapter 6 is attached here for convenience, as shown in Figure 7.7. A weak hydroxyl peak (from peak fitting) from Al-OH was observed, indicating a trace amount of chemically bound -OH is present on the AO surface.

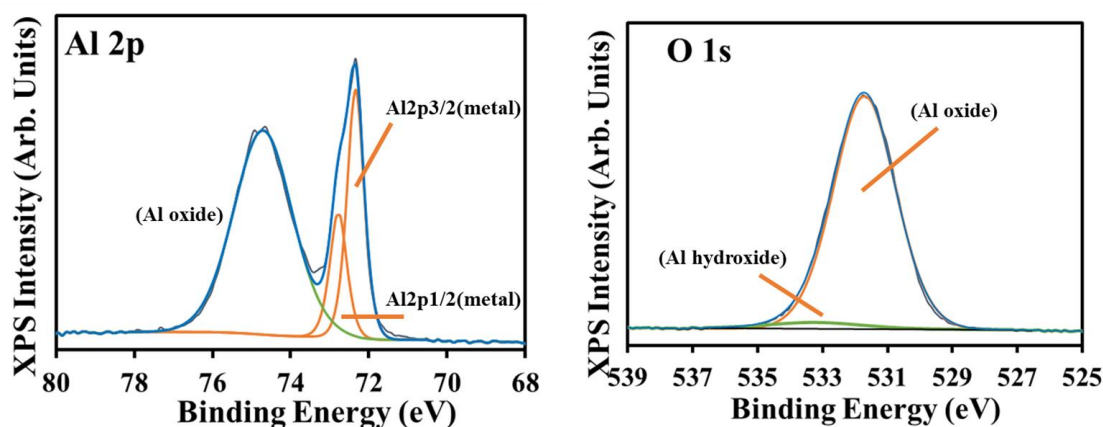


**Figure 7.7: XPS profiles of the surface of an aluminum substrate. Left: Al 2p profile. Right: O 1s profile.**

Previous studies showed that ester groups in certain polymers are able to form an H-bonded interaction with surface hydroxyl groups from an AO surface.<sup>36,37</sup> For instance, in the work by Brogly et al., the ester group in PMMA was able to H-bond with Al-OH, leading to a  $10\text{ cm}^{-1}$  red-shift of the carbonyl peak from  $1740\text{ cm}^{-1}$  to  $1730\text{ cm}^{-1}$ . Laila et al. found the ester group from poly(ethylene-*co*-butyl acrylate) (EBA) forms a H-bonded interaction with species on the AO surface, giving rise to an  $8\text{ cm}^{-1}$  red-shift of the carbonyl peak. In the current study, however, no evidence of a red-shift resulting from H-bonding was observed in all the samples. Three possible reasons are proposed for the absence of the red-shift of the carbonyl stretching band for PHB and PHBHx. First, it is possible that the H-bonding interaction does not exist, or if it does, the interaction might be too subtle to be detected by the IRRAS measurement. XPS data indeed shows that the existence of -OH species on AO is very minimal. In studies by Brogly et al. and Laila et al., the detailed chemical nature of the AO surfaces and the surface treatments used were not discussed. Thus, it is possible

that the AO surfaces used in their studies have more -OH than the AO surfaces used in our studies and this can lead to H-bond formation. Secondly, if we hypothesize that a trace amount of -OH can form H-bonds with the -C=O of PHB or PHBHx, then the interaction would be located near the 1-2 nm interfacial layer of polymer/substrate. A 40 nm film would be too thick for us to detect this potential H-bonding interaction. Thirdly, another possible reason for the absence of a red-shift could be that the new peak due to the potential H-bonding is obscured by the crystalline carbonyl peak at  $1726\text{ cm}^{-1}$  due to crystallization.

To eliminate the latter two possibilities, we used chemically synthesized atactic PHB (aPHB), which is incapable of crystallizing due to its atactic architecture. Thus, any red shift of the  $1749\text{ cm}^{-1}$  amorphous peak, must come from interaction between aPHB with an AO surface. In addition, to study the interaction from the actual polymer/substrate interfacial layer, we prepared nanolayer thin films of aPHB using a 0.003wt% aPHB in a chloroform solution. The film thickness of this nanolayer thin film is estimated to be 1.36 nm. The IRRAS spectra of both aPHB nanolayer and a 40 nm thick aPHB film are displayed in Figure 7.8.

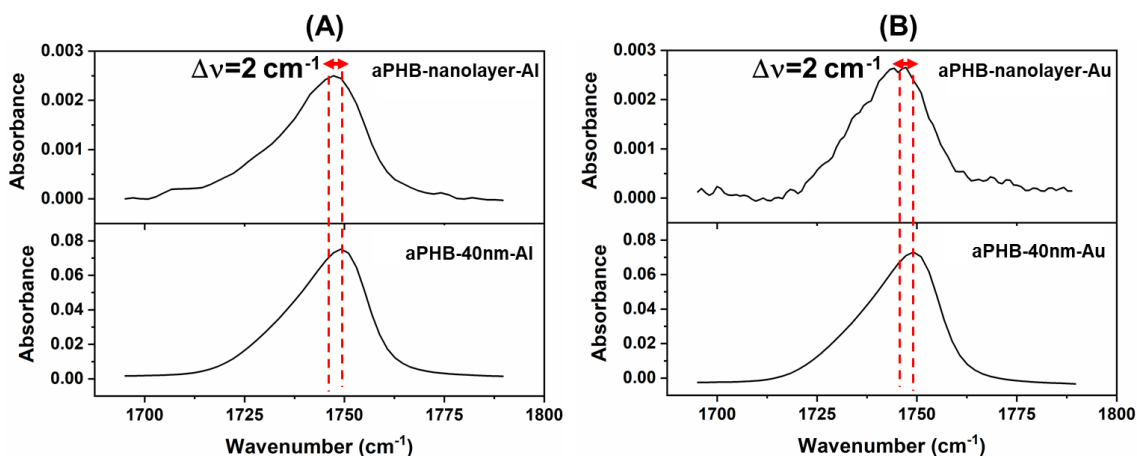


**Figure 7.8: Comparison of IR carbonyl stretching region of atactic PHB (aPHB) nanolayer vs 40 nm layer on aluminum substrate (A), and gold substrate (B).**

We see a  $2 \text{ cm}^{-1}$  red-shift from  $1749 \text{ cm}^{-1}$  to  $1747 \text{ cm}^{-1}$  for the aluminum substrate, but a similar peak displacement was also seen in the gold case, suggesting this slight shift is not limited to Al substrate. Hence, even using a 1.36 nm thick aPHB nanolayer we still did not observe as prominent a red-shift of the carbonyl stretching band as was reported by Brogly et al. (a  $10 \text{ cm}^{-1}$  shift) and Laila et al. (a  $8 \text{ cm}^{-1}$  shift). Therefore, this finding enables us to conclude that it is possible the H-bonding interaction does not exist, or if it does, the interaction might be too subtle to be detected by the IRRAS measurement. In addition, molecular structural differences between PHB or PHBHx and PMMA may also be another reason for the absence of a H-bonding interaction. PHB or PHBHx has ester groups in the backbone, which is different than PMMA and poly(ethylene-*co*-butyl acrylate), where ester groups were located at the side chain. Side-chain ester groups may result in a more effective contact of  $-\text{C}=\text{O}$  with an AO surface to form H-bonds. However, because the

crystallization retardation effect is prominent, we consider that apart from H-bonding interactions, there must be other molecular interactions present that contribute to this crystallization retardation phenomenon.

### 7.3.2 Dipole-dipole interaction between PHB/PHBHx and AO surface

Though no H-bonding was detected, an interaction force, such as a dipole-dipole interaction between an ester group and the AO surface, may also play a critical role. We examined the surface energy of the two substrates. The Owens and Wendt equation was used to extract surface energy components. Measured contact angles are shown in Figure 7.9, and derived surface energy components are listed in Table 7.2.

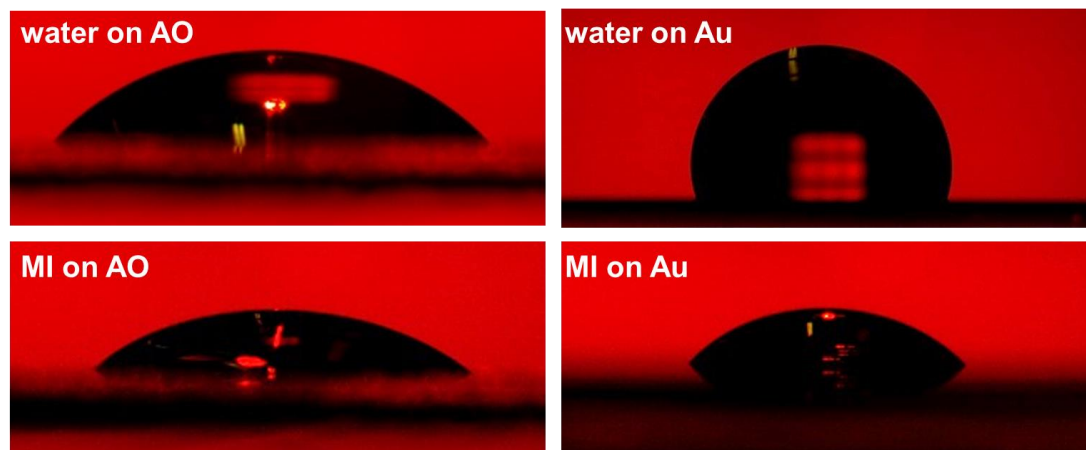


**Figure 7.9: Measured static contact angles of water and methylene iodide on gold and aluminum oxide surfaces.**

**Table 7.2: Calculated surface energy for gold and aluminum oxide (AO) surfaces**

Surface	Measured contact angle (°)		Total surface energy (ergs cm <sup>-2</sup> )	Surface energy composition (ergs cm <sup>-2</sup> )		Dispersive percentage	Polar percentage
	H <sub>2</sub> O	MI		dispersive	polar		
<b>Au</b>	90.3	29.1	44.7	44.2	0.5	98.8%	1.2%
<b>AO</b>	46.0	44.2	55.1	28.8	26.3	52.3%	47.7%

For gold, the dispersive force component dominates whereas for AO around 50% of the polar component contributes to the total surface energy. This finding indicates that AO has a highly polar surface. The crystallization of PHB and PHBHx relies on the intramolecular H-bonds formed between -C=O from one stem and -CH<sub>3</sub> groups from the neighboring stem. If the -C=O instead associates with O-Al-O from AO rather than associating with -CH<sub>3</sub> from the polymers, crystallization may be disrupted. In contrast, as shown in Table 7.2, the gold substrate has a dispersive surface, resulting in a weaker polymer/substrate interaction. Such a dispersive interaction is not expected to disrupt polymer crystallization.

### 7.3.3 The disordered nature of AO surface

We propose that dipole-dipole interactions may not be sufficient to result in such a prominent crystallization retardation effect. In addition, another question that arises is why the AO surface promotes crystallization retardation but not a crystallization enhancement by serving as a nucleating template? We speculate that crystallization retardation or enhancement depends on the degree of order of the

substrate surface. Figure 7.10 shows a high resolution TEM micrograph of an aluminum/aluminum oxide interfacial region.

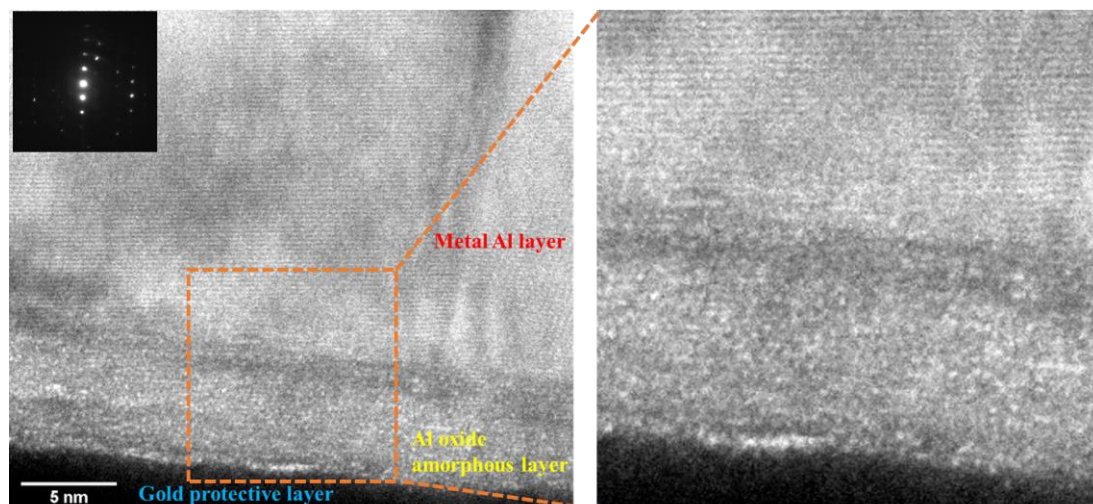


**Figure 7.10: TEM high resolution micrograph of Al/AO cross-section area. Left: overall view of the cross section and diffraction pattern from the metal layer. Right: a zoom-in to show clear lattice imaging.**

One can clearly identify the bulk aluminum metal layer and it is highly crystalline as indicated by the real-space lattice imaging and diffraction pattern. A 5 nm surface oxide layer was observed, which shows no lattice structure indicating it is disordered in nature. It is known that due to a required high activation energy, naturally formed metal oxide remains amorphous in the absence of an annealing treatment at high temperature.<sup>38</sup> The disordered AO surface will not facilitate polymer crystallization due to the absence of available crystalline facets to provide efficient nucleating sites. Instead, once the polymer is melted to form random coils, dipole-dipole interactions between the polymers and the disordered surface structure will

anchor the polymer in a disordered state. The amorphous surface also provides nanoscale holes or sites to trap chain segments to prevent chain movement required for crystallization. The intrinsic stiffness and rigidity of a metal oxide surface will also inhibit chain relaxation. All these factors are present, even after cooling to room temperature (over 100 °C supercooling), indicating that the polymers can still exist in a supercooled amorphous state for an extended time period (over 12 hrs for PHBHx (13mo%)) thereby contributing to the crystallization retardation phenomenon. Although the possibility of H-bond formation cannot be completely ruled out, our data do not show a typical H-bond induced red shift of the carbonyls. Thus, for a first approximation, we attribute the crystallization retardation to the dipole-dipole interaction and the disordered nature of the AO surface.

#### **7.3.4 Effect of the aluminum substrate on the crystal orientation**

Crystal orientation profiles in the films were studied using grazing incident wide angle X-ray diffraction, or GIWAXD, as shown in Figure 7.11.

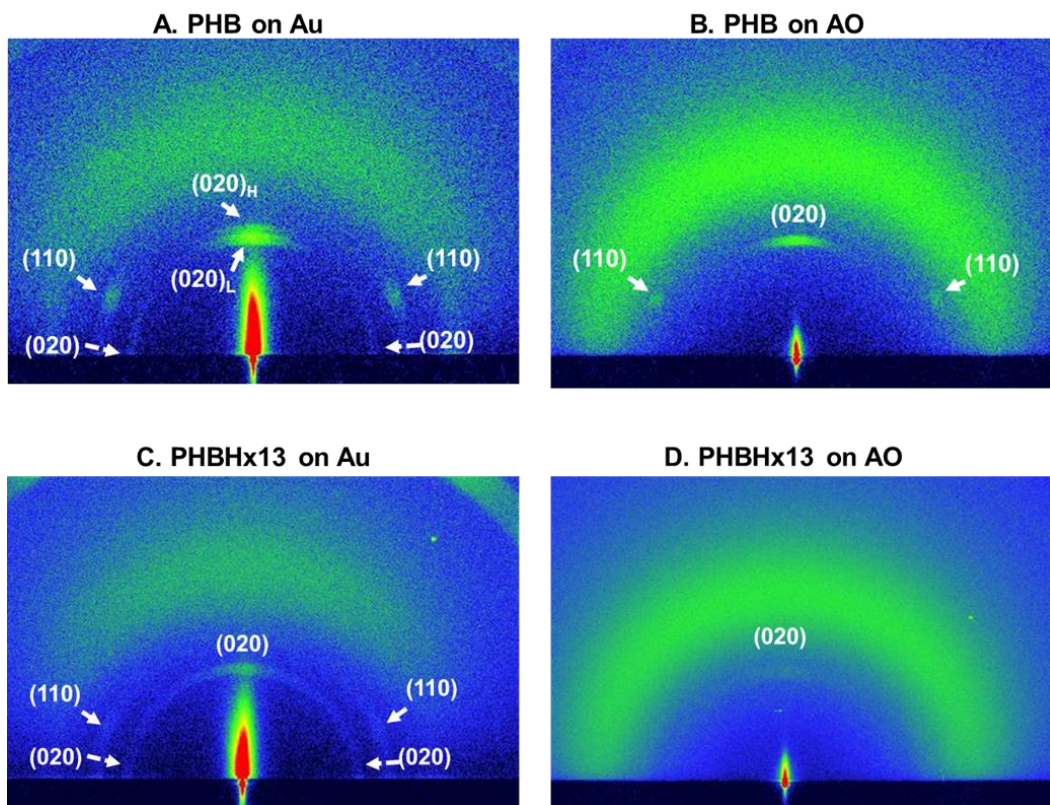


**Figure 7.11: GIWAXD profiles for a PHB crystalline film on gold (A), a PHB crystalline film on AO (B), a PHBHx(13mol%) film on gold (C), and a PHBHx(13mol%) film on AO (D).**

Crystal orientation was also found to have a substrate dependence. All samples used for GIWAXD study were well crystallized at room temperature after five days. The appearance of the (020) reflection along the out-of-plane (perpendicular) direction indicates an edge-on lamellae orientation whereas (020) appearing along the in-plane (horizontal) direction indicates a flat-on lamellar orientation. When crystallizing on gold, the edge-on oriented crystals predominate, but a fair amount of flat-on oriented crystals can also be seen as indicated by a weak (020) reflection along the horizontal direction. In addition, for PHB/Au, along the out-of-plane direction, we see a second

(020) peak, denoted as (020)<sub>H</sub> with a smaller d-spacing (higher reflection angle), suggesting a more perfect alpha crystal. It is most likely that these more perfect crystals were developed during the cooling step. This observation is consistent with IRRAS data and the Avrami analysis. Two d-spacings for the (020) peak were also observed by Khasanah et al.<sup>39</sup> In contrast, on an aluminum substrate, both PHB and PHBHx (13mol%) show only edge-on orientation, and no flat-on orientation was observed. This substrate induced crystal orientation difference will be discussed in a later section. In addition, based on the diffraction pattern observed on either on gold or aluminum, the overall reflection intensity for PHBHx(13ml%) is much weaker than that of PHB due to its intrinsic lower crystallinity.

**Proposed mechanism for edge-on crystal orientation of PHB/PHBHx on aluminum substrate.** A possible explanation for why the crystallites only show edge-on orientation, as indicated by the GIWAXD data in Figure 7.11, on aluminum substrates (or AO) will be discussed. Let us first examine the sample of PHBHx13 on Au (Figure 7.11C) and AO (Figure 7.11D). Both samples have edge-on crystals as indicated by the (020) peak along the perpendicular direction whereas PHBHx13 on Au also has flat-on crystals as indicated by the (020) peak along the horizontal direction. These two samples were both crystallized isothermally at room temperature; therefore, both have the same crystallization temperature profile. Thus, the orientation profile difference is not due to a temperature effect but more likely a substrate effect. Typically, a low crystallization temperature facilitates edge-on crystal formation,<sup>40</sup> and room temperature for PHBHx is a low crystallization temperature. Therefore, the flat-on crystals for PHBHx13 on Au are most likely due to a confinement effect. It is well known that a confinement effect can induce a flat-on crystal orientation.<sup>28</sup> In our case,

the flat-on crystals were most likely developed in the confinement layer of the polymer/Au substrate interface, where the polymer is confined by the bottom substrate. Such confinement-induced flat-on crystals for PHB have been studied extensively by Khasanah et al.<sup>41</sup> In their work, it was found that PHB in the confinement layer tends to form flat-on crystals, whereas polymers near the film surface (polymer/air interface) tend to crystallize into edge-on crystals. The proposed hypothesis for the absence of confinement-induced flat-on crystals for PHBHx13 on AO are shown below in Figure 7.12. On AO, due to a crystallization inhibition effect, the formation of flat-on crystals in the confinement layer is significantly inhibited. In contrast, polymers on the film surface can still crystallize to adopt an edge-on orientation. These early developed edge-on crystals may even induce the confinement layer to adopt the same edge-on orientation, resulting in an edge-on dominated crystal orientation throughout the entire film, as shown in Figure 12. Now let us examine PHB on AO (Figure 7.11B) which was also isothermally crystallized at room temperature. The exclusive edge-on orientation for PHB on AO is believed to be similar to that found for PHBHx13 on AO, i.e., the flat-on crystals in the confinement layer that normally form were inhibited due to the crystallization inhibition effect of AO. For PHB on Au (Figure 7.11A), the flat-on crystals may be caused by a similar confinement induced flat-on orientation as observed for the case of PHBHx13 on Au. A second possibility involves a high temperature induced flat-on orientation. Because PHB crystallizes quickly on Au, although the majority of the crystallization occurs after cooling to room temperature, crystallization may have already begun during the cooling process. This possibility is supported by the observation of a weak intensity peak at  $1230\text{ cm}^{-1}$  in the 2 min IRRAS spectrum shown in Figure 7.3. It is known that

a high crystallization temperature typically facilitates flat-on lamellar orientation.<sup>41</sup> Thus, part of the flat-on crystals may originate from high temperature crystallization.

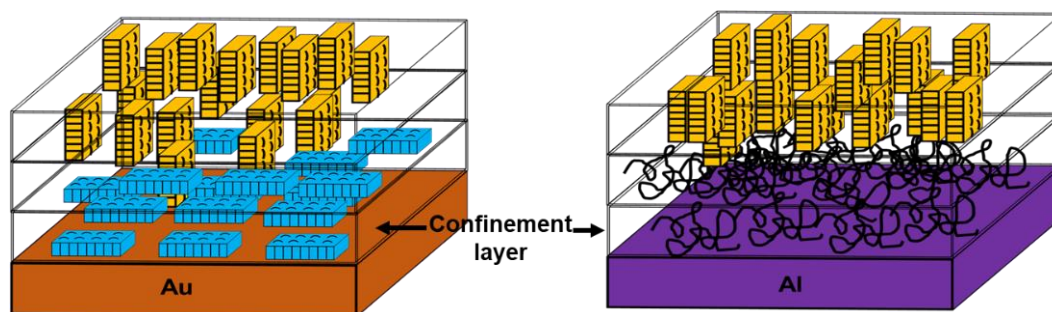


**Figure 7.12: A simplified schematic to illustrate crystal orientation profiles in PHB and PHBHx(13mol%) ultrathin films on gold (left) and aluminum (right). Edge-on crystal (yellow) and flat-on crystal (blue).**

**The scientific insights gained from the current study lies in the following points:**

1). This finding supplements the work done by Napolitano and Wübbenhorst.<sup>35</sup> In their work, Napolitano and Wübbenhorst also reported that PHB ultrathin films sandwiched between two aluminum plates were found not to crystallize. However, the reasons for the inhibition effect remain an open question—“Is it due to a confinement effect or the intrinsic aluminum oxide surface chemistry effect?”. Our result clearly showed that the intrinsic chemistry and disordered structure of the aluminum oxide surface can cause a significant crystallization retardation effect. To our knowledge, this is the first demonstration that an aluminum oxide surface itself, without confinement, can retard crystallization of PHB and PHBHx.

2). It would not be surprising to observe such a crystallization retardation effect if the polymer interacts with the AO surface via strong interactions such as chemical bonds, or strong H-bonds. In our case, however, all the evidence points towards a Van der Waals interaction (the dipole-dipole interaction for PHB/AO), a conventionally weak interaction, together with a disordered surface that can give rise to such a prominent crystallization retardation.

## Chapter 8

### INTERMOLECULAR HYDROGEN BONDING BETWEEN POLY[(R)-3-HYDROXYBUTYRATE] (PHB) AND PSEUDOBOEHMITE AND ITS EFFECT ON CRYSTALLIZATION OF PHB

As shown in Chapter 7, the crystallization retardation of PHB and PHBHx thin films on an AO surface is not caused by an H-bond between -C=O and -OH from the AO surface. In addition, it was found that, after days, even the copolymer PHBHx(13mol%) still slowly crystallizes on the AO surface, suggesting the retardation effect is a kinetic process. The question becomes: “is it possible to introduce chemically bonded -OH species to the AO surface to induce a H-bond between -OH and -C=O to achieve the goal of inhibiting the crystallization of PHB and PHBHx for an extended time?”

#### 8.1 Preparation of a pseudoboehmite surface

To introduce chemically bonded -OH groups onto an AO surface, we followed a modification method reported by J. van den Brand et al.<sup>42</sup> A cleaned aluminum substrate was treated by immersing into a boiling deionized water bath at 100 °C for 1 min. This treatment induces a thick pseudoboehmite layer on the surface. Then the substrate was rapidly taken out of water, and the water residue was removed by a nitrogen flow. Then the substrate was purged under nitrogen for another 30 mins. XPS data on treated surface and untreated AO surface is shown in Figure 8.1.

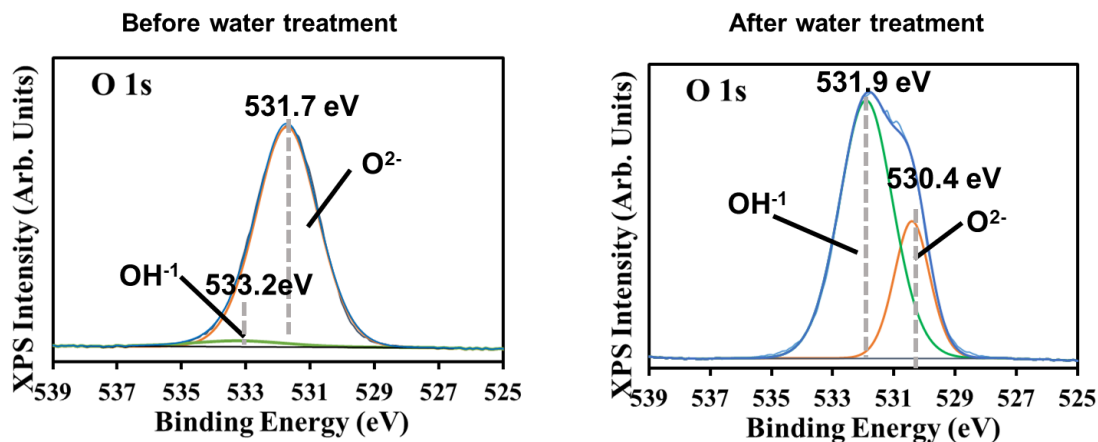


**Figure 8.1: XPS O 1s profiles of AO surface (before water treatment) and PB (after water treatment) surfaces.**

Before treatment, the surface is predominantly comprised of aluminum oxide (AO) as indicated by the peak at 531.7 eV. A small peak at 533.2 eV, resolved by curve fitting, suggests the existence of trace amounts of  $\text{OH}^{-1}$ . After treatment, a strong  $\text{OH}^{-1}$  peak at 531.9 eV appears and the  $\text{O}^{2-}$  shifted to 530.4 eV. The new peak positions for  $\text{OH}^{-1}$  and  $\text{O}^{2-}$  after water treatment agree with those reported for PB.<sup>42</sup> Therefore, water treatment results in a PB surface as expected.

## 8.2 Intermolecular H-bonding of aPHB and PB

To investigate if PHB can H-bond with a pseudoboehmite surface, an atactic PHB (aPHB) ultrathin film (around 40 nm) was spin coated on pseudoboehmite and Al (for comparison) substrates. The use of aPHB is driven by the total absence of crystallization for aPHB. Any observed infrared peak shift at a fixed temperature would therefore be attributed strictly to the interaction of the aPHB with PB. Figure 8.2(A) shows the carbonyl stretching region of IRRAS spectra and peak

decomposition profiles for spin-coated aPHB ultrathin films on AO and PB measured at room temperature (23 °C).

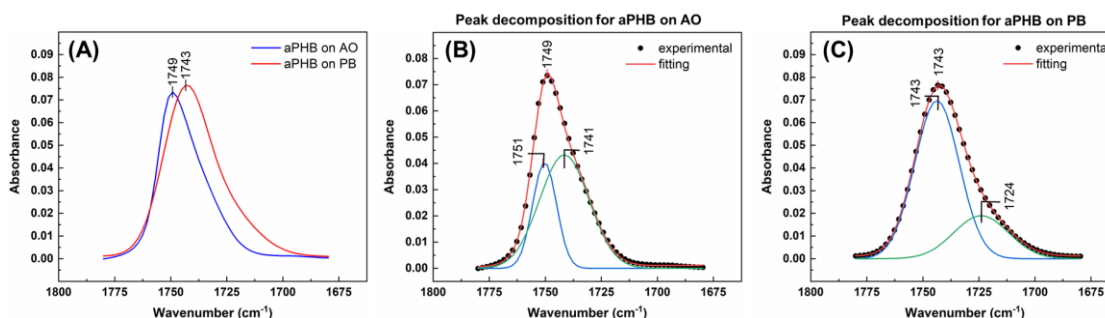


**Figure 8.2: (A) carbonyl stretching region of aPHB ultrathin films on AO and PB. (B) Peak decomposition for aPHB on AO. (C) Peak decomposition for aPHB on PB.**

Figure 8.2(A) shows that aPHB on AO has a peak maximum at  $1749\text{ cm}^{-1}$ , whereas aPHB on PB has the maximum shifted to  $1743\text{ cm}^{-1}$ . We have shown in chapter 7 that naturally oxidized aluminum oxide only interacts with PHB through dipole-dipole interactions leading to little ( $2\text{ cm}^{-1}$ ) or no shift in the carbonyl frequency. Therefore, the currently observed shift of  $6\text{ cm}^{-1}$  for aPHB on PB suggests an intermolecular H-bonding network formed between the  $\text{-C=O}$  of aPHB and  $\text{-OH}$  of PB.

Due to the asymmetric and broad nature of the peaks, peak decomposition (Gaussian fitting) was performed, as shown in Figure 8.2(B) and 8.2(C). For aPHB on AO in Figure 8.2(B), two peaks located at  $1741\text{ cm}^{-1}$  and  $1751\text{ cm}^{-1}$  can be resolved, possibly indicating two amorphous components are present in the film. Multiple amorphous carbonyl components have been recently observed for PHB ultrathin

films.<sup>39</sup> It is most likely that the high-wavenumber peak,  $1751\text{ cm}^{-1}$ , originates from the more flexible polymer chains near the polymer/air interface, whereas the dominant  $1741\text{ cm}^{-1}$  peak may originate from polymer chains in bulk (or away from polymer/air interface). For aPHB on PB (Figure 8.2(C)), peak decomposition gives rise to two peaks at  $1743\text{ cm}^{-1}$  and  $1724\text{ cm}^{-1}$ . Interestingly,  $1724\text{ cm}^{-1}$  is typically treated as an indicator of the  $\alpha$  crystalline form in iPHB.<sup>25</sup> However, in the current case, since aPHB is not able to crystallize, the peak of  $1724\text{ cm}^{-1}$  must originate from the intermolecular H-bonding occurring between the  $\text{-C=O}$  from aPHB and  $\text{-OH}$  from PB. In addition, the  $1743\text{ cm}^{-1}$  peak can be assigned to an amorphous component.

The observed intermolecular H-bonding interaction should be mostly from the polymer/substrate interfacial region, which is approximately several angstroms thick. The as-cast film is around 40 nm thick. If the upper-layer polymers can be removed, we should expect a rise of the carbonyl stretching peak at  $1724\text{ cm}^{-1}$ . To test this hypothesis, the as-cast film was immersed in chloroform (a good solvent for PHB) to remove upper-layer polymers. Figure 8.3(A) shows the trending of the carbonyl stretching peak as a function of immersion time. First, the peak intensity decreases with increasing immersion time, indicating the polymers originally in the film were gradually dissolved in chloroform. Second, the peak maximum shifts to a lower wavenumber with increasing immersion time. Figure 8.3(B) more clearly shows the plots of wavenumber shift and film thickness changes (derived from absorbance based on Beer-Lambert law) as a function of immersion time. The carbonyl peak maximum shifted from  $1743\text{ cm}^{-1}$  to  $1730\text{ cm}^{-1}$ . The film thickness decreases rapidly at the beginning and then slowly after 20 mins. This observation indicates the polymer layer near the polymer/substrate interface is more difficult to be removed, which is possibly

due to the H-bonding association between aPHB and PB near the polymer/substrate interface.

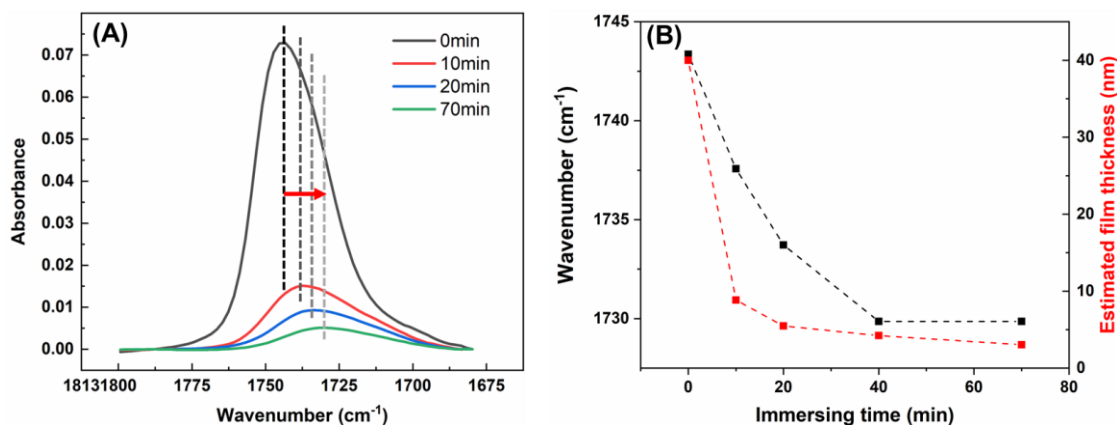


**Figure 8.3: (A) carbonyl stretching region of aPHB on AO with immersing time at 0, 10, 20, and 70 mins in chloroform (B) Plots of wavenumber shift and the estimated film thickness as a function of immersing time.**

Peak decomposition was performed for the spectra in Figure 8.3(A) (immersion time 10, 20, and 70 mins). The decomposed peaks were shown in Figure 8.4. The peak integrated area of 1724  $\text{cm}^{-1}$  (10 mins) or 1722  $\text{cm}^{-1}$  (20 mins and 70 mins), i.e., the intermolecular H-bonding peak, increases with immersion time. Therefore, we confirmed that a H-bond exists between the  $-\text{C}=\text{O}$  of aPHB and  $-\text{OH}$  of PB surface, and such interaction is located in the interface.

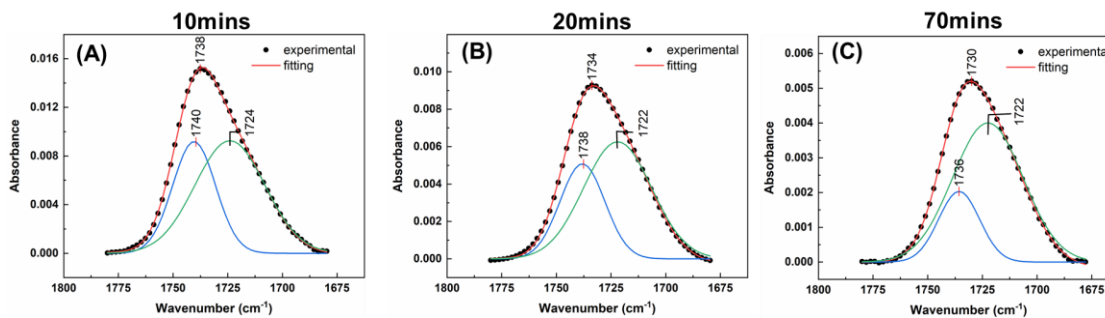


**Figure 8.4: Peak decomposition for carbonyl stretching region of aPHB films on PB at immersing times of 10 mins(A), 20 mins(B), and 70 mins(C).**

### 8.3 Intermolecular H-bonding of isotactic PHB (iPHB) with PB

That aPHB was found H-bonded with PB does not necessarily imply that iPHB can also form H-bonds with PB, because the H-bonding interaction may be tacticity dependent.<sup>37,43</sup> Thus, it is worth examining if iPHB can form similar H-bonding with PB. To remove the solvent effect during spin coating, the as-spun coated iPHB film was first melted, then allowed to cool down to room temperature. The whole processing procedure is shown in Figure 8.5. An iPHB film was also coated on Al substrate for comparison.

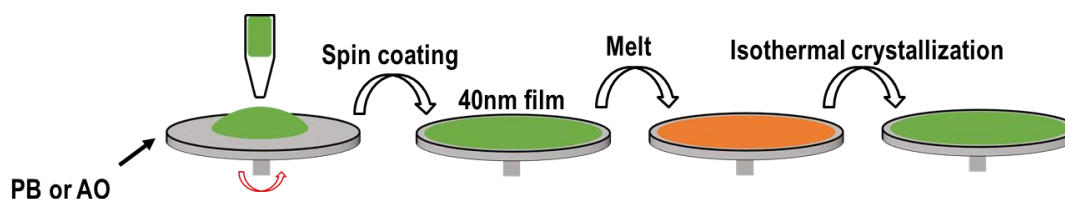


**Figure 8.5: Schematic processing procedures from spin coating to melt crystallization.**

Our preliminary results show that within several minutes after melting, though the sample has been cooled down to room temperature (23 °C), iPHB has not started crystallizing yet, leading to iPHB being in a supercooled amorphous state. Figure 8.6 shows that supercooled iPHB on AO has a peak maximum at 1750  $\text{cm}^{-1}$  and supercooled iPHB on PB has a maximum at 1744  $\text{cm}^{-1}$ . This PB induced red-shift for the case of iPHB is similar to that for aPHB. Figure 8.7(A) shows the decomposition profiles of the two spectra in Figure 8.6. For iPHB on AO, two peaks of 1752  $\text{cm}^{-1}$  and 1741  $\text{cm}^{-1}$  can be resolved, which are similar to those found in the case of aPHB on AO. For iPHB on PB, the peak can be decomposed into three individual peaks located at 1748, 1740, and 1724  $\text{cm}^{-1}$ . The observation of a 1724  $\text{cm}^{-1}$  peak indicates iPHB can form H-bonds with PB in a similar way as that for aPHB.

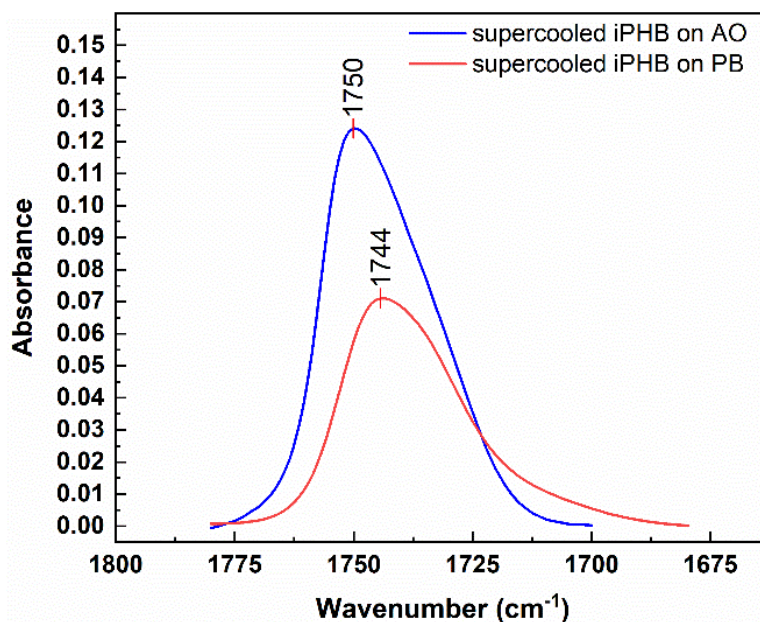


**Figure 8.6: Carbonyl stretching region for supercooled amorphous iPHB on AO and PB (2mins after melt)**

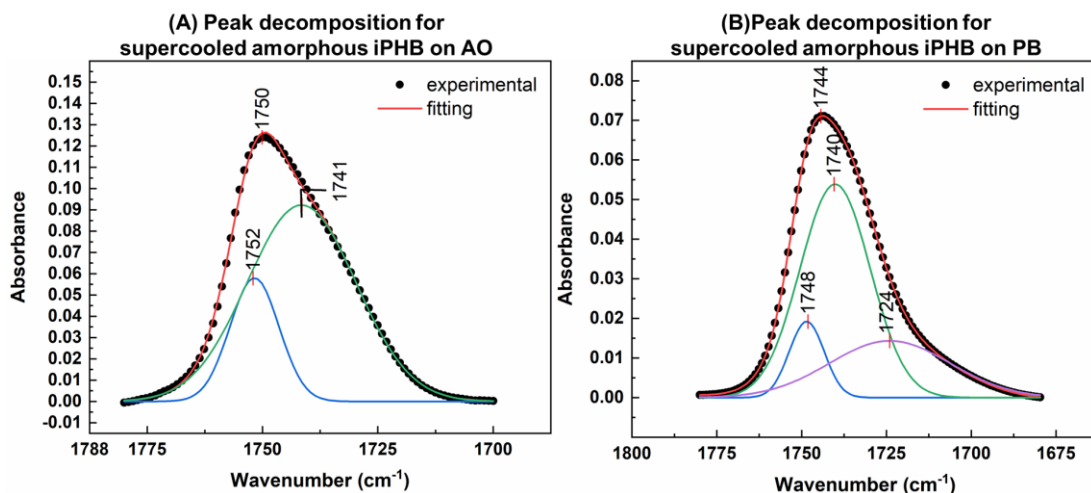


**Figure 8.7: (A) Peak decomposition for the supercooled amorphous iPHB film on AO. (B) Peak decomposition for the supercooled amorphous iPHB film on PB**

#### 8.4 Effects of intermolecular H-bonding on the crystallization behavior of PHB

At 23 °C, the supercooled amorphous iPHB on both AO and PB surfaces will finally crystallize but have different crystallinity profiles. Figure 8.8 shows the carbonyl regions for iPHB on AO and PB after a 10-day crystallization at room temperature. The carbonyl peak of iPHB on AO can be decomposed to 1746, 1736, and 1726  $\text{cm}^{-1}$ . Since iPHB cannot form H-bonds with AO, the development of a band at 1726  $\text{cm}^{-1}$  must be arising from  $\alpha$  crystallization of iPHB. For the case of iPHB on PB, as shown in Figure 8.8(B), four peaks located at 1749, 1740, 1726, and 1724  $\text{cm}^{-1}$  can be resolved. The preservation of 1724  $\text{cm}^{-1}$  indicates the intermolecular H-bonding interaction still exists even after crystallization. The peak of 1726  $\text{cm}^{-1}$  is from  $\alpha$  crystallization. The integrated area of the peak 1726  $\text{cm}^{-1}$  is significantly decreased for

iPHB on PB compared with iPHB on AO, suggesting an evident crystallinity drop. The crystallinity reduction may be caused by two reasons: (1) 3-hydroxybutyrate monomers directly involved in H-bonding formation with PB cannot crystallize (2) because the H-bonded monomers are anchored by the substrate, those free monomers between these H-bonded ones along the same PHB chain may also not be able to crystallize due to a reduced mobility.

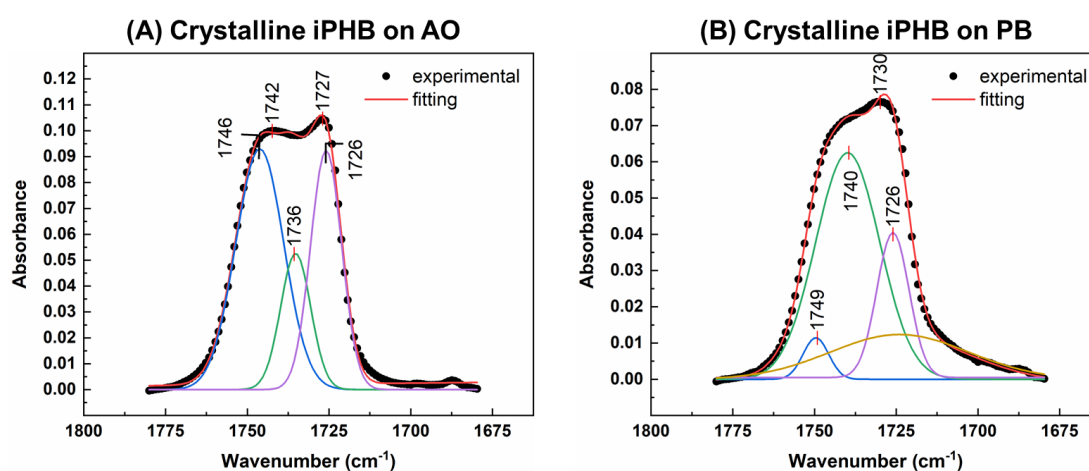


**Figure 8.8: (A) Peak decomposition of carbonyl stretching region for iPHB on AO after 10-day crystallization at 23 C. (B) Peak decomposition of carbonyl stretching region for iPHB on PB after 10-day crystallization at 23 C.**

In addition, the effect of intermolecular H-bonding on crystallinity and crystal orientation profiles of iPHB film was also examined using GIWAXD and polarized optical microscopy (POM). Figure 8.9 shows the diffraction patterns for iPHB on AO and PB after a 10-day crystallization. For iPHB on AO, the reflection along the

vertical direction can be assigned to the (020) planes for the  $\alpha$  crystalline phase, and the other two lateral reflections can be indexed with (110). The diffraction pattern is very similar to the electron diffraction pattern of solution grown iPHB lamellar crystals examined using TEM.<sup>44</sup> This result indicates the majority of crystallites are edge-on orientated with the  $b$ -axis parallel to the vertical direction.

In contrast, crystallized iPHB on PB (Figure 8.9(B)), shows a (020) diffraction ring with a very low intensity (barely seen in the 2D profile). The weak intensity indicates a crystallinity drop and the ring-shaped diffraction pattern indicates the crystallites are randomly oriented. For better visualization, 1D profiles were displayed in Figure 8(C). One can see that iPHB on PB shows a much broader and weaker peak compared with iPHB on AO surface. The peak broadening could be due to the effect of a smaller crystallite size for iPHB on PB or an overall low crystallinity. Figure 8.10 shows the POM images for the two samples. Two-dimensional spherulites can be seen for crystallized iPHB on AO, whereas no crystalline morphology is detected for crystallized iPHB on PB.

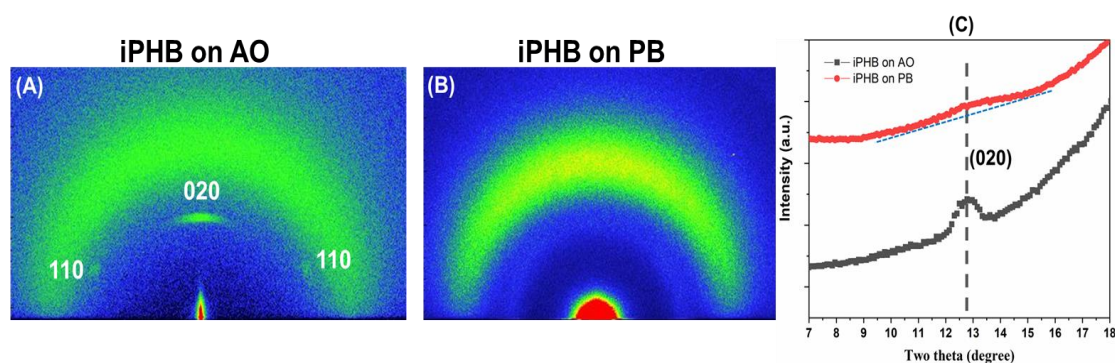


**Figure 8.9:** (A) GIWAXD profile for iPHB on AO after 10-day crystallization at 23 C. (B) GIWAXS profile for iPHB on PB after 10-day crystallization at 23 C. (C) 1D profiles of iPHB on AO *versus* on PB. The broad peak at a high angle is from scattering from glass substrates

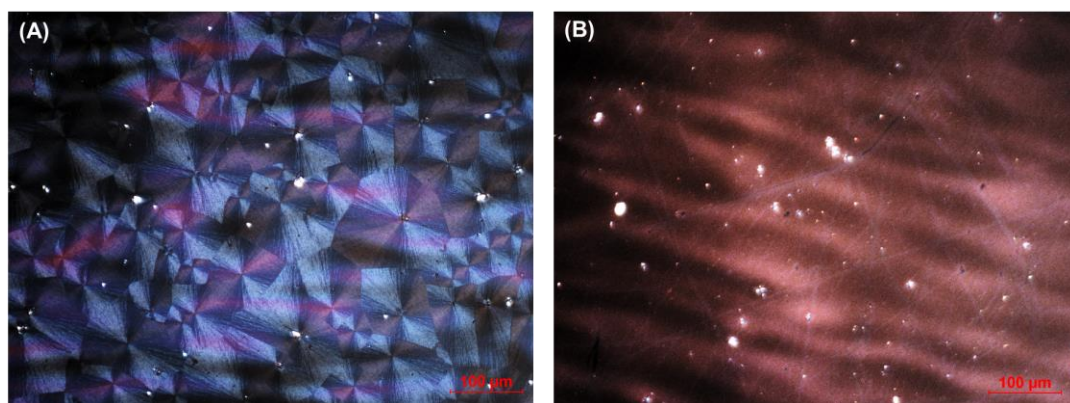


**Figure 8.10:** POM images of crystalline iPHB on AO (A) and PB (B).

It is seen that the intermolecular H-bonding between iPHB and PB can effectively lower the crystallinity of the PHB over a relatively long time (10 days) compared with the AO case. In addition, the  $1724\text{ cm}^{-1}$  peak, indicative of the

intermolecular H-bonding is preserved even after crystallization. These observations suggest the H-bonds formed for iPHB on PB are markedly stable.

We can compare two values to approximately understand why the H-bonds between PB and PHB can inhibit PHB crystallization in an extended time: the H-bonding formation enthalpy and crystallization enthalpy of iPHB. The H-bonding enthalpy  $\Delta H^{AB}$  for polyesters (Lewis base) associated with Lewis acids can be estimated using the relationship  $\Delta H^{AB} = -k^{AB} \Delta \nu^{AB}$ , where  $k^{AB} = 0.99$  kJ/mol,  $\Delta \nu^{AB}$  is the wavenumber shift of carbonyl stretching frequency from amorphous state.<sup>37,45</sup> In the current case, if the frequency of amorphous carbonyl for iPHB is taken as  $1740$   $\text{cm}^{-1}$ , then the H-bonding enthalpy is estimated as  $15.8$  kJ/mol, which is slightly higher than the  $\alpha$  crystallization enthalpy of iPHB, which is  $12.5$  kJ/mol as reported by Sato et al..<sup>25</sup> A higher bonding energy suggests PHB tends to H-bond with -OH from PB instead of self-association to crystallize. This tendency may be considered as the reason why the H-bonding peak  $1724$   $\text{cm}^{-1}$  does not disappear even after 10 days. Because the H-bonding mainly arise from the interfacial region, polymers near film surface is less affected by H-bonding so that they can still crystallize. This mechanism explains why we can still observe a low level of crystallinity as indicated by IR and XRD data.

## Chapter 9

### FUTURE DIRECTIONS AND RECOMMENDATIONS

In this chapter, we comment on the results described earlier and provide suggestions on potential continuation of current projects. Future research directions on PHBHx which may be different than those described here will be also discussed.

#### 9.1 Comments on the special interaction of $-\text{CH}\cdots\text{O}=\text{C}$ in PHBHx alpha crystal structure

In the single crystal study, we observed a unique, highly anisotropic needle shaped single crystal growth pattern for PHBHx. This anisotropic growth behavior of PHBHx differs from single crystals of other polyesters such as PLLA and PCL, which have a more symmetric single crystal growth pattern.<sup>46,47</sup> The growth directionality naturally led us to consider an underlying molecular interaction with a directional nature which could dictate the crystal growth direction. IR studies on PHBHx single crystals detected a blue shift of the  $-\text{CH}$  asymmetric stretching band located at  $3009\text{ cm}^{-1}$ . Previously, Sato et al.<sup>25</sup> for the first time, observed such a blue shift in the homopolymer PHB. It is proposed that this blue shift was due to an unconventional weak H-bonding interaction between one hydrogen atom of  $-\text{CH}_3$  and the oxygen of  $\text{O}=\text{C}$ . We analyzed the weak H-bonding packing in the crystal structure and found that the major component of  $-\text{CH}\cdots\text{O}=\text{C}$  was indeed parallel with the dominant crystal growth direction. Since it is known that H-bonding is directional in nature, we suspected that the growth directionality of PHBHx single crystal may be dictated by this weak H-bonding interaction.

However, it is worth clarifying that crystallization is a cooperative process which involves many different molecular interactions. Attributing a crystallization driving force to a single interaction is risky. Normally, in a crystal lattice, there are some molecular interaction that increase the energy locally, but also some molecular interactions that decrease energy elsewhere. It is the total sum of these energy changes that governs the crystallization process. This awareness leads us to ask the question: “Does the weak H-bonding itself help stabilize the crystal structure, or is this observed blue-shift associated with the so-called weak “H-bonding” actually forced to form as a result of crystallization?” If the former is correct, why would we observe a blue shift? If the latter is true, then the crystallization may not be driven by the  $\text{-CH}\cdots\text{O}=\text{C}$  interaction at all. The purpose of the current discussion is not to prove which standpoint is correct, but to call for caution from future researchers working in this area, and to provide constructive technical viewpoints.

We first show an example of how the interaction pair  $\text{-CH}\cdots\text{O}=\text{C}$  with a blue shifted C-H can help stabilize a crystal lattice. Takanori et al. studied the conformational stability of 1-methoxy-2-(methylthio)ethane, or MMTE.<sup>48</sup> The molecular structure of MMTE is shown in Figure 9.1. Atoms along the backbone are indexed from right to left.

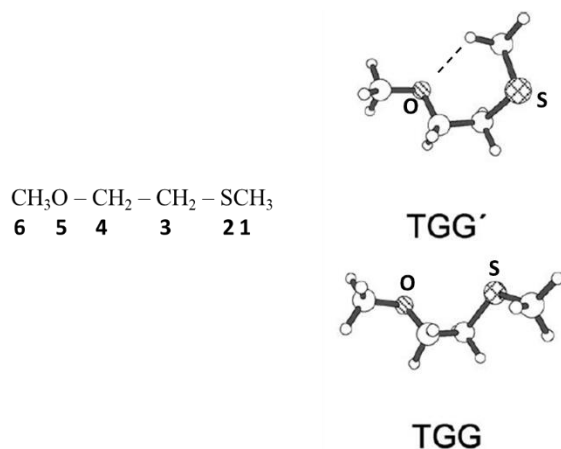


**Figure 9.1: Molecular structure of 1-methoxy-2-(methylthio)ethane and two conformers.**

The conformation of the MMTE using T for trans, G for *gauche*<sup>±</sup> and G' for *gauche*<sup>∓</sup> for a sequence of the three bonds CH<sub>3</sub>O–CH<sub>2</sub>–CH<sub>2</sub>–SCH<sub>3</sub> from the left to the right. The two conformers, TGG' and TGG are shown in Figure 9.1. For the TGG' conformer, there is a 1,5-CH···O interaction involved. The energy of TGG' is calculated to be 4 kJ/mol less than that of TGG, indicating that TGG' is more energetically stable than TGG. Geometrically, the calculation showed that the C-H bond length involved in the 1,5-CH···O interaction in TGG' is shortened by 0.003–0.004 Å compared with that in TGG. In addition, a blue shift of the stretching frequency of the C-H was observed. This study is based on an isolated single molecule, so that there is no interference from crystallization. Therefore, this study provides a solid argument that a -CH···O=C interaction with a blue shifted C-H indeed can stabilize molecular structure. Detailed studies can be found in the original paper.<sup>48</sup>

A fundamental explanation for the blue shift can be found in the review paper by Pavel and Zdeněk.<sup>49</sup> The natural bond orbital (NBO) analysis was used in the paper

to evaluate charge transfer. If an H donor and acceptor pair is represented by  $X_3C-H\cdots Y$  (X and Y represent arbitrary atoms, C represents carbon atom, and H represents hydrogen atom), the result showed that for a standard H-bonding system, the charge transfer from H acceptor “Y” dominantly goes to the C-H bond, resulting in an elongation of this bond and consequently leading to a red shift in the C-H stretching frequency. For the case of a weak H-bonding system, the dominating charge acceptor is the far end bond of X-C instead of C-H bond, leading to an elongation of the X-C bond. The X-C bond elongation triggers a secondary rearrangement, making the C-H bond shortened, giving rise to a blue shift of C-H.

This proposed mechanism by Pavel and Zdeněk at least provides a theoretical criterion to evaluate if the  $CH\cdots O$  interaction present in PHBHx crystal lattice drives real blue shift H-bonding or not. Based on the charge transfer theory, we can examine the variation of the C-CH<sub>3</sub> bond length of PHB before and after crystallization. This study necessarily requires simulation as a technical support. Ideally, if the calculation shows an elongation of C-CH<sub>3</sub> bond after crystallization, it is highly possible the  $CH\cdots O$  interaction is indeed a weak, which helps stabilize the crystal structure. If there is no C-CH<sub>3</sub> bond elongation, then it is possible that the C-H bond is forced to be shortened because of crystallization and the current weak H-bonding concept in the alpha crystal structure of PHBHx may be fundamentally incorrect.

## 9.2 Other directions

An obvious future direction for PHBHx would be developing novel processing methods to generate the beta form of PHBHx, which shows unique piezoelectric properties. Generating PHBHx beta form remains a technical challenge. So far, only electrospinning has proven to be able to generate the beta form. The beta form of

PVDF may potentially be used as a substrate material to epitaxially induce the beta form of PHBHx. One recommendation would be to first generate a PVDF single crystal with pure beta form. This may increase the possibility of inducing PHBHx beta form crystals. Another research direction involves using film stretching techniques to generate the beta form of PHBHx. Film stretching is more easily transferred to the commercial environment. A two-step film stretching technique has been successfully applied to generate beta form crystals for PHB.<sup>50</sup> Hence, a modified two-step film stretching method could be used to stretch PHBHx films to see if the beta form develops. Another important topic for future investigation is the application of high-pressure to PHBHx copolymers in order to determine its effect on the presence of different crystalline polymorphs.

## REFERENCES

- (1) Gandini, A. Polymers from Renewable Resources: A Challenge for the Future of Macromolecular Materials. *Macromolecules* **2008**, *41* (24), 9491–9504. <https://doi.org/10.1021/ma801735u>.
- (2) Zhu, Y.; Romain, C.; Williams, C. K. Sustainable Polymers from Renewable Resources. *Nature* **2016**, *540* (7633), 354–362. <https://doi.org/10.1038/nature21001>.
- (3) Philip, S.; Keshavarz, T.; Roy, I. Polyhydroxyalkanoates: Biodegradable Polymers with a Range of Applications. *J. Chem. Technol. Biotechnol.* **2007**, *82* (3), 233–247. <https://doi.org/10.1002/jctb.1667>.
- (4) Poly- $\beta$ -hydroxybutyrate Metabolism in Washed Suspensions of *Bacillus cereus* and *Bacillus megaterium* | Microbiology Society <https://www.microbiologyresearch.org/content/journal/micro/10.1099/00221287-19-1-210> (accessed Nov 12, 2019).
- (5) Noda, I.; Lindsey, S. B.; Caraway, D. Nodax™ Class PHA Copolymers: Their Properties and Applications. In *Plastics from Bacteria: Natural Functions and Applications*; Chen, G. G.-Q., Ed.; Microbiology Monographs; Springer Berlin Heidelberg: Berlin, Heidelberg, 2010; pp 237–255. [https://doi.org/10.1007/978-3-642-03287-5\\_10](https://doi.org/10.1007/978-3-642-03287-5_10).
- (6) Kawai, T.; Ujihara, K.; Maeda, H. Fold Structure of Solution Grown Crystals of Alkyl-Branched Copolymers of Polyethylene. *Makromol. Chem.* **1970**, *132* (1), 87–111. <https://doi.org/10.1002/macp.1970.021320108>.
- (7) Swan, P. R. Polyethylene Unit Cell Variations with Branching. *J. Polym. Sci.* **1962**, *56* (164), 409–416. <https://doi.org/10.1002/pol.1962.1205616411>.
- (8) Hoffman, J. D. Polymer Single Crystals. Philip H. Geil. Interscience (Wiley), New York, 1963. Xii + 560 Pp. Illus. \$16. *Science* **1964**, *143* (3602), 121–121. <https://doi.org/10.1126/science.143.3602.121>.
- (9) Agbolaghi, S.; Abbaspoor, S.; Abbasi, F. A Comprehensive Review on Polymer Single Crystals—From Fundamental Concepts to Applications. *Prog. Polym. Sci.* **2018**, *81*, 22–79. <https://doi.org/10.1016/j.progpolymsci.2017.11.006>.
- (10) Lotz, B.; Miyoshi, T.; Cheng, S. Z. D. *50th Anniversary Perspective* : Polymer Crystals and Crystallization: Personal Journeys in a Challenging Research Field. *Macromolecules* **2017**, *50* (16), 5995–6025. <https://doi.org/10.1021/acs.macromol.7b00907>.

- (11) Two-Dimensional Folded Chain Crystals of a Synthetic Polymer in a Langmuir–Blodgett Film <https://pubs.acs.org/doi/pdf/10.1021/ja050457e> (accessed Nov 12, 2019). <https://doi.org/10.1021/ja050457e>.
- (12) Iijima, S.; Yumura, T.; Liu, Z. One-Dimensional Nanowires of Pseudoboehmite (Aluminum Oxyhydroxide  $\gamma$ -AlOOH). *Proc. Natl. Acad. Sci.* **2016**, *113* (42), 11759–11764. <https://doi.org/10.1073/pnas.1614059113>.
- (13) Electrospray ion-trap multistage mass spectrometry for characterisation of co-monomer compositional distribution of bacterial poly(3-hydroxybutyrate-co-3-hydroxyhexanoate) at the molecular level - Adamus - 2003 - Rapid Communications in Mass Spectrometry - Wiley Online Library [https://onlinelibrary.wiley.com/doi/full/10.1002/rcm.1190?casa\\_token=pykv3005n24AAAAA%3AJ7ECtTiSnjMsK1H2dKLPau7QxtbyAhbk6Q2Th-JAO2b6ZbcAJdA-DZ6EQIWQymj2SeEB2wJodVKfG88](https://onlinelibrary.wiley.com/doi/full/10.1002/rcm.1190?casa_token=pykv3005n24AAAAA%3AJ7ECtTiSnjMsK1H2dKLPau7QxtbyAhbk6Q2Th-JAO2b6ZbcAJdA-DZ6EQIWQymj2SeEB2wJodVKfG88) (accessed Nov 12, 2019).
- (14) Greenler, R. G. Infrared Study of Adsorbed Molecules on Metal Surfaces by Reflection Techniques. *J. Chem. Phys.* **1966**, *44* (1), 310–315. <https://doi.org/10.1063/1.1726462>.
- (15) Sawayanagi, T.; Tanaka, T.; Iwata, T.; Abe, H.; Doi, Y.; Ito, K.; Fujisawa, T.; Fujita, M. Real-Time Synchrotron SAXS and WAXD Studies on Annealing Behavior of Poly[(R)-3-Hydroxybutyrate] Single Crystals. *Macromolecules* **2006**, *39* (6), 2201–2208. <https://doi.org/10.1021/ma052425h>.
- (16) Desiraju, G. R.; Steiner, T. *The Weak Hydrogen Bond: In Structural Chemistry and Biology*; Oxford University Press, 2001.
- (17) Wang, H.; Tashiro, K. Reinvestigation of Crystal Structure and Intermolecular Interactions of Biodegradable Poly(3-Hydroxybutyrate)  $\alpha$ -Form and the Prediction of Its Mechanical Property. *Macromolecules* **2016**, *49* (2), 581–594. <https://doi.org/10.1021/acs.macromol.5b02310>.
- (18) Kumar, S.; Adams, W. W. Electron Beam Damage in High Temperature Polymers. *Polymer* **1990**, *31* (1), 15–19. [https://doi.org/10.1016/0032-3861\(90\)90341-U](https://doi.org/10.1016/0032-3861(90)90341-U).
- (19) Direct AFM Observation of Crystal Twisting and Organization in Banded Spherulites of Chiral Poly(3-hydroxybutyrate-co-3-hydroxyhexanoate) <https://pubs.acs.org/doi/pdf/10.1021/ma0499122> (accessed Nov 12, 2019). <https://doi.org/10.1021/ma0499122>.
- (20) Fukada, E.; Ando, Y. Bending Piezoelectricity in a Microbially Produced Poly- $\beta$ -Hydroxybutyrate. *Biorheology* **1988**, *25* (1–2), 297–302. <https://doi.org/10.3233/BIR-1988-251-239>.
- (21) Ando, Y.; Fukada, E. Piezoelectric Properties and Molecular Motion of Poly( $\beta$ -Hydroxybutyrate) Films. *J. Polym. Sci. Polym. Phys. Ed.* **1984**, *22* (10), 1821–1834. <https://doi.org/10.1002/pol.1984.180221010>.
- (22) Fukada, E.; Ando, Y. Piezoelectric Properties of Poly- $\beta$ -Hydroxybutyrate and Copolymers of  $\beta$ -Hydroxybutyrate and  $\beta$ -Hydroxyvalerate. *Int. J. Biol.*

- Macromol.* **1986**, 8 (6), 361–366. [https://doi.org/10.1016/0141-8130\(86\)90056-5](https://doi.org/10.1016/0141-8130(86)90056-5).
- (23) Mamat, M. R. Z.; Ariffin, H.; Hassan, M. A.; Mohd Zahari, M. A. K. Bio-Based Production of Crotonic Acid by Pyrolysis of Poly(3-Hydroxybutyrate) Inclusions. *J. Clean. Prod.* **2014**, 83, 463–472. <https://doi.org/10.1016/j.jclepro.2014.07.064>.
- (24) Kopinke, F.-D.; Remmler, M.; Mackenzie, K. Thermal Decomposition of Biodegradable Polyesters—I: Poly( $\beta$ -Hydroxybutyric Acid). *Polym. Degrad. Stab.* **1996**, 52 (1), 25–38. [https://doi.org/10.1016/0141-3910\(95\)00221-9](https://doi.org/10.1016/0141-3910(95)00221-9).
- (25) Sato, H.; Murakami, R.; Padermshoke, A.; Hirose, F.; Senda, K.; Noda, I.; Ozaki, Y. Infrared Spectroscopy Studies of CH $\cdots$ O Hydrogen Bondings and Thermal Behavior of Biodegradable Poly(Hydroxyalkanoate). *Macromolecules* **2004**, 37 (19), 7203–7213. <https://doi.org/10.1021/ma049117o>.
- (26) Noda, I.; Dowrey, A. E.; Haynes, J. L.; Marcott, C. Group Frequency Assignments for Major Infrared Bands Observed in Common Synthetic Polymers. In *Physical Properties of Polymers Handbook*; Mark, J. E., Ed.; Springer New York: New York, NY, 2007; pp 395–406. [https://doi.org/10.1007/978-0-387-69002-5\\_22](https://doi.org/10.1007/978-0-387-69002-5_22).
- (27) Owens, D. K.; Wendt, R. C. Estimation of the Surface Free Energy of Polymers. *J. Appl. Polym. Sci.* **1969**, 13 (8), 1741–1747. <https://doi.org/10.1002/app.1969.070130815>.
- (28) Wang, H.; Keum, J. K.; Hiltner, A.; Baer, E.; Freeman, B.; Rozanski, A.; Galeski, A. Confined Crystallization of Polyethylene Oxide in Nanolayer Assemblies. *Science* **2009**, 323 (5915), 757–760. <https://doi.org/10.1126/science.1164601>.
- (29) Wang, H.; Keum, J. K.; Hiltner, A.; Baer, E. Crystallization Kinetics of Poly(Ethylene Oxide) in Confined Nanolayers. *Macromolecules* **2010**, 43 (7), 3359–3364. <https://doi.org/10.1021/ma902780p>.
- (30) Ponting, M.; Lin, Y.; Keum, J. K.; Hiltner, A.; Baer, E. Effect of Substrate on the Isothermal Crystallization Kinetics of Confined Poly( $\epsilon$ -Caprolactone) Nanolayers. *Macromolecules* **2010**, 43 (20), 8619–8627. <https://doi.org/10.1021/ma101625h>.
- (31) Avrami, M. Kinetics of Phase Change. I General Theory. *J. Chem. Phys.* **1939**, 7 (12), 1103–1112. <https://doi.org/10.1063/1.1750380>.
- (32) Choi, H. W.; Kim, Y. H.; Rim, Y. H.; Yang, Y. S. Crystallization Kinetics of Lithium Niobate Glass: Determination of the Johnson–Mehl–Avrami–Kolmogorov Parameters. *Phys. Chem. Chem. Phys.* **2013**, 15 (24), 9940. <https://doi.org/10.1039/c3cp50909e>.
- (33) Dai, X.; Li, H.; Ren, Z.; Russell, T. P.; Yan, S.; Sun, X. Confinement Effects on the Crystallization of Poly(3-Hydroxybutyrate). *Macromolecules* **2018**, 51 (15), 5732–5741. <https://doi.org/10.1021/acs.macromol.8b01083>.
- (34) An, Y.; Dong, L.; Mo, Z.; Liu, T.; Feng, Z. Nonisothermal Crystallization Kinetics of Poly (  $\beta$ -Hydroxybutyrate ). 8.

- (35) Napolitano, S.; Wübbenhorst, M. Slowing Down of the Crystallization Kinetics in Ultrathin Polymer Films: A Size or an Interface Effect? *Macromolecules* **2006**, *39* (18), 5967–5970. <https://doi.org/10.1021/ma061304u>.
- (36) Ulrén, L.; Hjertberg, T.; Ishida, H. An FT-IR Study on Interfacial Interactions in Ethylene Copolymers/Aluminium Laminates in Relation to Adhesion Properties. *J. Adhes.* **1990**, *31* (2–4), 117–136. <https://doi.org/10.1080/00218469008048220>.
- (37) Brogly, M.; Grohens, Y.; Labbe, C.; Schultz, J. Influence of Tacticity on the Conformation and Development of Acid-Base Adducts of PMMA Homopolymers Adsorbed on Aluminium Mirrors. *Int. J. Adhes. Adhes.* **1997**, *17* (3), 257–261. [https://doi.org/10.1016/S0143-7496\(97\)00011-0](https://doi.org/10.1016/S0143-7496(97)00011-0).
- (38) Jeurgens, L. P. H.; Sloof, W. G.; Tichelaar, F. D.; Mittemeijer, E. J. Structure and Morphology of Aluminium-Oxide Films Formed by Thermal Oxidation of Aluminium. *Thin Solid Films* **2002**, *418* (2), 89–101. [https://doi.org/10.1016/S0040-6090\(02\)00787-3](https://doi.org/10.1016/S0040-6090(02)00787-3).
- (39) Khasanah; Reddy, K. R.; Ogawa, S.; Sato, H.; Takahashi, I.; Ozaki, Y. Evolution of Intermediate and Highly Ordered Crystalline States under Spatial Confinement in Poly(3-Hydroxybutyrate) Ultrathin Films. *Macromolecules* **2016**, *49* (11), 4202–4210. <https://doi.org/10.1021/acs.macromol.6b00431>.
- (40) Sun, X.; Gao, N.; Li, Q.; Zhang, J.; Yang, X.; Ren, Z.; Yan, S. Crystal Morphology of Poly(3-Hydroxybutyrate) on Amorphous Poly(Vinylphenol) Substrate. *Langmuir* **2016**, *32* (16), 3983–3994. <https://doi.org/10.1021/acs.langmuir.6b00058>.
- (41) Khasanah; Reddy, K. R.; Ogawa, S.; Sato, H.; Takahashi, I.; Ozaki, Y. Evolution of Intermediate and Highly Ordered Crystalline States under Spatial Confinement in Poly(3-Hydroxybutyrate) Ultrathin Films. *Macromolecules* **2016**, *49* (11), 4202–4210. <https://doi.org/10.1021/acs.macromol.6b00431>.
- (42) van den Brand, J.; Sloof, W. G.; Terryn, H.; de Wit, J. H. W. Correlation between Hydroxyl Fraction and O/Al Atomic Ratio as Determined from XPS Spectra of Aluminium Oxide Layers. *Surf. Interface Anal.* **2004**, *36* (1), 81–88. <https://doi.org/10.1002/sia.1653>.
- (43) Iriondo, P.; Iruin, J. J.; Fernandez-Berridi, M. J. Association Equilibria and Miscibility Prediction in Blends of Poly(Vinylphenol) with Poly(Hydroxybutyrate) and Related Homo- and Copolymers: An FTIR Study. *Macromolecules* **1996**, *29* (17), 5605–5610. <https://doi.org/10.1021/ma960286l>.
- (44) Revol, J.-F.; Chanzy, H. D.; Deslandes, Y.; Marchessault, R. H. High-Resolution Electron Microscopy of Poly( $\beta$ -Hydroxybutyrate). *Polymer* **1989**, *30* (11), 1973–1976. [https://doi.org/10.1016/0032-3861\(89\)90281-4](https://doi.org/10.1016/0032-3861(89)90281-4).
- (45) Fowkes, F. M.; Tischler, D. O.; Wolfe, J. A.; Lannigan, L. A.; Ademu-John, C. M.; Halliwell, M. J. Acid-Base Complexes of Polymers. *J. Polym. Sci. Polym. Chem. Ed.* **1984**, *22* (3), 547–566. <https://doi.org/10.1002/pol.1984.170220304>.
- (46) Iwata, T.; Doi, Y. Morphology and Enzymatic Degradation of Poly( $\epsilon$ -Caprolactone) Single Crystals: Does a Polymer Single Crystal Consist of

- Micro-Crystals? *Polym. Int.* **2002**, *51* (10), 852–858.  
<https://doi.org/10.1002/pi.858>.
- (47) Morphology and Enzymatic Degradation of Poly(l-lactic acid) Single Crystals | Macromolecules <https://pubs.acs.org/doi/abs/10.1021/ma980008h> (accessed Oct 23, 2019).
- (48) Harada, T.; Yoshida, H.; Ohno, K.; Matsuura, H. Conformational Stabilities of 1-Methoxy-2-(Methylthio)Ethane and Relevant Intramolecular CH Á Á Á O Interaction Studied by Matrix-Isolation Infrared Spectroscopy and Density Functional Calculations. *Chem. Phys. Lett.* **2002**, *8*.
- (49) Hobza, P.; Havlas, Z. Blue-Shifting Hydrogen Bonds. *Chem. Rev.* **2000**, *100* (11), 4253–4264. <https://doi.org/10.1021/cr990050q>.
- (50) Aoyagi, Y.; Doi, Y.; Iwata, T. Mechanical Properties and Highly Ordered Structure of Ultra-High-Molecular-Weight Poly[(R)-3-Hydroxybutyrate] Films: Effects of Annealing and Two-Step Drawing. *Polym. Degrad. Stab.* **2003**, *79* (2), 209–216. [https://doi.org/10.1016/S0141-3910\(02\)00273-2](https://doi.org/10.1016/S0141-3910(02)00273-2).

## Appendix A

### PERMISSIONS

#### ACS Publications Division Permissions

##### Overview of Permissions and RightsLink

The American Chemical Society (ACS) offers the RightsLink service to meet most of your licensing needs for material published by the ACS Publications Division. See the specific instructions in the link below

<https://pubs.acs.org/page/copyright/permissions.html>

Before requesting permission for the use of any material, check to be sure the image is not credited to a source other than ACS. The credit may be given in the figure/table/chart caption or in the reference section. ACS cannot grant permission for material for which it does not own copyright.

RightsLink cannot be used for repository requests. Send requests to the journal editorial office.

If you receive an error message when making your RightsLink request, see Solutions for RightsLink Errors.

##### Items for Which ACS Does Not Grant Permission

Note that ACS does not grant permission for these materials or provide the following:

Posting of ACS articles/chapters on Web sites or in online publications.

Granting permission to third parties. Ask your client to request permission and provide them with the requirements on this page.

We cannot provide high-resolution files for images. If permission is granted, please contact the author for the image.

The use of ACS figures/tables/charts to be included in the same or another ACS journal does not require ACS permission.

Individual schemes and structures are free of charge and do not require a license.

PDFs of articles or e-mailing of articles.

### **Elsevier Rights & permissions**

The terms of your purchasing agreement determine if you can reuse Elsevier content. If reuse of the content is not permitted you can obtain permission on ScienceDirect through RightsLink or by contacting Elsevier's Global Rights Department.

When is permission required?

As a general rule, seek permission to reproduce any substantial part of a copyrighted work. This includes text, illustrations, charts, tables, photographs, or other material from previously published sources used without significant adaptation. Determining what is a "substantial part" is subjective, and depends on the significance of the material and the quantity of material used. Please note as well that sources of all data must be credited, whether or not permission is required.

Types of reuse that require permission include:

In a book, textbook, journal, magazine, thesis, dissertation, TV program, documentary, movie, or application

In a different format (CD-ROM or DVD)

In a newspaper or newsletter

In conference, classroom or training materials, including continuing medical education (CME)

Desktop delivery, electronic printing, or posting or other use on a website

In a government report

In a poster, presentation, slide kit, promotional material or pamphlet

Photocopies or reprints

Obtaining permission via RightsLink®

Elsevier recommends requesting reuse permission using the Rightslink® automated service for its ease of use and 24/7 availability. To use RightsLink for ScienceDirect content, see Obtaining Permission to Reuse Elsevier Material (<https://www.elsevier.com/authors/journal-authors/policies-and-ethics>).